ABSTRACT

Neutron stars are astrophysical laboratories to study extremely dense matter. The exact composition of the interior of a neutron star is yet unknown. However, recent observational and theoretical developments have provided crucial constraints on the properties of dense matter in neutron stars. In this thesis, we describe how we can use the astrophysical signals from neutron stars to measure their physical properties. We can use these measurements to determine the structure and composition of neutron star. We focus on two phases of the neutron star's life and the astrophysical signals associated with it. First, we look at gravitational wave signals from core-collapse supernovae—the birthplace of neutron stars. We analyze the gravitational-wave signals obtained from three-dimensional simulations of core-collapse and calculate the detection prospects of these signals by the proposed next-generation detectors, such as Cosmic Explorer. We find that Cosmic Explorer can detect a supernova signal in the Milky Way galaxy. We analyze the first ~ 10 ms of the gravitational-wave signal from core-collapse, where the signal is non-stochastic and primarily depends on the core rotation rate and its equation of state. We use data from numerical simulations of collapsing stars with rapidly rotating cores and develop a mapping between the physical parameters and the waveform morphology. We analyze the stochastic part of the signal, which is primarily generated due to the oscillations of the proto-neutron star. We develop a novel method to generate time-frequency spectrograms and we use them to measure the frequencies and energy associated with the quadrupolar $f-$mode oscillations of the proto-neutron star. Lastly, we determine the reproducibility of Riley *et al.* results, in which the authors analyze the X-ray data from NICER to measure the mass and radius of PSR J0030+0451 using X-ray pulse profile modeling. We find that using the data and software artifacts provided, we can not only reproduce their results but can extend them as well. Measuring the mass and radius of pulsar constrains its equation of state, and consequently its internal composition.

NEUTRON STAR INTERIORS:
FROM PROTO-NEUTRON STARS TO
GALACTIC PULSARS

By

Chaitanya Afle

BS, Indian Institute of Science Education and Research Pune, 2016

MS, Indian Institute of Science Education and Research Pune, 2016

DISSERTATION

SUBMITTED IN PARTIAL FULFILLMENT OF THE REQUIREMENTS

FOR THE DEGREE OF

DOCTOR OF PHILOSOPHY IN PHYSICS

Syracuse University

June 2023

ACKNOWLEDGEMENTS

To my collaborators—Ingo Tews, Collin Capano, Adam Burrows, David Vartanyan, Eric Coughlin, and Suman Kundu—thank you for your invaluable ideas and efforts, which enabled us to get the most out of the projects we worked on together.

I would like to thank my defense committee members—Duncan Brown, Eric Coughlin, Alex Nitz, and Laura-Anne Minkoff-Zern—for taking the time to review and critique this dissertation.

To Ashwini Ramesh, Sharvaree Vadgama, Nimisha Thakur, Sohan Sarangi, and Akshay Khadse—thank you for being dear friends throughout these years. I would like to specially thank Kalyanee Shirlekar, for her incredible support, patience, and love.

Finally, I want to express my gratitude to my parents, to whom this thesis is dedicated. I appreciate your unwavering support and for being such a tremendous source of inspiration.

Contents

List of Tables

List of Figures

Preface

Chapter 2 is based on material from:

Varun Srivastava, Stefan Ballmer, Duncan A. Brown, *Chaitanya Afle*, Adam Burrows, David Radice, and David Vartanyan, "Detection prospects of core-collapse supernovae with supernova-optimized third-generation gravitational-wave detectors," **Phys. Rev. D 100, 043026 (2019)**

https://journals.aps.org/prd/abstract/10.1103/PhysRevD.100.043026.

Chapter 3 is based on material from:

Chaitanya Afle, Duncan A. Brown, "Inferring physical properties of stellar collapse by third-generation gravitational-wave detectors," **Phys. Rev. D 103, 023005 (2021)**

https://journals.aps.org/prd/abstract/10.1103/PhysRevD.103.023005.

Chapter 4 is based on the material from:

Chaitanya Afle, Suman Kumar Kundu, Jenna Cammerino, Eric R Coughlin, Duncan A. Brown, David Vartanyan, Adam Burrows, "Measuring the properties of f-mode oscillations of a protoneutron star by third generation gravitational-wave detectors," **Phys. Rev. D 107, 123005 (2023)**

https://journals.aps.org/prd/abstract/10.1103/PhysRevD.107.123005.

Chapter 5 is based on material from the following work which has been submitted for publication to *IEEE CISE* :

Chaitanya Afle, Patrick R. Miles, Silvina Caino-Lores, Collin D. Capano, Ingo Tews, Karan Vahi, Ewa Deelman, Michela Taufer, Duncan A. Brown, "Reproducing the results for NICER observation of PSR J0030+0451," **arXiv:2304.01035**

https://arxiv.org/abs/2304.01035.

To Aai and Baba

Chapter 1

Introduction

Neutron stars are among the densest objects in the universe, second only to black holes. They offer a unique window into the physics of extreme regimes that are not well understood yet, and conditions that cannot be reproduced in terrestrial laboratories. The densities in the core of neutron stars can reach up to ten times the nuclear saturation density ($\rho = 2.8 \times 10^{14}$g/cm^3) [4, 5, 6, 7, 8, 9]. A way to probe the physics of these extreme conditions is by measuring the properties of neutrons stars using the astrophysical signals that they generate.

The exact internal composition of a neutron star is not yet known. We know that they are mostly made of neutrons, because of the inverse beta decay process during a core-collapse supernova—the birthplace of neutron stars. However, the densities at the core of the star are extremely high, and we do not have a full understanding of the kind of matter that could exist in such conditions. The core can be comprised mostly of neutrons with a fraction of protons, or it could host exotic particles like hyperons, deconfined quarks, etc [10, 11]. The interactions between these particles scale up on a larger scale as the relationship between pressure and densities, i.e. the "cold" equation of state [12]. This relationship describes the behavior of cold, dense matter, that comprises the old, isolated neutron stars, and neutron stars in binary systems before they come close to their companions. When the neutron stars are born, or when they are in a binary system and merge with their companion object, the conditions are hot and dynamic and one has to take into account the temperature, in addition to the pressure and density, to describe the "hot" equation of state of dense matter.

Given a pressure-density relationship, and the Tolman–Oppenheimer–Volkoff relativistic stellar structure equation [13, 14], one can map out the relationship between the mass and the radius of the neutron star. The uncertainties in the composition of the neutron star and the inter-particle forces results in a range of models that describe the pressure-density-temperature relations, and consequently, a range of mass-radius relationships.

Since neutron stars are highly compact objects, we have to take into account relativistic effects when we model them. We can utilize this property of the neutron stars to measure their physical properties. For example, we can use the gravitational-waves from neutron stars (from a newly formed proto-neutron star, or from binary neutron star mergers) to measure its mass and radius. Using observations and theoretical models, we can constrain the plausible regions in the mass-radius plane. Backtracking, we can do the same for equations of state represented in the pressure-density plane, and hence constrain the type of particles residing in the core of a neutron star [15, 16, 17].

In this thesis, we investigate methods to measure the physical properties of neutron stars using astrophysical observations. First, we focus on the proto-neutron star phase of a neutron star during its birth in a core-collapse supernova. In particular, we focus on gravitational-wave radiation from a supernova, during which the primary source of the radiation is the proto-neutron star oscillations. Gravitational-waves and neutrinos are the only possible observational windows to extract the physics from proto-neutron stars, since the stellar material enveloping them is opaque to electromagnetic waves. Using such signals, we demonstrate that not only can we measure the properties of the proto-neutron star, but we can also shed more light on the supernova mechanism. Secondly, we measure the mass and radius of an old, cold neutron star by analyzing the X-ray emission from its surface. In this phase, the neutron star has cooled off due to neutrino emission and has become stable, unlike the proto-neutron star phase where it was hot and dynamic. We can measure various physical properties of the neutron star using both kind of measurements. In particular, measurements of mass and radius of neutron stars can constrain the possible equations of state, and consequently their structure and inner composition.

1.0.1 Gravitational waves

The Advanced LIGO [18] and Virgo [19] observatories are set to begin their fourth observing run in the summer of 2023 to detect gravitational waves from mergers of compact object binaries [20]. These binaries can be comprised of stellar-mass black holes or neutron stars. During the first three observing runs, the observatories reported a total of 52 confident detections [21, 18, 22, 23, 24, 25], including the first direct observation of gravitational waves from a binary black hole merger, GW150914 [26], and a direct detection of gravitational waves from a binary neutron star merger, GW170817 [27]. The latter event was also observed across the electromagnetic spectrum - from gamma-rays to radio [28]. The total catalog of signals includes those from two binary neutron stars, two neutron star-black hole, and a signal from a binary system with the light compact object object either the lowest mass black hole or one of the highest mass neutron star. With all these observations, the era of gravitational-wave astronomy has just begun, and we will be able to answer a plethora of long-standing physics questions using it.

Gravitational waves were one of the earliest predictions of the Theory of General Relativity. If one considers the case where the spectime metric can be approximated as $g^{\mu\nu} = \eta^{\mu\nu} + h^{\mu\nu}$, where $\eta^{\mu\nu}$ is the flat, Minkowski spacetime metric and $h^{\mu\nu}$ is a small perturbation on it, then in the transverse-traceless gauge, Einstein's equations become a wave equation for $h^{\mu\nu}$. If a system has time-varying quadrupole moment $I_{\mu\nu}$, then it will generate gravitational waves. Specifically, the expression is:

$$h_{\mu\nu} = \frac{2G}{Dc^4} \ddot{I}_{\mu\nu}, \tag{1.1}$$

where D is the distance between the source of gravitational radiation and the observer. Since the factor $\frac{2G}{c^4} = 1.6 \times 10^{-44}$ kg^{-1} m^{-1}s^2 is strikingly small, the factor $\frac{\ddot{I}_{\mu\nu}}{D}$ has to be tremendously large to obtain measureable values of h. Astrophysical sources, primarily involving compact objects, provide large values of $\ddot{I}_{\mu\nu}$, such that even though the distances D are also huge, the values of h are measureable. For example, a binary neutron star system of stars of mass $1.4M_\odot$ and of radius 11 km each will produce $\ddot{I}_{\mu\nu} \approx 10^{45}$kg m^{2}s^{-2}. Such a source will generate gravitational waves that would be $\approx 10^{-21}$ at a distance of 1 Mpc. In order to detect such a signal, one has to be able to measure extremely small changes in distances when the gravitational-wave passes by.

Gravitational-wave observatories are kilometer-scale Michelson interferometers with Fabry-Perot cavities in each of their arms. As a gravitational-wave passes through the detector, it stretches and squeezes the spacetime, distorting the armlengths of the interferometer. This results in a phase difference over time in each of the arms. The detectors measure the signal amplitude in the terms of the strain h, which is a dimensionless quantity given by

$$h = \frac{\Delta L}{L}, \tag{1.2}$$

where L is the arm length of of the detectors when there is no gravitational-wave passing through it, and ΔL is the change in arm length induced by the signal.

The sensitivity of the detectors is dependent on various noise sources. These include the seismic noise (which is dominant at low frequencies, $\lesssim 10$ Hz), thermal noise (contributes majorly at frequencies $\approx 10 - 100$ Hz), and quantum noise (dominant at frequencies $\gtrsim 200$ Hz) [29]. Advanced LIGO is most sensitive in the band $15 - 1000$ Hz. From equation 1.2, we can see that larger armlengths would result in larger ΔL for the same signal waveform strain amplitude. Hence, Advanced LIGO is 4 km long. Future detectors, such as the Cosmic Explorer [30] in United States and Einstein Telescope [31] in Europe are planned to have 40km and 10 km armlengths, respectively. They will be almost an order of magnitude more sensitive than the current detectors, making the nearby sources much louder, and further away sources detectable.

1.0.2 Core-collapse supernovae

When the core of a massive star ($8M_\odot \lesssim M \lesssim 130M_\odot$ when it becomes a main sequence star) exceeds its Chandrashekhar mass, it begins to undergo gravitational collapse [32, 33, 34, 35]. The compression of the core leads the material to nuclear densities, and the nuclear equation of state stiffens, which results in the *core bounce*. This creates a shock wave that propagates outwards and plows through the outer envelope of the star, causing an explosion and leaving behind a compact remnant [36]. The core collapse and subsequent bounce can power supernova explosions that radiate light, neutrinos, and gravitational waves (see e.g. Refs. [37, 38, 39, 40] and references therein). Electromagnetic waves generated deep within the star get absorbed by the material around them. We only receive the electromagnetic signals

from the outer edges of the star. The gravitational waves and neutrinos, on the other hand, are generated within the core and travel unhindered through the stellar envelope, carrying information about the structure and dynamics of the inner parts of the star.

The outgoing shock initially stalls, primarily because it loses its energy to dissociate heavy nuclei as it propagates outwards. It also faces the ram pressure of the infalling material. The primary focus of supernova theorists and simulations for the past few decades has been to explain how this shock eventually revives and blows up the star. The currently accepted hypothesis is that a fraction of neutrinos that are produced in the proto-neutron star get trapped in the gain region–the region just behind the shock. Turbulence has been shown to be the key to revive the shock. The trapped neutrinos heat up the gain region to generate enough turbulence to revive the shock [33, 41].

The neutrino-heating mechanism is consistent with the observations and theoretical predictions of explosion statistics, energies and other observables. The majority of the gravitational binding energy in a supernova, over 99% ($\sim 10^{53}$ ergs), is discharged through neutrinos. To restart the stalled shock, the neutrino-heating mechanism needs just a small fraction of this energy to connect with the matter inside the collapsing star via the weak force.

Core-collapse supernovae are crucial to understand because they are one of the primary sources of heavy elements in the universe [42]. They also influence the interstellar medium, can emit cosmic rays, and are the source of the cosmic relic neutrino background [43]. Supernova physics is a complex blend of gravity, hydrodynamical instabilities, neutrino interactions, radiation dynamics in multi-dimensions.

Gravitational waves from Core-Collapse Supernovae

Galactic core collapse supernovae are one of the potential sources of gravitational waves that can be detected by the next-generation gravitational-wave detectors [44, 45, 46]. This kind of detection is particularly interesting because the gravitational-wave signal is accompanied by neutrino signal and possibly by electromagnetic observations. The range of detection of core collapse supernovae for aLIGO type detectors is around 10 kpc for optimally oriented sources, while for the third-generation detectors it goes as far as 70 kpc. The estimated event rate for core-collapse supernovae

in a galaxy the size of the Milky Way is 1-3 per century [47, 48, 49, 50]. If the third-generation detectors detect such an event in the galaxy, the signal-to-noise ratio (SNR) will be high enough to extract very interesting physics (such as the equation of state, rotation rate, central density, etc. of the protoneutron star) out of the observed data. In Chapter 2 we discuss the detection prospects of gravitational-waves from supernovae for the next-generation gravitational-wave detectors.

The gravitational-wave signal of core-collapse supernovae comprises of three phases - the core bounce and the immediate postbounce oscillations of the protoneutron star $(5 - 10$ ms), prompt convection phase $(10 - 50$ ms), and the the neutrino convection/explosion phase $(\gtrsim 100$ ms). Due to the neutrino convection in and above the protoneutron star, and fallback accretion onto it, the latter phase is stochastic in nature. However, the core bounce and postbounce phases are non stochastic and contain vital information about the physical parameters such as the angular momentum of the core and nuclear equation of state. Most of the work in the past three decades was focused on the bounce and the postbounce phases for a rapidly rotating core of a massive star [51, 52, 53]. However, our current understanding of stellar evolution and estimates of rotation rates of pulsars suggest that the cores of massive stars will be slowly rotating by the end of their lives owing to angular momentum transport to the stellar envelope and eventually to stellar winds [54, 55]. They will also be weakly differentially rotating due to angular momentum redistribution because of strong magnetic torques [56, 57]. Rotation rate of the core is an important quantity to measure as it provides crucial insight into the rotation rates of the first generation compact objects formed as an aftermath of the core-collapse. In Chapter 3 we focus on the first ~ 10 ms of the gravitational-wave signal from core-collapse to measure the rotation-rate and the equation of state of the protoneutron star.

During the neutrino convection phase, the primary source of gravitational-waves are the proto-neutron star oscillations. These oscillations are thought to be caused by the infalling, accreting matter on the proto-neutron star. The stochasticity of the signal in the time domain renders it very difficult to be modeled in the same vein as a gravitational-wave signal from compact binary coalescence. However, if we look at the short-time Fourier transform of the signal, we see a distinct track starting at ~ 200 ms after the core bounce at ~ 500 Hz, and grows to ~ 1000 Hz 500 ms after

the core bounce. Linear perturbation analysis of the simulation data for the proto-neutron star reveals that this track is associated with the fundamental $l = 2$ $f-$mode oscillations of the protoneutron star. An $f-$mode, or fundamental mode oscillation is a subclass of gravity modes—modes of oscillations in which buoyancy is the restoring force.

In Chapter 4 we analyze the stochastic phase gravitational-wave signal ($t-t_{\text{bounce}} \gtrsim$ 0.4 seconds) to measure the frequencies and energies associated with the fundamental $f-$mode oscillations of the proto-neutron star. Measurement of these quantities help in inferring the central densities of the proto-neutron star, and may shed more light on the supernova mechanism.

1.0.3 Millisecond pulsars and X-ray pulse profile modeling

Pulsars are rotating neutron stars that have period of rotation that ranges from a few milliseconds to a few seconds. They emit radiation that an observer can see at regular intervals as the pulsar is rotating [58, 59]. In particular, the neutron star's surface has "hotspots" - regions of higher temperature than the ambient temperature that emit X-rays. These surface emissions provide us a way to to probe the interior composition of the neutron star. The X-rays emitted from the surface travel through the exterior spacetime of the neutron star. Since the pulsar is rotating, they also get rotationally deformed—redshifted when the hotspot is going away from the observer as the pulsar rotates, whereas blueshifted when the hotspot is appearing again. Given a mechanism of how this radiation is produced on the surface and the ray propagation of the radiation through the spacetime, one can model the pulsed signal that can be detected by a distant observer [60]. One can parameterize this model incorporating the mass, radius, rotation rate, etc. Using a likelihood function, one can then perform a Bayesian analysis to determine the model parameters that describe the posterior.

In 2018, NASA's Neutron star Interior Composition Explorer (NICER) observed X-rays from a galactic pulsar PSR J0030+0451, which is at a distance of ~ 0.33 kpc and has a period of rotation of 4.89ms. Riley *et al.* reported Bayesian parameter measurements of the mass and the radius, among other parameters, and found that mass of the pulsar is $1.34^{+0.15}_{-0.16} M_\odot$ and the radius is $12.71^{+1.14}_{-1.19}$km, where the errors depict the 68% credible interval. In Chapter 5, we explore the reproducibility of Riley *et. al.* [61] analysis, given the data, software, and documentation provided to the

public. We also extend and modify their original analysis to test its robustness to the priors used in the analysis.

We discuss the conclusions drawn from these studies in Chapter 6.

Chapter 2

Detection prospects of gravitational-waves from Core-collapse supernovae

2.1 Introduction

The Advanced LIGO [62] and VIRGO [63] gravitational-wave detectors observed signals from the coalescence of over ten binary black holes (BBH) and one binary neutron star merger (BNS) [64, 65, 66, 67, 68, 69] by the end of their second science run. Core-collapse supernovae (CCSNe) are a potential astrophysical source of gravitational waves that could be detected by interferometric detectors. The gravitational waves are generated deep in the star, at the collapsing core, and are emitted untouched by the outer envelopes. They contain vital information about the interior of the star and about the core-collapse process, which is not present in the electromagnetic counterpart of the emitted radiation. We can infer various physical parameters such as the nuclear equation of state, rotation rate, pulsation frequencies, etc. from the gravitational wave signal of a CCSNe once it has been detected [70, 71, 72]. However, gravitational waves from CCSNe are yet to be observed [73, 74]. The inferred sensitivity of the aLIGO-VIRGO network to detect CCSNe ranges from a few kiloparsecs (kpc) to a few megaparsecs (Mpc) [75]. The range of a few megaparsecs in [75] corresponds to extreme emission models which assume properties of stars which are unlikely to occur in astrophysical scenarios. The smaller sensitive range of a few

kiloparsecs to CCSNe along with low CCSNe rates within galaxies leads to a low gravitational-wave detection probability from CCSNe [76, 77, 78, 79, 80].

The gravitational radiation from CCSNe depends on a complex interplay of general relativity, magneto-hydrodynamics, nuclear, and particle physics. The burst signal, therefore, does not have a simple model, and we have to use numerical simulations to understand its structure. Numerical simulations also help in understanding the frequency content of the gravitational wave signal which is crucial in determining the parameters to tune future detectors towards supernovae.

The three-dimensional (3D) simulations of core-collapse supernovae reveal that their gravitational-wave signatures are broadband with frequencies ranging from a few hertz to a few thousand hertz. The time-changing quadrupole moment of the emitted neutrinos occupies the few Hertz to ten Hertz range, while the higher frequencies are associated with the prompt convection and rotational bounce phase, the proto-neutron-star (PNS) ringing phase, and turbulent motions. [81] and [82] demonstrated that the excitation of the fundamental g- and f-modes of the PNS can be a dominant component and that much of the gravitational wave energy emitted is associated with such PNS oscillations [83, 84]. The frequency ramp with time after the bounce of the latter is a characteristic signature of CCSNe and will reveal the inner dynamics of the residual PNS core and supernova phenomenon once detected. There now exist in the literature numerous 3D CCSNe models that map out the gravitational-wave signatures expected from CCSNe [85, 86, 87, 88, 80, 89]. For this study, we focus on the extensive suite of 3D waveforms found in [80].

In our work, we optimize the design prospects of a third-generation Cosmic-Explorer-like detector to detect gravitational wave signals from CCSNe and discuss the astrophysical consequences. We focus on the prospects for detection of non-rotating or slowly rotating stars since they are likely to be astrophysically more likely [90]. We first review the detection ranges for the second-generation detectors. A significant amount of power is emitted by CCSNe within the gravitational-wave frequency range 500 Hz to 1500 Hz. Therefore, in order to improve the sensitivity of gravitational wave detectors to CCSNe, we need to tune the detector parameters to increase the sensitivity in this bandwidth. With the present models of likely gravitational wave emission from CCSNe [80], we find that the detectable range with a supernovae-optimized Cosmic-Explorer-like third generation detector is still only up

to a hundred kiloparsecs. The detector range is therefore limited to CCSNe that occur within our galaxy. The corresponding event rate is approximately two per century [91, 92, 93, 94, 95]. However, the supernovae-optimized detector would improve the signal-to-noise ratio (SNR) for the galactic sources by approximately 25% as compared to the Cosmic-Explorer. For completeness, we also discuss the strain requirements in a detector to achieve CCSNe event rates of the order of one per year. To this end, we address the fundamental sources of noise that limit our sensitivity to achieve this desired strain.

Distance	Type-II CCSNe rate (per century)	References
Milky way (D < 30 kpc)	0.6-2.5	[91, 92, 93, 94, 95]
M31 or Andromeda (D = 770 kpc)	0.2-0.83	[96, 97, 98, 93, 95]
M33 (D = 840 kpc)	0.62	[93, 95]
Local Group (D < 3 Mpc)	9	[99, 95]
Edge of Virgo Super-cluster (D < 10 Mpc)	47	[100, 101, 102]
Virgo-cluster (D < 20 Mpc)	210	[101, 103]

Table 1: The cumulative rate of CCSNe in out local universe. To achieve a detection rate of one per year, assuming a 100% duty cycle of the gravitational wave detector, we need a strain sensitivity to have a CCSNe reach of the order of 10 Mpc.

2.2   Gravitational waves from CCSNe

Fig. 1 shows the spectrograms of the waveforms obtained from the simulation for the $19 M_\odot$ progenitor. The left column shows the spectrogram of the waveform from the 3D simulation, while the right column shows the spectrogram of the waveform from the 2D simulation. The red vertical dashed line in the right column represents the simulation time of the 3D waveform. For simulations of the same ZAMS mass, both the 2D waveforms and the 3D waveforms show similar behavior in the time-frequency plane. We can see the prompt convection signal for the first ~ 10 milliseconds after the core bounce, followed by the characteristic g/f-mode ring up of the proto-neutron star (PNS) increasing in frequency [104]. For the 2D waveforms, the frequency ranges from ~ 20 Hz to ~ 2000 Hz. The g/f-mode signal of the PNS starts around 200 milliseconds after the core bounce at a frequency of ~ 500 Hz, and 1 sec after the core bounce reaches ~ 1500 Hz. For the waveforms obtained from the 3D simulations, the frequency ranges up to ~ 1000 Hz. This is because the 3D simulations end earlier $(0.4 - 1.0$ sec after core bounce).
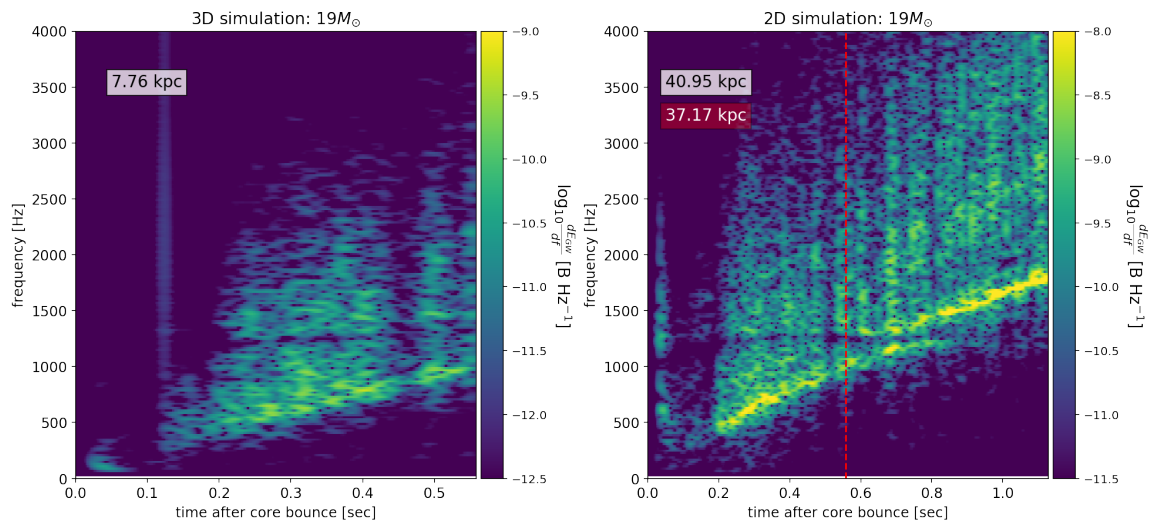
Figure 1: Spectrograms of gravitational-wave waveforms from 3D (left column) and 2D (right column) simulations of $19M_\odot$ progenitor. The number on the top left corner each plot with white background is the distance for which these GW signals have an optimal SNR of 8. For the 2D simulations, we recalculate this distance (shown on red background) by truncating the waveform at the end-time of the corresponding 3D simulation. The red vertical dashed line shows the truncation time.

ZAMS Mass	Optimal distance (kpc)			Normalized σ^2 (10Hz-450Hz)		Normalized σ^2 (450Hz-2000Hz)	
	3D	2D	2D trun-cated	3D	2D	3D	2D
$9M_\odot$	2.43	15.51	15.46	0.342	0.232	0.658	0.767
$11M_\odot$	5.87	31.96	26.68	0.154	0.058	0.845	0.941
$11M_\odot$ (w/o MB)	5.99	28.78	26.04	0.131	0.099	0.869	0.9
$19M_\odot$ (w/o MB)	7.75	40.61	37.18	0.120	0.074	0.880	0.925
$25M_\odot$	13.35	48.26	40.09	0.12	0.069	0.88	0.931
$60M_\odot$	9.63	48.79	36.30	0.211	0.065	0.790	0.935

Table 2: For different ZAMS mass, with and without many-body (MB) approximation the table summarizes the optimal distances for aLIGO and σ^2 for a flat PSD in the frequency bandwidths 10Hz - 450Hz and 450Hz - 2000Hz for waveforms.

We calculate the optimal distance (or the detection distance for optimally-oriented sources) for each of these waveforms, as defined below [105]:

$$d_{opt} = \frac{\sigma}{\rho^*} = \frac{1}{\rho^*} \left[2 \int_{f_{\text{low}}}^{f_{\text{high}}} df \frac{\tilde{h}(f)\tilde{h}^*(f)}{S_h(f)} \right]^{\frac{1}{2}} \qquad (2.1)$$

where $S_h(f)$ is the power spectral density (PSD) of the detector, $\rho^* = 8$ is the signal-to-noise ratio for an optimal matched filter (optimal SNR) and the limits over the integral are defined by f_{low} and f_{high}. We note that for unmodeled searched like CCSNe, matched filter searches is not applicable. Instead, Coherent WaveBurst searches (CWB) or incoherent transient searches (Omicron) are implemented to search for CCSNe in aLIGO-VIRGO strain data [106, 107, 108, 109]. There is mismatch which leads to loss of SNR when one moves from modeled match-filter searches to unmodeled transient wavelet burst searches [110]. The use of optimal SNR in the paper presents an optimistic scenario without any of these losses. We set the lower frequency cutoff, $f_{\text{low}} = 10$ Hz and use `aLIGOZeroDetHighPower` [111] as PSD for aLIGO to compute the optimal distances for all the waveforms, which are shown in Table 2. For aLIGO, the average distances for waveforms from 3D simulations are ~ 8 kpc, while the average distances for corresponding 2D numerical simulations are ~ 35.5 kpc. The 3D simulations have shorter times with respect to the 2D simulations, so we truncate the 2D simulations at the same corresponding times to compare the optimal distances. In doing so, the average optimal distance for the waveforms from the 2D simulations is ~ 30 kpc. We find that the 2D waveforms are, on an average, ~ 4 times louder than the 3D waveforms. Therefore, we will only use the waveforms from 3D simulations to tune the third generation detectors for CCSNe and calculate ranges.

Table 2 also shows the optimal signal-to-noise (SNR) σ^2 of the waveforms in two frequency bandwidths : 10Hz - 450Hz and 450Hz - 2000Hz. These σ^2 values have been calculated using a flat PSD (see section §2.5), so that we can infer the distribution of the frequency content of the waveforms without being biased by the noise curves of any detector. We can verify from the spectrograms that almost all of the frequency content is below 2000 Hz. We find that the ratio of σ^2 in the range 10Hz - 450Hz to that in range 450Hz - 2000Hz is ~ 0.2 for 3D simulations while for 2D simulations it is ~ 0.1. This implies that $\sim 80\%$ of the content of the waveforms is in the frequency

range 450Hz - 2000Hz. This is crucial since in Secs §2.3 and §2.4, we tune the detector parameters to increase the sensitivity in this frequency range.

In section §2.3, we define a phenomenological CCSNe waveform which is derived from the 3D numerical waveforms. We maximize the range of the phenomenological supernovae waveform (see Fig. 2) with a third-generation Cosmic-Explorer-like detector. We use GWINC to estimate the noise floor for different detector parameters [112]. The maximized range achieved can then be translated into the corresponding event rate of CCSNe, as summarized in table 1 (assuming a 100% detector duty-cycle).

We use the waveforms from [80] to compare the ranges of different waveforms of CCSNe using the Einstein Telescope (ET), the Cosmic Explorer (CE) and the Supernovae-Optimized detector (SN-Opt). In section 2.5, we invert the problem to calculate the strain requirements of a *hypothetical* detector to achieve an event rate of the order of one in two years or in the terms of distances – has a range of the order of 10 Mpc for gravitational-wave signals from CCSNe. Lastly, we consider in section §2.5 detector configurations beyond the third-generation detectors (Hypothetical) and find the ranges for different numerical waveforms of CCSNe.

2.3   Defining a Representative Supernovae Gravitational-Wave Waveform

To maximize the detectable range for CCSNe in a given detector configuration, we need a reference CCSNe waveform that captures the broad features of supernovae waveform. The reference waveform must have the strain amplitude and spectral features similar to any supernovae waveform. We use the waveforms from the 3D simulations of core-collapse [113, 80] to generate a phenomenological model that captures the broad range of features of core-collapse supernovae waveform. We generate the phenomenological waveform to average out the power emission features from different numerical waveforms so that features in any one of the waveforms do not affect the results of the study. Thereby, the phenomenological waveform provides a model-independent approach.

We construct the phenomenological waveform by a sum of sine-Gaussian bursts. A sine-Gaussian can be defined with three parameters, the central frequency f_o, the quality factor or the sharpness of the peak Q and the amplitude scale h_o. The frequency

domain representation of a sine-Gaussian can be expressed with these parameters as

$$\tilde{s}(f) = \frac{h_o}{4\sqrt{\pi}} \frac{Q}{f_o} e^{-\frac{(f-f_o)^2 Q^2}{4f^2}} \tag{2.2}$$

The different frequencies are used to model different spectral features of the core-collapse waveform. We choose central frequencies f_o^i for sine-Gaussian using the numerical waveforms from 3D simulations of core-collapse. We choose, by hand, five distinct central frequencies f_o^i which correspond to peak emission in the numerical waveforms. We limit ourselves to five distinct values of frequencies in order to avoid over-fitting the sine-Gaussian phenomenological waveform to the numerical waveforms. We note that the supernovae waveforms have emission at higher frequencies but they are much lower in amplitude. Therefore, for the purposes of optimization, we limit ourselves to an upper limit of 2kHz in the phenomenological waveform.

To build the phenomenological waveform, we divide the frequency domain into four bins ranging from – 10 Hz to 250 Hz, 250 Hz to 500 Hz, 500 Hz to 1 kHz and 1 kHz to 2 kHz. For each of the chosen central frequencies f_o^i, the quality factor Q^i and the amplitude h_o^i are chosen so as to minimize the error in the normalized power in the four different bins of frequencies above. The error in the normalized power in each bin is then added in quadrature for different waveforms and is given by

$$\Delta e = \sqrt{\frac{1}{N-1} \sum_i^N (\text{Model}_{f_{low}}^{f_{high}} - \text{NR}_{f_{low}}^{f_{high}})^2} \tag{2.3}$$

This approach gives us a simple but robust gravitational waveform, free from the parameter degeneracies but capturing the features of gravitational wave radiation from CCSNe. We will use this to perform optimization and maximize the range for this waveform and thus for CCSNe. The errors in the different frequency bins ranging from 10Hz to 250Hz, 250Hz to 500Hz, 500Hz to 1kHz and 1kHz to 2kHz is 3%, 9%, 2% and 19% respectively. The higher error in the last frequency bin is by the construction of the phenomenological waveform and is added to incorporate the features persistent in the 2D waveforms which show higher emissions in this frequency range discussed in section §2.2. Fig. 2 shows the phenomenological waveform constructed. We incorporate this waveform as a reference supernovae signal within GWINC [112]. The ranges, horizon, and reach for the phenomenological waveform can then be calculated by solving for distance D which would rescale the waveform in equation 2.2 as 1/D.
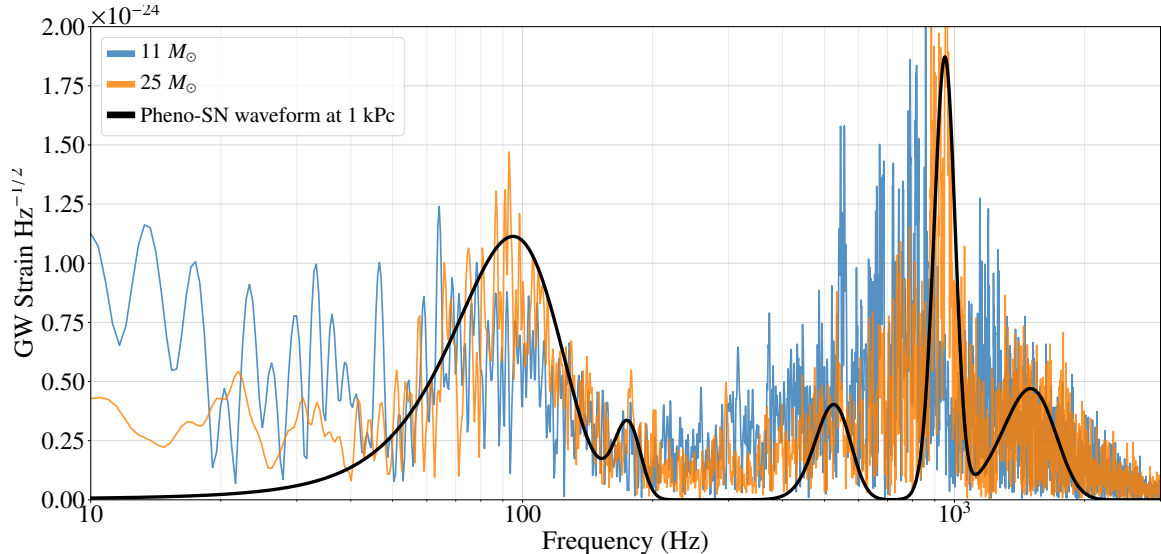
Figure 2: The figure shows the phenomenological waveform used as a representative for gravitational wave emission from CCSNe. The waveform is constructed by using five sine-Gaussian bursts with different central frequencies $f_o = 95$, 175, 525, 950 and 1500 Hz. The quality factor and the amplitude at each central frequency are then derived by minimizing the normalized power emitted in four different bins of frequency from 10 Hz to 250 Hz, 250 Hz to 500 Hz, 500 Hz to 1000 Hz and 1000 Hz to 2000 Hz. The overall amplitude of the phenomenological waveform is not calculated by the fit and can be rescaled. We are interested in the broad features in frequency in different waveforms which is effectively captured in the phenomenological waveform.

In each of the subsequent sections, we go back to each of the numerical waveforms and recompute the ranges achieved with all the different detector designs considered in our study.

2.4 Optimizing SN detectability for 3G detectors

We use the phenomenological gravitational-wave waveform for CCSNe to explore detector configurations that optimize the Cosmic Explorer detector's sensitivity to CCSNe. To avoid overemphasis on any particular frequency chosen in the phenomenological waveform, we down weight narrow-band configurations during the process of optimization. We also avoid narrow-band designs so that the optimized detector's

sensitivity to BNS is greater then 1 Gpc. We will explore the narrow-band configurations with a different approach discussed in section §2.4.3

2.4.1 Broadband configuration tuned for Supernovae

Quantum noise is the predominant source of noise which limits the performance of the gravitational-wave detector. Radiation pressure noise limits the detector sensitivity at low frequencies and shot noise limits sensitivity at high frequencies [62, 63, 114]. In our study, we use the design parameters of Cosmic Explorer [115] as the starting point. For the purposes of optimization, we choose the Cosmic Explorer rather than the Einstein Telescope as the former has a better noise performance at frequencies which are relevant to CCSNe. We optimize over the length of the signal recycling cavity (L_{src}) and the transmissivity of the signal recycling mirror (T_{srm}) to maximize the CCSNe detection range. The quantum resonant sidebands can be tuned with these parameters and we exploit this behavior for supernovae tuning similar to the approach used by Buonanno et al. [116] and Martynov et al. [117].

We also study, the effect of the length of the arm cavity (L_{arm}) on supernovae sensitivity. We use Markov Chain Monte Carlo sampling [118] and particle swarm optimization [119] to search the parameter space and maximize the range for the phenomenological waveform for a broadband detector. During the process of maximizing the range, we down-weight the narrow-band configurations with two constraints for sample points. First, the reflectivity of the signal recycling cavity $T_{srm} > 0.01$. Second, the given detector configuration must have a optimal distance for binary neutron stars systems ($m_1 = m_2 = 1.4\ M_\odot$ and $s_{1z} = s_{2z} = 0$) to be greater than 1 Gpc. By doing so, we ensure that the detector's sensitivity is not lost for compact binaries.

The strain sensitivity improves as the square root of the arm length of the detector as long as the gravitational-wave frequency (Ω) is much less than the free spectral range (f_{FSR}) of the Fabry-Perot cavity. The strain sensitivity of the detector does not always improve by scaling the detector as other fundamental sources of noise also change by scaling the length of the detector [120]. As the gravitational wave spectrum of supernovae has some power in a few kilohertz range, we allow the arm length to vary independently similar to the analysis by [121, 117]. Our simulations indicated the optimal length to be close to 40 km, the upper bound value allowed for the length parameter. As a result, we set the length of the arm cavity to 40 km. For a 40 km

arm length, the f_{FSR} is 3750 Hz. The sensitivity of the detector is limited by the f_{FSR}, any further increase in the length of the arms will reduce the f_{FSR}, resulting in the loss in sensitivity to CCSNe, where the gravitational wave spectrum persists up to a few kilohertz.

The optimal supernovae zero-detuned detector's noise budget is shown in Fig. 3. We find a longer signal recycling with a length of 180 m compared to 55m for Cosmic Explorer along with a transmissivity of the signal recycling cavity changed to 0.015 improved the detector's sensitivity by improving the quantum noise floor at higher frequencies. The loss in sensitivity around 3 kHz is due to the FSR of the arm cavity. The dip at 4 kHz corresponds to the pole of the signal recycling cavity.

We also consider the effects of detuning the signal recycling cavity. We find detuning the signal recycling cavity with active compensation with the squeezing phase can be used to actively tune the third generation detectors in narrow bins of frequency without losing 15 dB of squeezing. It has been proposed that detuning the ground-based detectors can be useful in testing the general theory of relativity [3] with a joint operation with LISA [122]. We will consider the applicability of these configurations to see if they provide any improvements for CCSNe in section §2.4.2.

The optimization over the length of the signal recycling cavity and the transitivity of the signal recycling mirror to maximize the supernovae range with the phenomenological waveform in Fig. 2 leads to an improvement of approximately 30% in the range of CCSNe as compared to the Cosmic Explorer design. However, extending the range from a 70 kpc to 95 kpc does not add any galaxies in our local universe. The optimized supernovae detector does not increase the detection rate as compared to the Cosmic Explorer. For the sources at a fixed distance, this corresponds to approximately 25% improvement in SNR.

The Fig. 4 compares the broadband configuration of a zero detuned 40 km detector optimized for CCSNe signals with the design of the Cosmic Explorer, both configurations have a 15dB squeezing. We improve on the sensitivity in the frequency range from 450 Hz to 1550 Hz at the cost of a loss in sensitivity from 10 Hz to 450 Hz. This results in a 15% loss in range for BNS. However, it still provides higher sensitivity for the post-merger signals based on the predicted frequencies of interest for post-merger oscillations [66, 16, 123, 124]. The table 3 summarizes the parameters and their corresponding ranges towards different gravitational-wave sources. One

advantage offered by the supernovae optimized configuration is robustness. With-out any squeezing, the supernovae optimized detector has a range extending to the LMC, whereas the range of the phenomenological SN waveform with Cosmic Explorer without squeezing is 32 kpc.

Next, we use the noise curves of aLIGO, Cosmic Explorer, Einstein Telescope and Supernovae optimized detector configurations to compute the ranges for the 3D waveforms As stated earlier, the 3D waveforms are representative of astrophysically abundant stars which are not rapidly rotating and the corresponding gravitational wave strain emitted is small. Figure 5 summarizes the ranges of different waveforms based on their ZAMS mass. We see that the sensitivity of the third-generation of gravitational-wave detectors to CCSNe is limited to sources within our galaxy. From the event rates of CCSNe summarized in table 1, we find the corresponding event rate of observation of gravitational waves from CCSNe (assuming a 100 % detector duty-cycle) is approximately one in fifty years.

2.4.2 Detuning a large signal recycling cavity for narrow-band configurations

A significant GW signal from CCSNe lies in the frequency band from 500 Hz to 1500 Hz. The power emitted at different frequencies may vary depending on the astrophysical features of the star - mass, rotation speed, equation of state, etc [125, 126, 113, 80, 127, 128, 85].

In this section, we do not change the detector parameters' such as the transitivity or the length of the signal recycling cavity. This is because these parameters cannot be changed once the detector design is laid out. However, one can detune the signal recycling cavity to maximize sensitivity in a narrow band of frequencies [129, 130]. This response from detuning the signal recycling cavity arises from the two sidebands resonances in quantum noise [116, 114]. We consider the detuning of the signal recycling cavity at different frequencies.

We maintain the frequency dependent squeezing of 15 dB. We achieve 15 dB squeezing in a detuned signal recycling cavity without losing the injected squeezing by actively changing the squeezing angle in accordance with the amount of detuning. Thus, detuning the signal recycling cavity along with actively changing the squeezing angle can be used to switch from a broadband zero-detuned detector to a narrow band

detector with greater sensitivity for some frequencies determined by the magnitude of detuning. We perform another tier of optimization in which we actively vary the amount of detuning and the squeezing angle. We limit the amount of detuning in the range from $-\pi/5$ to $\pi/5$ and the squeezing phase is tuned in between $-\pi$ to π. To optimize the detector response at frequencies of 40 Hz, 100 Hz, 400 Hz and 1200 Hz, we inject a sine-Gaussian at each frequency and then maximize the range for this injected signal by varying only the detuning and squeezing angle for the supernovae optimized detector.

We find that detuning the signal can improve the sensitivity of the detector in narrow bins of frequency below 400 Hz. We do not achieve improvements in sensitivity at higher frequencies therefore, we do not improve the range for different models by detuning the detector. There are no improvements in the optimal SNR values for a source at a fixed distance. In summary, detuning the signal recycling cavity is not useful for improving the Cosmic-Explorer-like detector's sensitivity to CCSNe. Instead, detuning the signal recycling cavity at higher frequency degrades the sensitivity of the broadband supernovae-optimized detector. The corresponding results of detuning the signal recycling cavity are summarized in Fig. 6.

2.4.3 Narrow-band Configurations tuned for Supernovae

The parameters of the broadband supernovae-optimized detector were computed in section §2.4.1 with two constraints. We will in this section relax those constraints and consider narrow-band detector configurations to maximize the range for CCSNe. The phenomenological waveform we developed cannot be used for narrow-band optimization as the fit was performed to match the power of the 3D waveforms over a broad frequency bandwidth. Therefore, we find narrow-band configurations using a different technique.

The length of the signal recycling cavity can be changed to tune the resonant frequency of arising from the coupling of the signal recycling cavity with the arms of the interferometer [131, 116]. The bandwidth of the resonance at a frequency ω_r is given by

$$B = \frac{cT_{srm}}{4L_{src}} \tag{2.4}$$

where T_{srm} is the transmissivity of the signal recycling mirror and L_{src} is the length

of the signal recycling cavity. We choose the length of the signal recycling cavity at 150m, 300m and 750m are such that the resonant frequency ω_r is at 1000 Hz, 750 Hz and 500 Hz respectively. The equation 2.4 is then inverted for bandwidth ranging from 250 Hz to 1600 Hz and the corresponding values of the transmissivity of the signal recycling mirror are calculated.

We find that a narrow-bandwidth of 250 Hz significantly affects the sensitivity of the detector towards CCSNe. This is expected as we have stated earlier that the frequency spectrum of gravitational wave emission from CCSNe is broadband. The range of improvements achieved by narrow-band detectors at 500 Hz, 750 Hz and 1000 Hz with a bandwidth of 250 Hz are also varying from waveform to waveform and therefore is not model independent 7. When the bandwidth is increased to 1600 Hz the range improves for the 750 Hz narrow-band detector for some of the waveforms as shown in Fig. 7. The L_{src} = 300m and T_{srm} = 0.0064 give this narrow-band detector configuration. The mean improvement in optimal SNR with the 750 Hz narrow-band and 1600 Hz bandwidth detector is approximately 10 % with respect to the supernovae optimized broadband detector. However, we caution that the improvement from narrow banding is not the same across all the 3D numerical waveforms. Moreover, this comes at the cost of significant loss of sensitivity below 400 Hz and above 1100 Hz. The range for BNS drops to 3 Gpc (z=0.9) compared to 3.7 Gpc (z=1.1) for supernovae-optimized Cosmic Explorer and 4.3 Gpc (z=1.4) with respect to the Cosmic Explorer.

2.5 Challenges in building a CCSNe Detector to achieve Higher Event rates

In section §2.4.1, we find an optimized third-generation broadband gravitational wave detector for a CCSNe signal has the range only to a few hundred kilo-parsec for the 3D numerical waveforms of CCSNe.

We now address the question of what are the strain requirements for a gravitational-wave detector to be able to detect CCSNe with an event rate of 0.5 per year. From the table 1, we see that this "Hypothetical CCSNe detector" must have a range of $\mathcal{O}(10$ Mpc) for CCSNe to achieve an event rate of 0.5 per year. Moreover, for a single detector, we need a signal to noise ratio (SNR) of 8 to define the detection of a signal against the background. Using the two constraints above we can calculate the

minimum strain sensitivity required to achieve an event rate of 0.5 per year for the waveforms from 3D numerical simulations. The optimal distance for the numerical waveforms can be calculated by equation 2.1. The limits over the integral are defined by f_{low} and f_{high}. To find the strain requirements for the different waveforms we assume a flat PSD over a broadband range of frequency ranging from f_{low} and f_{high}. We consider two scenarios which are summarized in the figures 8. First, we vary the upper limit of the frequency integrated – f_{High} with the lower limit of integration is held constant at 10 Hz. The second scenario where the upper limit of integration is constant at 2 kHz and we vary the lower frequency limit f_{low}. We find the minimum strain sensitivity required for the gravitational-wave detector to detect the CCSNe with an event rate of 0.5 per year is 3×10^{-27} Hz$^{-1/2}$ over a frequency range of 100 Hz to 1500 Hz.

Thus, we need a detector with sensitivity approximately a hundred times better than the Cosmic Explorer design to detect CCSNe with an event rate of 0.5 per year. In the next section §2.5, we will summarize the noise limitations of the third generation detectors and consider design parameters for gravitational-wave detectors beyond the scope of the third-generation to determine the technological hurdles to overcome in order to ever observe gravitational signals from CCSNe more frequently.

It is evident from Fig. 3 that the sensitivity is limited by the quantum noise in the broad range of frequencies. The standard quantum noise limit is dependent primarily on the length of the arm cavities, the test masses and the power of the input laser [132]. The length of the arm cavities cannot be increased any further as the f$_{FSR}$ would significantly affect the performance of the detector at the frequencies of interest. As a result, we set the length of the Hypothetical detectors to 40 kms. Increasing the power of the input laser is the one possibility to reduce quantum noise. We assume an input laser power of 500W. At high frequencies, the quantum noise in the detector manifests itself as shot noise and is limited by photon number arriving at the photo-detector. To see the best we can achieve, we set the photo-detection efficiency of the photo-detector in Hypothetical to 1 (from 0.96 for CE design). For the same reason, we also set the optical and squeezing injection losses in the detector to zero.

The coating thermal noise and the residual gas noise are the next limiting factor in the system. We reduce the substrate absorption by an order of magnitude from

CE design. Lastly, as the frequency range of interest is from 100Hz we can sacrifice the sensitivity at lower frequencies. Thus, we can reduce the masses of the mirrors as we are interested in improving the shot noise characteristics of the detector, at the cost of higher radiation pressure noise. In this setup we optimize over the length of the signal recycling cavity L_{src}, the transmissivity of the signal recycling mirror T_{srm}, the transmissivity of the input test mass T_{itm} and the scale mass parameter to change the masses of the mirror. The optimization over these parameters is aimed at maximizing the range for the representative supernovae waveform, we will reference this optimized detector as *Hypothetical-1*.

The quantum noise limit in a dual-recycled Fabry-Perot interferometer also depends on the gain of the power recycling cavity [116, 114]. We will in another independent optimization also tune the transmissivity of the power recycling mirror T_{prm} along with the above parameters. We define this supernovae-optimized detector as *Hypothetical-2*. The table 3 summarizes the optimal parameters of different detectors. Fig. 9 shows the noise budget of the Supernovae optimized Hypothetical detectors. We see that the residual is the limiting source of the noise. Removing the residual gas noise improves the noise floor of the detector by a factor of two in the wide range of frequencies of interest, see Fig. 9. After removing the residual gas noise, we are limited in sensitivity by quantum noise over the broad range of frequencies.

The strain sensitivity achieved after removing the residual gas noise is $5 \times 10^{-26} \text{Hz}^{-1/2}$. The improvements in photo-detection efficiency, the input laser power, substrate coatings and minimization of optical losses are not sufficient to achieve a strain sensitivity of the order of 3×10^{-27} $\text{Hz}^{-1/2}$ required to detect CCSNe with an event rate of one in two years (see section §2.5).

Lastly, we revisit the numerical waveforms of core-collapse supernovae to see the ranges achieved by the Hypothetical supernovae-optimized detector designs. We find for the 3D waveforms from numerical simulations have a mean distance of 800 kpc, see Fig. 10. Thus, with beyond the third generation detector designs, we would be able to observe core-collapse supernovae from Andromeda. The corresponding event rate is of the order of one in twenty years. The event rate calculation assumes a 100% duty cycle of the detector. The observation rate of gravitational waves from CCSNe is low even for gravitational-wave detectors beyond the scope of the third-generation detectors.
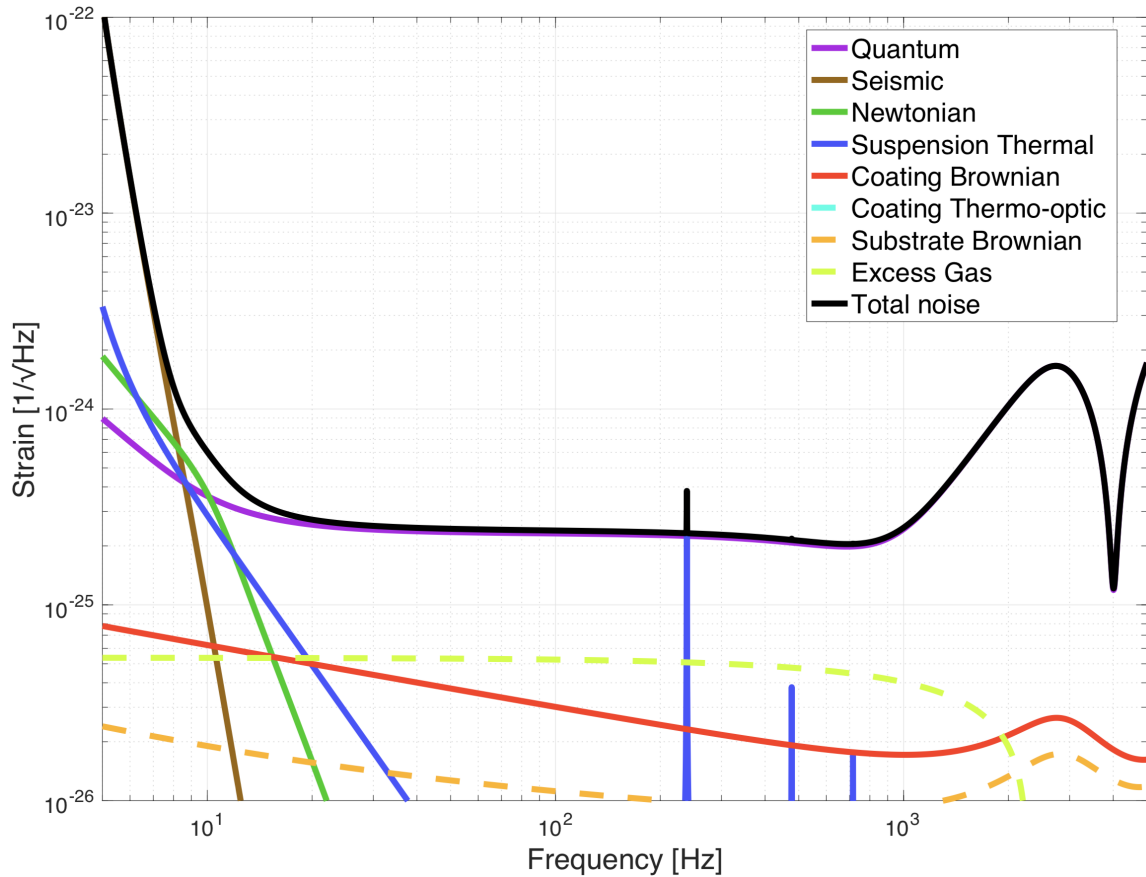
Figure 3: The figure summarizes the noise budget of the supernovae-optimized detector for a gravitational-wave signal with a 45 degrees tilt with respect to the arm cavities [1]. Over the broad range of frequencies of interest, 500 Hz to 1500 Hz, the sensitivity is limited by quantum noise. The dip in sensitivity at 4 kHz corresponds to the pole of the signal recycling cavity.
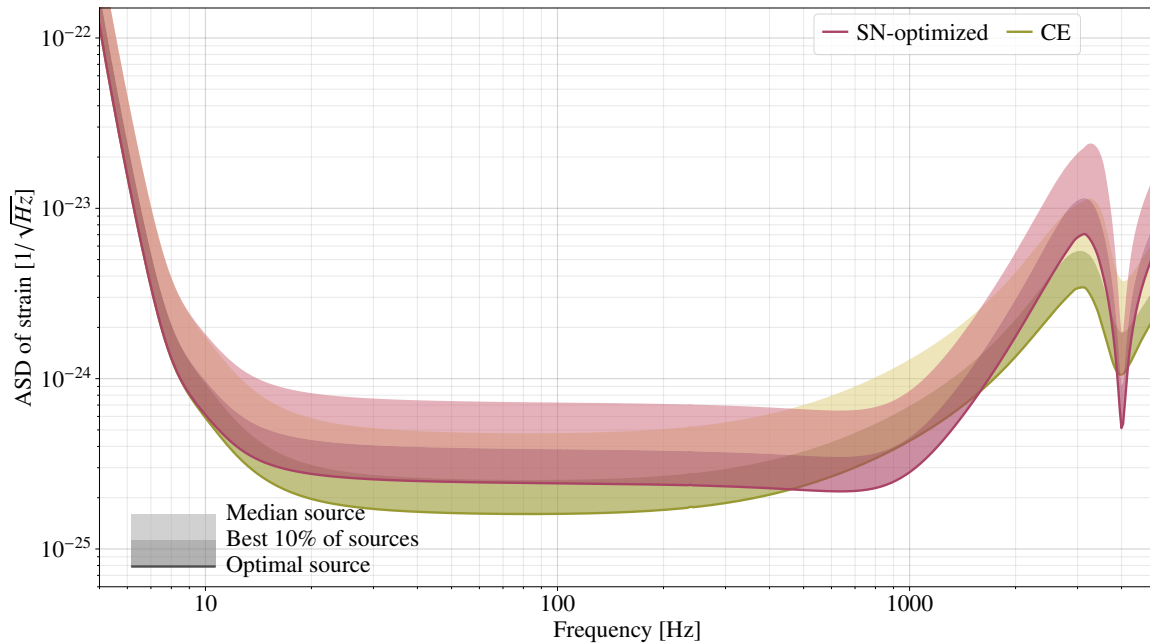
Figure 4: The figure summarizes the sky-averaged and orientation-averaged power spectral density of Cosmic Explorer and supernovae-tuned detector [2]. We see that the Cosmic Explorer has a better noise floor from 10 Hz to 450 Hz. The supernovae-tuned detector has improved sensitivity over the range from 450 Hz to 1600 Hz. The numerical waveforms of CCSNe suggest that a significant amount of power is emitted in this range. The optimization for CCSNe improves the range from 70 kpc to 95 kpc for CCSNe. However, this range improvement does not add any new galaxies. Therefore, the event rate does not change with the improved sensitivity and we are limited to sources within our galaxy.
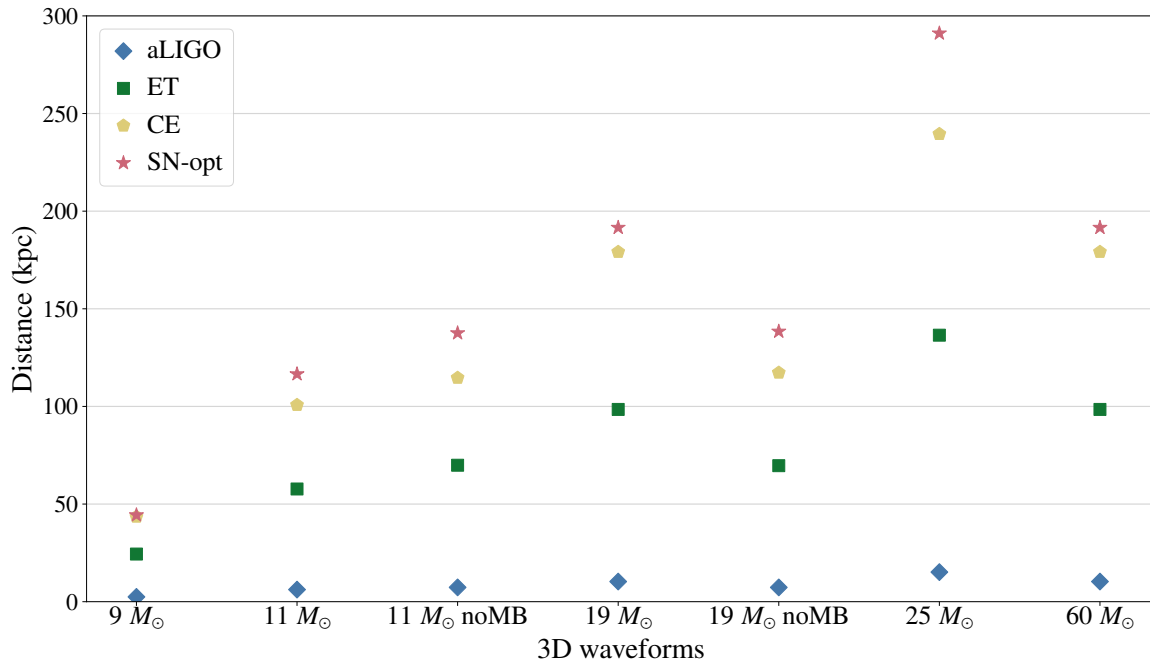
Figure 5: The figure summarizes the distance of the 3D waveforms for different second and third-generation gravitational wave detectors. We see for second-generation advanced LIGO detector that the optimal distances for the 3D numerical waveforms are limited to 10kpc. The optimal distance is so small enough that we are not sensitive to all the galactic supernovae. All the third-generation detectors have optimal distance such that each detector is sensitive enough to detect gravitational waves from galactic CCSNe. However, as evident from the plot above, for a source at a fixed distance, the ET will have the lower SNR as compared to Cosmic Explorer. The supernovae-optimized detector provides approximately a 25% improvement in the SNR as compared to Cosmic Explorer.
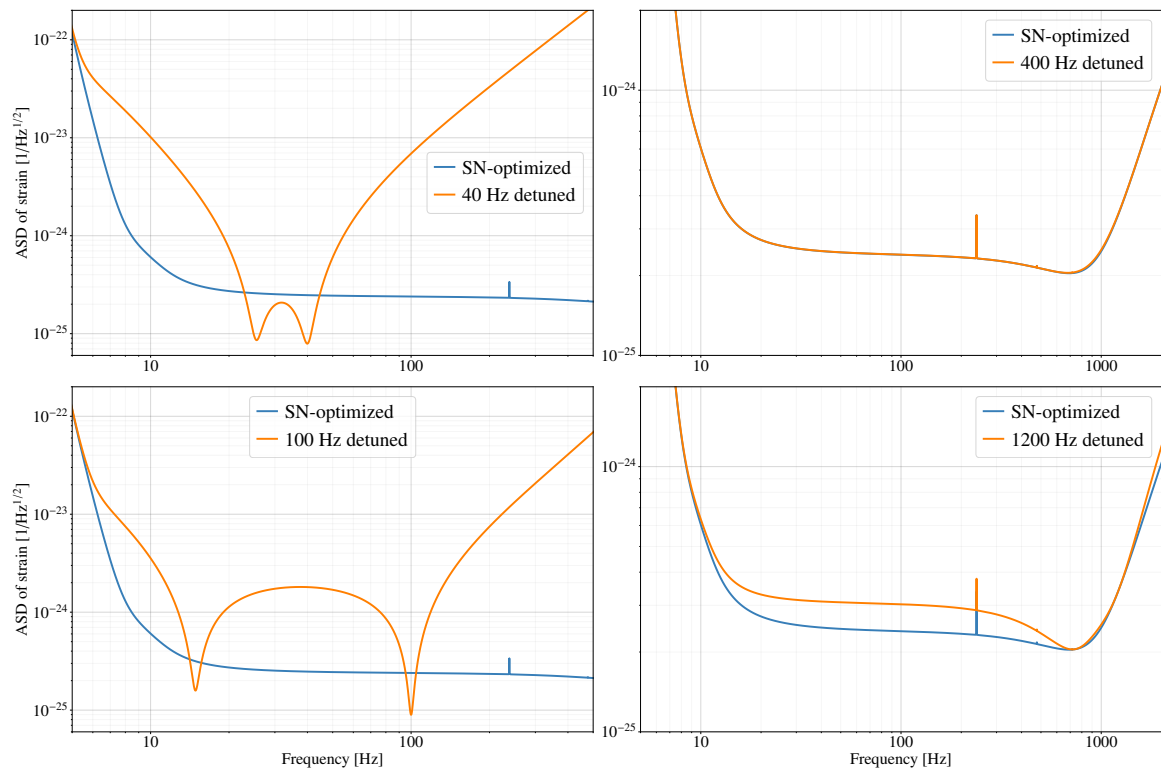
Figure 6: We explore the possibility of detuning the signal recycling cavity to improve the sensitivity towards CCSNe. We find that detuning can be used to improve sensitivity in narrow bins of frequency below 400 Hz. This could, therefore, be used to study the ring-down modes of binary black-holes systems in collaboration with eLISA [3]. However, for improvements to the range of CCSNe, this technique isn't useful.
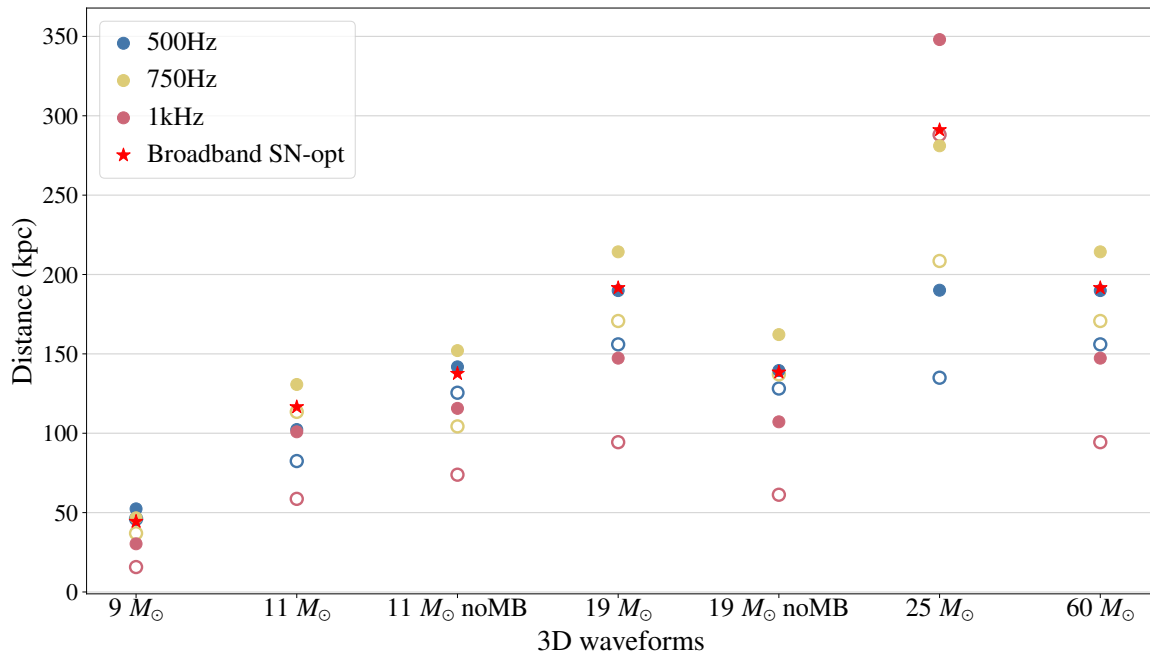
Figure 7: The figure summarizes the optimal distance of the different 3D waveforms for narrow-band detectors at frequencies 500 Hz, 750 Hz and 1000 Hz. The hollow circles denote the narrow-band detectors with a bandwidth of 250 Hz while the filled circles denote the bandwidth of 1600 Hz. The optimal distances from the broadband supernovae-optimized detector are represented as stars. We see tighter narrow-banding with a bandwidth of 250 Hz degrades the performance of the detector. The wider bandwidth of 1600 Hz around the 750 Hz narrow-band detector improves the optimal distances for most of the numerical waveforms.
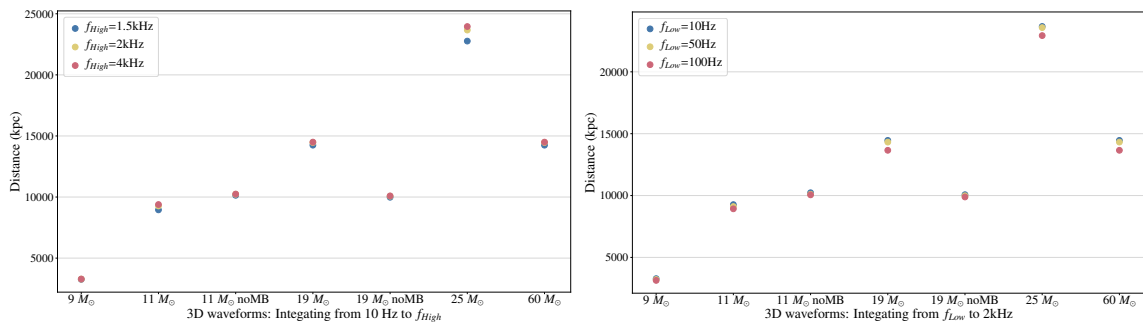
Figure 8: Considering toy detector with a flat PSD of $3 \times 10^{-27}~Hz^{-1/2}$ in range 10 Hz to f_{High} (above) and f_{low} to 2 kHz (below), the figure summarizes the range with the corresponding sensitivity and numerical waveform CCSNe corresponding to their ZAMS mass. We see a broadband detector with a strain sensitivity of $3 \times 10^{-27}~Hz^{-1/2}$ from 200 Hz to 1.5 kHz is desired to achieve the ranges that would correspond to an observed event rate of one per year for gravitational-waves from CCSNe.
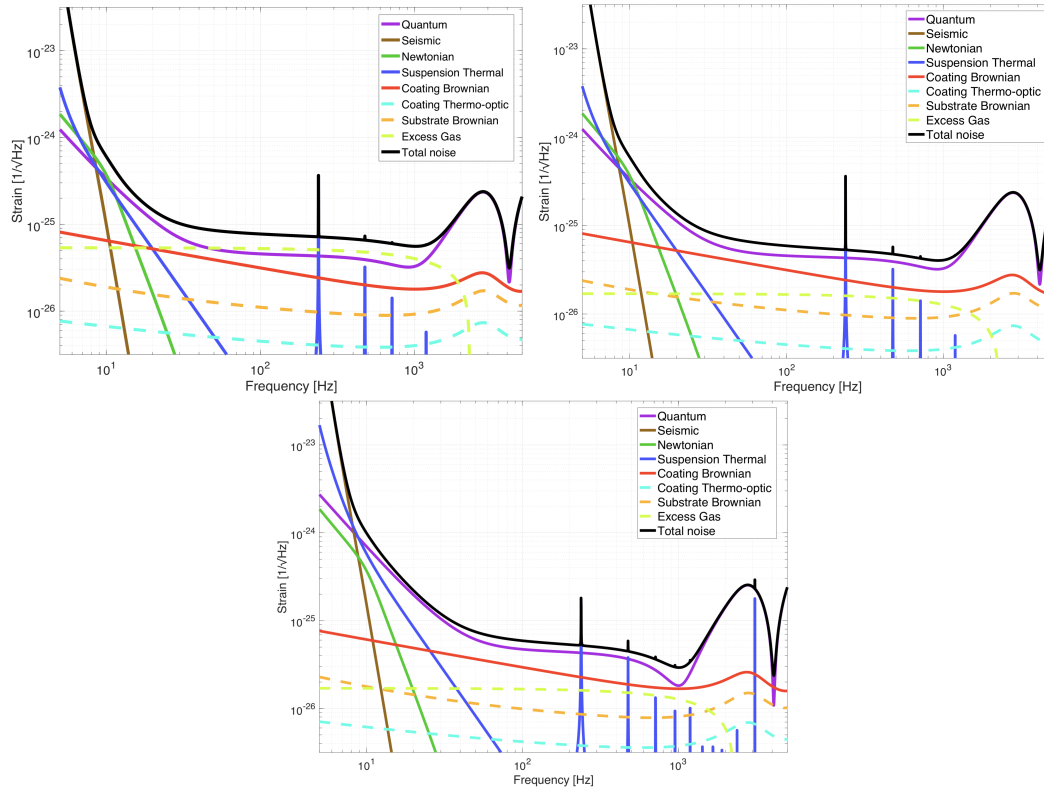
Figure 9: The figure above summarizes the noise budgets for the Hypothetical detector configurations. We see from the figure on the top that the detector's sensitivity is limited by residual gas noise. Therefore, we reduce the residual gas pressure by a factor of ten from CE design. The plot in the middle and bottom plots show optimization results without changing the transmittance of the power recycling cavity and with active changes in the transmittance of the power recycling cavity. Thereby, changing the gain of the power recycling cavity and the finesse of the detector. We will refer to the two detector configurations as Hypothetical-1 and Hypothetical-2 respectively.
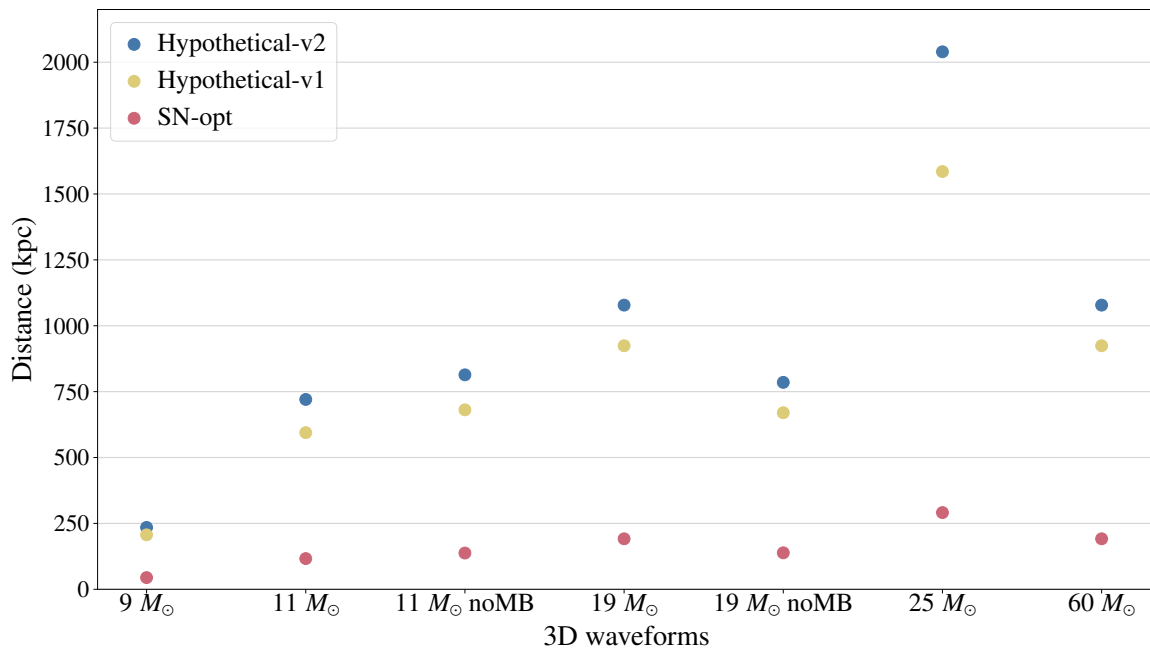
Figure 10: The plot shows with extreme technological upgrades to the third-generation detectors discussed in section §2.5, we optimal distances for the CCSNe is limited to 1Mpc. The event rate for the observation of gravitational waves from CCSNe is still low but improves to one in twenty years.

Parameters	aLIGO	Cosmic Explorer-2	SN Optimized	Hypothetical-1	Hypothetical-2
Input Power	125W	220W	220W	500W	500W
SRM transmission	0.325	0.04	0.015	0.0030	0.0122
ITM transmission	0.014	0.014	0.014	0.0036	0.0269
PRM transmission	0.030	0.030	0.030	0.030	0.0011
L_{src}	55m	55m	175m	30m	260m
Finesse	446.25	447.52	447.52	1745.33	233.33
Power Recycling Factor	40.66	65.32	65.32	94.25	1300.09
Arm power	712.43 kW	2025.70 kW	2025.70 kW	26.06 MW	47.61 MW
Thermal load on ITM	0.386 W	1.150 W	1.150 W	13.094 W	24.180 W
Thermal load on BS	0.051 W	0.253 W	0.253 W	0.008 W	0.080 W
BNS range	173.00 Mpc	4.29 Gpc	3.67 Gpc	5.32 Gpc	5.09 Gpc
BNS horizon	394.83 Mpc	11.05 Gpc	9.49 Gpc	12.97 Gpc	12.53 Gpc
BNS reach	246.06 Mpc	8.54 Gpc	6.90 Gpc	11.56 Gpc	10.80 Gpc
BBH range	1.61 Gpc	6.13 Gpc	6.10 Gpc	6.15 Gpc	6.09 Gpc
BBH horizon	3.81 Gpc	11.86 Gpc	11.85 Gpc	11.85 Gpc	11.70 Gpc
BBH reach	2.54 Gpc	11.73 Gpc	11.73 Gpc	11.72 Gpc	11.52 Gpc
Supernovae range	4.34 kpc	71.95 kpc	94.24 kpc	540.53 kpc	716.03 kpc
Supernovae horizon	9.84 kpc	163.08 kpc	213.61 kpc	1225.22 kpc	1623.06 kpc
Supernovae reach	6.10 kpc	101.04 kpc	132.35 kpc	759.15 kpc	1005.65 kpc
Stochastic Omega	2.36e-09	1.82e-13	2.77e-13	1.1e-13	2.58e-13

Table 3: Summary of All Detectors

2.6   Conclusion

We have shown that it is possible to tune a Cosmic Explorer detector to increase the range to CCSNe by approximately 25%. This range improvement does not translate to an increase in detection rate due to the inhomogeneity of the local universe. Therefore, even optimized third-generation gravitational-wave detectors will be limited to CCSNe sources within our galaxy and the Magellanic Clouds. Assuming the detectors have a duty-cycle of 100% the corresponding event rate of CCSNe is one in fifty years. Incorporating the detector downtime and duty-cycle would further decrease the event rate of observed gravitational-wave signals from CCSNe.

However, if such an event were to occur, the broadband supernovae-optimized detector would improve the SNR by of sources by 25%. This improvement would facilitate help understand the properties of the progenitor star in the rare event of CCSNe observation. The supernovae-optimized detector has a slightly reduced sensitivity to the inspiral of neutron stars, but the high-frequency improvements would benefit the study of post-merger signatures and the late-time behavior of the inspiral.

We find that a gravitational-wave detector would require a strain sensitivity of the order of 3×10^{-27} Hz$^{-1/2}$, over a frequency range from 100 Hz to 1500 Hz in order to guarantee a high rate of CCSNe detection. At this strain sensitivity, as per the current estimates of the BNS background, the stochastic background from BNS mergers would contribute as the fundamental sources of noise [133]. This along with technological challenges discussed in section §2.5 poses significant hurdles in achieving an event rate of one per year for the observation of gravitational-waves from CCSNe based on the present models and knowledge of gravitational-wave emission from CCSNe. The technological requirements for these upgrades are beyond the requirements for the third-generation detector. With drastic improvements of an input laser power of 500 W and a photo-detection efficiency of 1, an order of magnitude improvement in the residual gas noise and coating noise from the Cosmic Explorer design, and assuming minimal optical losses in *Hypothetical* detectors. We find that after optimizing these detector configurations to maximize for the supernovae range the range extends to Andromeda for some of the CCSNe numerical waveforms. The event rate achieved with such a hypothetical detector is one in twenty years.

Chapter 3

Measuring rotation rate and equation of state of the protoneutron star

3.1 Introduction

When the core of a massive star exceeds its Chandrasekhar mass, it begins to undergo gravitational collapse [134, 33, 34, 35]. The core-collapse and subsequent bounce can power a supernovae explosion that radiates light, neutrinos, and gravitational waves (see e.g. Refs. [37, 38, 39, 40] and references therein). Gravitational waves generated during the supernovae travel unhindered through the stellar envelope, carrying information about the structure and dynamics of the collapsing star. Advanced LIGO will be able to detect core-collapse supernovae out to 50 kpc if the cores are rapidly rotating and the explosion is magnetorotationally driven, and to 5 kpc if the explosion is neutrino driven [44, 45]. Cosmic Explorer, a proposed third-generation detector will be able to observe neutrino driven explosion signals out to a few hundred kiloparsecs [46], and the magnetorotationally driven explosion signals out to 2 Mpc. The estimated event rate for core-collapse supernovae in the Milky Way is 1-3 per century [47, 48, 49, 50]. While the probability of observing a signal within the reach of these detectors is low, if the information about the supernova can be extracted from the gravitational waves, it would shed new light on the physical processes of core-collapse.

Significant advances have been made over the last two decades in the simulation

of core-collapse supernovae (see e.g. Refs. [135, 136] and references therein). Abdika-malov *et al.* [52] performed 132 simulations in which they studied the dependence of the gravitational-wave signal at the core bounce and postbounce on the rotational properties of the progenitor core. They quantify rotation of the core by the ratio of the rotational kinetic energy and the gravitational potential energy $\beta = T/|W|$ and find that the gravitational-wave strain amplitude at the bounce primarily depends on β, while the degree of differential rotation only becomes relevant for cores with $\beta \gtrsim 0.08$. They use two equations of state (LS220 and HShen) and explore the difference between the waveforms associated with the two equations of state. Richers *et al.* [51] used the progenitor star identical to Ref. [52] in their simulations. They investigated the dependence of the gravitational-wave signal on the nuclear equation of state. They performed a total of 1764 simulations exploring 18 equations of state and 98 rotation profiles (varying β and differential rotation). They confirm that the gravitational-wave signal at the bounce is most sensitive to β, while the postbounce oscillations depends on the equation of state, which manifests itself through the characteristic frequency of the oscillations, f_{peak}.

Abdikamalov *et al.* attempted to determine if gravitational-wave observations could be used to extract physical information about the core rotation. They constructed a template bank of waveforms spanning the range of rotation rates in their simulations, projected signals against this bank, and found that a signal observed at 10 kpc by Advanced LIGO could be used to constrain β to within 20% when $\beta \gtrsim 0.05$. Heng introduced the idea of using principal component analysis to model a set of supernovae waveforms, rather than using the waveforms themselves as a template bank [137]. Previous studies have used principal component analysis to infer the core-collapse explosion mechanism [138, 139, 140, 141].

Edwards *et al.* [142] used a principal component basis of the Abdikamalov *et al.* waveform catalog and Bayesian parameter estimation [143] to determine if the core rotation β could be extracted from the observation of a signal. Using a linear model, they fit the posterior means of the principal component coefficients to the known values of the physical parameter. Then they sample from the posterior predictive t-distribution to make probabilistic statements about β estimation. They test their method on signals observed in Advanced LIGO with a signal-to-noise ratio of 20 and are able to recover signals with $\beta = 0.02$ with $\beta = 0.05 \pm 0.03$, improving the

accuracy of measurement to $\beta = 0.05 \pm 0.04$ for signals with $\beta = 0.05$, with average 90% credible interval widths of 0.06.

In this paper, we use the waveform catalog of Richers *et al.* to determine how accurately Advanced LIGO and the proposed third-generation detector Cosmic Explorer could extract information about the nuclear equation of state and the progenitor core rotation rate from observations of core-collapse supernovae. Since the progenitor cores of supernovae are expected to be rotating relatively slowly (core rotation periods $\gtrsim 30$ s) [56, 55, 57], we focus on the waveforms in the Richers *et al.* set with $0 \leq \beta < 0.07$. We use a total of 659 waveforms spanning 13 nuclear equations of state. We use principal component analysis to construct a model that captures the features of the Richers *et al.* catalog and construct a map between the parameters measured by the principal component model and the physical parameters of the waveform f_{peak} and β. We use Monte Carlo methods to perform Bayesian parameter estimation to measure the posterior probability distribution of the principal component model parameters and the constructed map to transform these into the posterior probability distributions of the physical parameters.

We find that for sources with $\beta \geq 0.02$ at a distance of 8 kpc, β can be estimated with a 90% credible interval of 0.004 for Advanced LIGO, and 0.0008 for Cosmic Explorer detectors. The precision of measurement for signal sources at 48.5 kpc observed in Cosmic Explorer deteriorates to 90% credible interval of 0.003. We can constrain f_{peak} for sources within the Milky Way galaxy to with 90% credible interval of 5 Hz for detections in the third-generation detectors, if the β for the signal is more than 0.02, thus allowing us to constrain the nuclear equation of state.

This paper is organized as follows: In Sec. 3.2 we describe the the construction of a principal component basis set using the Richers *et al.* waveforms from which we withhold a random sample of 10% to test our method. In Sec. 3.3 we describe the construction of the map between the parameters of the principal component model and the physical waveform. In Sec. 3.4 we describe our Bayesian parameter estimation methods, and in Sec. 3.5 we present the results of the methods using simulated signals in Advanced LIGO and Cosmic Explorer. In Sec 3.6 we summarize our findings and discuss directions for future work.

3.2 Principal Component Analysis

Principal component analysis extracts the dominant features from a set of waveforms as linearly independent principal components [137]. In this study, we use singular value decomposition to compute the principal components. A set of discretely and evenly sampled-in-time waveforms can be written as the columns of a matrix D which can be written as

$$D = U\Sigma V^T, \tag{3.1}$$

where the matrices U and V contain the orthonormal eigenvectors of DD^T and $D^T D$, respectively, and the diagonal matrix Σ contains the eigenvalues of DD^T. The orthonormal vectors in the matrix U are the principal components, and are sorted in decreasing order of the size of the square root of the eigenvalues. Hence, the first principal component describes the most dominant feature in the set of waveforms. If we have N waveforms in the catalog D, then U contains N principal components. By constructing a principal component decomposition of the catalog, we attempt to construct a set of basis vectors that captures the features of signals that lie in the space spanned by the waveform catalog, without requiring modelling every possible core-collapse in the catalog space. The principal component analysis provides us with a semianalytic model for core-collapse waveforms, given by

$$H \approx \sum_{j=1}^{N} \alpha_j U_j, \tag{3.2}$$

where the α_j are the coefficients of the signal H expressed in terms of the basis vectors U_j. We can use Bayesian parameter estimation to construct posterior probability densities on the model parameters α_j and hence the gravitational-wave signal H. However, there are two challenges to directly implementing this approach. First, the number of waveforms used to construct the principal component analysis N must be large enough to accurately explore the features in the catalog (typically of order 10^2–10^3 waveforms), but this N may be significantly larger than the number of basis vectors needed to capture the essential features of the waveforms. Second, the measured α_j are parameters of the basis vectors and are not directly related to physical parameters of the waveforms. As suggested in previous works, we address these challenges in two ways. Since the principal component analysis tells us which basis vectors

capture the dominant features of the catalog, we can construct an approximation to each waveform h as a linear combination of a subset of the principal components

$$h = \sum_{j=1}^{k} \alpha_j U_j. \tag{3.3}$$

where $k < N$. Here, we use two approaches to choose the value of k; we study the overlap between the original waveforms in the catalog and approximations to these waveforms using a subset of basis vectors. If the overlap is unity, then the approximate decomposition exactly reproduces the original waveforms. We use the overlap method to make an initial choice of the number of basis vectors k and then perform parameter estimation to confirm that the choice is sufficient; that is statistical error dominates over the systematic error that arises from choosing $k < N$. Finally, we determine which of the α_i are needed to extract the physical parameters β and f_{peak} and use the catalog to construct the maps $\beta(\alpha_i)$ and $f_{\mathrm{peak}}(\alpha_i)$.

To construct the basis set, we use the axisymmetric general-relativistic hydrodynamic simulations from Richers *et al.* that span 18 different equations of state and 98 rotation profiles [51]. They use a $12 M_\odot$ nonrotating progenitor (model s12WH07 from [144]) in the CoCoNuT code [145, 146] once for each of the 18 equations of state. Richers *et al.* imposed a rotation profile on the progenitor according to the cylindrical rotation law [147]:

$$\Omega(r) = \Omega_0 \left[1 + \left(\frac{r}{A} \right)^2 \right]^{-1}, \tag{3.4}$$

where A (measured in km) depicts the measure of degree of differential rotation, Ω_0 is the maximum initial rotation rate, and r is the distance from the rotational axis in km.

We exclude the prompt convection part of the waveforms when building the principal component basis set. This part of the signal is highly stochastic in nature making it challenging to model with principal component analysis. However, the prompt convection phase is retained in the waveforms that are used as signals to test our method. Richers *et al.* suggest that information on the progenitor core rotation and the equation of state can be extracted from the core bounce and the postbounce oscillations of the protoneutron star. We therefore use the criteria proposed by Richers *et al.* to truncate the waveform 6 ms after the third zero-crossing of the strain waveform after the bounce. We resample the waveforms to 16 384 Hz and ensure that

the length of all waveforms is 1 s by zero padding them with the core bounce aligned at $t = 0.5$ s for all the waveforms. In our analysis, we only use the plus polarization of the waveforms.

The general morphology of the waveforms can be seen in Fig. 11. Prior to the core bounce, the strain increases slowly. It decreases rapidly through the bounce to a local minimum. The depth of the local minimum increases with the rotation rate of the inner core at the time of the bounce. This phase is followed by the postbounce ringdown oscillations of the newly formed protoneutron star, which lasts ~ 6 ms. The characteristic frequency of these oscillations depends on the equation of state of the inner core. The top panel of Fig. 11 shows the waveforms for SFHx equation of state and the rotation rates of the inner core between $\beta = 0.02$ and 0.06. We can see that the depth of the first local minimum immediately after the core bounce increases with the rotation rate. However, the postbounce oscillations have almost the same frequency irrespective of the rotation rate. The bottom panel shows us the waveforms for $\Omega = 2.50$ rad/sec and the precollapse differential rotation rate $A = 467$ km for various equations of state listed in Table 4. We can note that the depth of the first local minimum is nearly the same for waveforms with different equation of state since the rotation rate is the same while the postbounce oscillation frequency is different for different equations of state.

In order to focus on slowly rotating progenitor cores, we restrict the catalog to the set of simulations with $\beta < 0.07$. We also exclude simulations whose equation of state is ruled out by observations of GW170817 [27, 148, 149], giving us 659 waveforms in total. We select 60 waveforms at random from this set and reserve them for testing our methods; these test signals are not included in the construction of either the principal component decomposition or the map between principal component parameters and physical parameters. We construct a principal component basis set from the remaining 599 waveforms. We do not consider the affects of the pre-collapse differential core rotation since Refs. [52] and [51] show that the waveforms for slowly rotating cores are only very weakly dependent on the differential rotation profile. Therefore we consider parameterization of the catalog only by β, regardless of the differential rotation. Figure 12 shows the values of β and f_{peak} of the simulations used to construct the principal component analysis and map (crosses) and and the signals reserved to test our method (dots).

Figure 13 shows the reconstruction of each of the 599 waveforms using the principal component basis set. The horizontal axis represents the number of principal components k used to generate the waveform by Eq. 3.3 and the vertical axis represents the overlap between the original catalog waveform H and the approximate reconstructed waveform h for each value of k, where the overlap between is defined as [150]:

$$\langle H|h \rangle = 4\mathbb{R} \int_0^\infty \frac{\tilde{h}(f)\tilde{H}(f)}{S_n(f)} \, \mathrm{d}x, \tag{3.5}$$

where $\tilde{H}(f)$ and $\tilde{h}(f)$ are the Fourier transforms of the waveforms and $S_n(f)$ is the power spectral density of the Cosmic Explorer (CE1) detector noise. This figure shows that by using the first 50 of the 599 principal components, we are able to reconstruct the all 599 original waveforms with more than 90% overlap. However, we find that using 50 basis vectors in the Bayesian parameter estimation is computationally expensive and note that if only 15 basis vectors are used, 96% of the waveforms are reconstructed with an overlap greater than 90%. In Fig. 12 the catalog waveforms for which 15 basis vectors are sufficient to reconstruct the overlap to $\geq 90\%$ are shown with blue crosses and the catalog waveforms that fail this criteria are shown with green crosses. We see that all the waveforms that require more than fifteen principal components to reproduce the waveform with at least 90% overlap lie in the region of slowest core rotation β. These are the waveforms for which it is most challenging to extract β and f_{peak} [51]. However, we still include these waveforms in our analysis.

Previous studies have used principal component analysis to construct a gravitational-waveform model for rotating core-collapse supernovae that is used for Bayesian reconstruction of the signal observed in the detector. Röver *et al.* [143] also used overlaps between the original waveforms and the waveforms generated through a subset of principal component basis to determine the number of basis vectors to be used in their waveform model. They used 128 waveform simulations from Dimmelmeier *et al.* [53] to construct their basis set and used 10 basis vectors. Edwards *et al.* [142] used a constrained optimization approach to select the number of basis vectors in their study. They used 132 waveforms in the Abdikamalov *et al.* catalog [52] to construct their basis set and used the first 14 of the basis vectors in their model.

3.3   Mapping to physical parameters

Having constructed a principal component model and determined that fifteen basis vectors are adequate to capture the essential features of the catalog space, we construct a map between the unphysical parameters of our model α_j and the physical parameters of interest β and f_{peak}. The ratio of the rotational kinetic energy to the gravitational potential energy of the inner core β, is a robust way of quantifying the rotation rate of the inner core [52, 51]. β is a time dependent quantity that evolves during the core-collapse event. In our work we quantify the rotation rate of the core of the progenitor with β at the time of the core bounce.

Fig. 14 shows the values of the coefficients of the first four principal components α_i ($i = 1, 2, 3, 4$) as a function of the rotation rate β for the waveforms in the catalog. We see that α_1 is the parameter most strongly correlated with β, exhibiting a roughly linear dependence across the catalog space. The increase in the spread of points in α_1 as β increases is caused by waveforms with similar values of β but different equations of state; the change in equation of state weakly affects the map between the two parameters. The correlation between the other three model parameters and β is not as obvious. We use the data shown in Fig. 14 to construct a map $\beta(\alpha_1, \ldots, \alpha_k)$, where $k \leq 8$.

To construct the map using just the first model parameter $\beta(\alpha_1)$, we use the least square fit for a straight line, obtaining the slope 0.0326 and the intercept 0.0007. If we want to incorporate more than one model parameters to construct the map, we use interpolation to find $\beta(\mathbf{A})$ for an arbitrary point $\mathbf{A} = (\alpha_1, \ldots, \alpha_n)$ with $2 \leq n \leq 8$ using the known values of β and $(\alpha_1, \ldots, \alpha_n)$. This interpolation is performed using the linear method of `scipy.interpolate.griddata` which finds the convex hull of $\mathbf{A}$, which consists of the nearest $n + 1$ neighbours of $\mathbf{A}$ that contain $\mathbf{A}$: $\mathbf{A_1}, \ldots, \mathbf{A_{n+1}}$, for which the β values are known. $\mathbf{A}$ can be written as a weighted average of $\mathbf{A_1}, \ldots, \mathbf{A_{n+1}}$:

$$\mathbf{A} = \sum_{i=1}^{n+1} \gamma_i \mathbf{A_i}, \tag{3.6}$$

where $\gamma_i > 0$ and $\sum \gamma_i = 1$. The map for an arbitrary point is then generated using

the linear interpolation with the γ_is as the weights in the interpolation:

$$\beta\left(\mathbf{A}\right) \approx \sum_{i=1}^{n+1} \gamma_i \beta\left(\mathbf{A}_i\right). \tag{3.7}$$

The interpolation fails if $\mathbf{A}$ does not lie within a convex hull of points with known values of β. Finding the convex hull of $\mathbf{A}$ becomes increasingly computationally expensive as the number of model parameters (and hence, the number of dimensions) used in the interpolation increases. To determine how many model parameters should be used in the map to construct a robust and sufficiently accurate map, we perform the following test. We first note that since our waveform catalog is large, the omission of one waveform from the construction of the principal component basis does not significantly change the principal component decomposition. Given this, we can exclude a waveform from the principal component analysis, construct the interpolation function using the remaining waveforms, and use this interpolating function to estimate the known value of β for the waveform excluded from our algorithm. We repeat this procedure for each of the waveforms in the catalog used to construct the principal component basis and the interpolation function. Note that we do not use the 10% of the catalog reserved for astrophysical testing here, as we reserve those waveforms for use until our method is fully tuned.

The outcome of this test is shown in Fig. 15. The horizontal axis shows the number of model parameters used to construct the map $\beta(\alpha_1, \ldots, \alpha_k)$ for $k \leq 8$. The median error in reconstructing β from each of these maps for the waveforms in the catalog is plotted on the vertical axis. The failure rate of interpolation corresponding to each map is also shown. We see that as the number of model parameters used to construct the map increases, the interpolation error decreases. Maps that use interpolation with two or more model parameters have significantly less error as compared to the map $\beta(\alpha_1)$ constructed using the least square fit. Hence we do not use the map $\beta(\alpha_1)$ in our analysis. However, with increasing number of model parameters, the failure rate for interpolation also increases. The interpolation fails for more than 80% of the cases when we use eight model parameters. The failure rate of the map constructed by using nine model parameters or more is even higher and we do not consider that in our analysis. We also note that the error in reconstruction of β using the interpolation increases as β increases. This can be attributed to the fact that that the volume of parameter space sampled is sparser as β increases.

We use the maps $\beta(\alpha_1, ..., \alpha_k)$ with $k \leq 8$ to translate the posteriors obtained for the model parameters from the Bayesian inference of simulated signals to the posteriors on β. We constrain the samples to be in the convex hull of the first two model parameters, as shown in Fig. 16 in order to successfully interpolate using the first three parameters. We first use the map constructed by using eight model parameters, which would result in some samples in the posteriors getting rejected because of the failure in interpolation. We then use the map formed by seven model parameters for the samples for which the interpolation failed previously, and repeat the procedure with maps constructed using fewer model parameters for the samples for which interpolation fails. Eventually, all the remaining samples are successfully interpolated by using the map $\beta(\alpha_1, \alpha_2, \alpha_3)$. Constraining the samples within the convex hull using four parameters or higher is computationally expensive. A much more robust map can be constructed by using machine learning and by populating the parameter space with more simulations. We leave the construction and testing of that map for future work.

The postbounce oscillation frequency f_{peak} is the $l = 2$ $f-$mode peak frequency of the protoneutron star after the core bounce [151, 152]. Richers *et al.* observed that for simulations with $0.02 \leq \beta \leq 0.06$, f_{peak} for a given nuclear equation of state is independent of the value of β (see Fig. 12), with the softer equations of state having a higher postbounce oscillation frequency. We use this relation between f_{peak} and the equation of state, shown in Table 4, to infer the equation of state dependence on f_{peak}. To measure f_{peak}, in our analysis, we the method of Richers *et al.* We first isolate the postbounce oscillation from the earlier bounce and the later convection phases of the waveform by taking the Fourier transform of the waveform up to the end of the bounce phase t_{be} (taken to be the third zero crossing after the core bounce) and, separately, the Fourier transform of the waveform up to $t_{\text{be}} + 6$ ms, in order to include a few cycles of the postbounce oscillations and isolate them from the convective phase. The Fourier transform of the waveform up to the bounce phase is subtracted from the Fourier transform that includes postbounce oscillations and the largest spectral feature within the window 600 - 1075 Hz is f_{peak}. As found by Richers *et al.*, for slowly rotating cores with $\beta \leq 0.02$ this method to extract f_{peak} is unreliable since the protoneutron star oscillations are only weakly excited. For $\beta \geq 0.06$, centrifugal forces start affecting the postbounce oscillations and the f_{peak}

Equation of State	f_{peak} Mean value [Hz]	f_{peak} Standard deviation [Hz]
SFHo	772.1	5.6
SFHx	768.9	6.2
LS180	728.4	6.4
HSIUF	724.2	8.4
LS220	723.7	6.4
GShenFSU2.1	723.2	11.1
GShenFSU1.7	721.1	10.3
LS375	709.1	8.1
HSTMA	704.1	5.7
HSFSG	702.1	7.9
HSDD2	701.6	8.3
BHBLP	699.7	8.6
BHBL	699.7	8.2

Table 4: The mean and standard deviation of the f_{peak} values of the waveforms used to form the principal component basis belonging to a particular equation of state with $0.02 \leq \beta \leq 0.06$.

value depends on differential rotation in addition to the equation of state.

In our analysis, we measure f_{peak} of a signal observed in a detector by applying the method of Richers *et al.* to the waveform reconstructed by our Bayesian parameter estimation. For each sample in our posterior probability distribution, we construct the approximate signal given by Eq. 3.3 using all 15 measured principal component parameters. We then determine the postbounce oscillation frequency using the the approximate posterior waveform. Evaluating f_{peak} for all the samples gives a posterior probability distribution for f_{peak}. Comparing the posterior with Table 4 enables us to rule out the equations of state inconsistent with the signal waveform. In this way gravitational waves from core-collapse provide us a different regime than binary neutron star mergers to study the nuclear equation of state.

3.4   Parameter Estimation

By combining the methods described above with Bayesian parameter estimation [153, 154] we can estimate the posterior probability distributions for the physical parameters of astrophysical signals. Our Bayesian parameter estimation samples the probability of the modeled parameter values given a model and set of detectors' data using Markov Chain Monte Carlo methods. We calculate the posterior probability density function, $p(\vec{\vartheta}|\vec{d}(t), H)$, for the set of parameters $\vec{\vartheta}$ for the gravitational-waveform model, H, given the gravitational-wave data from the detectors $\vec{d}(t)$

$$p(\vec{\vartheta}|\vec{d}(t), H) = \frac{p(\vec{d}(t)|\vec{\vartheta}, H)p(\vec{\vartheta}|H)}{p(\vec{d}(t)|H)}, \tag{3.8}$$

where $p(\vec{\vartheta}|H)$ is the prior—the assumed knowledge of the distributions for the parameters $\vec{\vartheta}$ describing the signal, before considering the data. $p(\vec{d}(t)|\vec{\vartheta}, H)$ is the likelihood—the probability of obtaining the data $\vec{d}(t)$ given the model H with parameters $\vec{\vartheta}$. We use the Gaussian likelihood in this analysis, which is given by [155]:

$$p(\vec{d}(t)|\vec{\vartheta}, H) = \exp\left[-\frac{1}{2}\sum_{i=1}^{N}\langle\tilde{n}_i(f)|\tilde{n}_i(f)\rangle\right]$$

$$= \exp\left[-\frac{1}{2}\sum_{i=1}^{N}\langle\tilde{d}_i(f) - \tilde{s}(f, \vartheta)|\tilde{d}_i(f) - \tilde{s}(f, \vartheta)\rangle\right] \tag{3.9}$$

where N is the number of detectors (in our case, $N = 1$), and $\tilde{d}_i(f)$ and $\tilde{n}_i(f)$ are the Fourier transforms of the data and the noise in the detector. We sample the posterior probability distribution using stochastic sampling methods. Our choice of sampler in `PyCBC Inference` [156] is guided by the fact that the default parallel tempered MCMC sampler `emcee_pt` [157, 158, 159] can experience problems converging for signals with signal-to-noise ratios greater than 100. To address this, we use the dynamic nested sampling package `Dynesty` [160, 161, 162] which provides posterior probability distributions for all the signals explored here. For signals with very high signal-to-noise ratio, the detector noise becomes negligible and so it is possible to obtain a point estimate of the signal parameters by directly computing the inner product between the signal and the basis vectors. By performing this spot-check for the high signal-to-noise ratio signals, we find that these point estimates agree with the posteriors obtained by the `Dynesty` sampler.

In our analysis, we assume that any gravitational-wave signal from a core-collapse supernova will be accompanied by a neutrino signal detected by neutrino observatories such as IceCube [163], Super-Kamiokande [164] or DUNE [165]. The neutrino observations can estimate the time of the core bounce to within $3-4$ ms [166, 38, 167]. Our analysis only considers the core bounce and the next $5-7$ ms, and we use assume that information from the neutrino observations can provide a narrow prior of 8 ms for the time of the bounce. We also assume that the distance and sky location to the source are known and we do not include them in the parameter estimation.

We use `PyCBC Inference` [156] to obtain posteriors for the coefficients of the first fifteen principal components of the waveform catalog. We use uniform priors for all the fifteen coefficients as shown in Table 5, in addition to the constraint that the samples are restricted with the convex hull formed by the point cloud of the first three model parameters for the waveforms in the catalog. Using the map discussed in section 3.3 and the methods to extract f_{peak} values, we translate the posteriors on the coefficients to posteriors on β and f_{peak}.

3.5 Results

We test our method using the 60 signal waveforms reserved from above. Each waveform, consisting of the core-collapse, postbounce oscillation, and prompt convection

Parameter	Lower bound on prior	Upper bound on prior
α_1	0.0	10.5
α_2	-5.0	3.55
α_3	-2.0	2.0
α_4	-1.5	2.0
α_5	-1.0	1.75
α_6	-0.85	1.05
α_7	-0.75	1.5
α_8	-0.75	0.75
α_9	-0.75	0.75
α_{10}	-0.75	0.75
α_{11}	-0.75	0.75
α_{12}	-0.75	0.75
α_{13}	-0.75	0.75
α_{14}	-0.75	0.75
α_{15}	-0.75	0.75
t_{bounce}(GPS time)	1126259469.517	1126259469.525

Table 5: Upper and lower bounds on the uniform priors used for the model parameters α_i and t_{bounce} in Bayesian parameter estimation. The values for α_i were chosen based on the range of values obtained from the construction of principal component basis set. t_{bounce} has a uniform prior width of 8ms. All signals are aligned such that the bounce is at $t_{\mathrm{GPS}} = 1126259469.5 + 0.02125$ where 0.02125 is the light travel time between the center of the Earth and the detectors. Note that an additional constraint on the priors is to restrict the samples with the convex hull formed by the first three model parameters of the waveforms in the catalog (see Sec. 3.3).

phases, is used to create a simulated observation by adding it to Gaussian noise colored to the strain sensitivity of the Advanced LIGO detectors and the third-generation detectors: Cosmic Explorer 1 (CE1), and Cosmic Explorer 2 (CE2). Cosmic Explorer is the proposed third generation detector which is planned to begin observing in 2030s [168]. The first stage of the observatory, Cosmic Explorer 1, is the scaling up of the Advanced LIGO technologies to an interferometer with 40 km arm length. The second stage of the observatory, Cosmic Explorer 2, will be an upgrade on the core optics of Cosmic Explorer 1 by using cryogenic technologies and new mirror substrates. The predicted noise power spectral densities of the three detectors used in this study are shown in Fig. 17. We place the sources at distances corresponding to the center of the Milky Way galaxy (8 kpc), far edge of the Milky Way from the Earth (23 kpc), the Large Magellanic Cloud (48.5 kpc), and out to 242 kpc to capture the dwarf satellite galaxies of the Milky Way in the local group. In addition, we place the sources at the distances of 40.5 kpc and at 115 kpc. The sources are assumed to be optimally oriented for the detector. The signal-to-noise ratio of the signal waveforms and its variation with β is plotted in Fig. 18. We do not perform the analysis if the simulated signal has a signal-to-noise ratio less than 8 (shown as purple points in the figure). We note that more sensitive interferometers are able to detect more number of signals with low β. Advanced LIGO is not able to detect any sources at 115 kpc or beyond. It is also unable to detect the sources with $\beta < 0.02$ at 40.5 kpc and beyond. The signal-to-noise ratios and detection ranges in our study are consistent with those obtained for comparable signals in previous core-collapse supernovae search studies [45, 44].

We summarize our results in Tables 6, 7. We measure the median values and the 90% credible intervals from the posteriors obtained from MCMC for β and f_{peak}. The width of 90% credible intervals show how precisely we can measure the parameters. 90% credible interval of f_{peak} is useful to determine the equations of state consistent with the signal, using Table 4. The mean of the median values provides an estimate of the accuracy of the measurement of the parameters. We present our results by classifying the signals in two sets: $\beta < 0.02$, and $\beta \geq 0.02$.
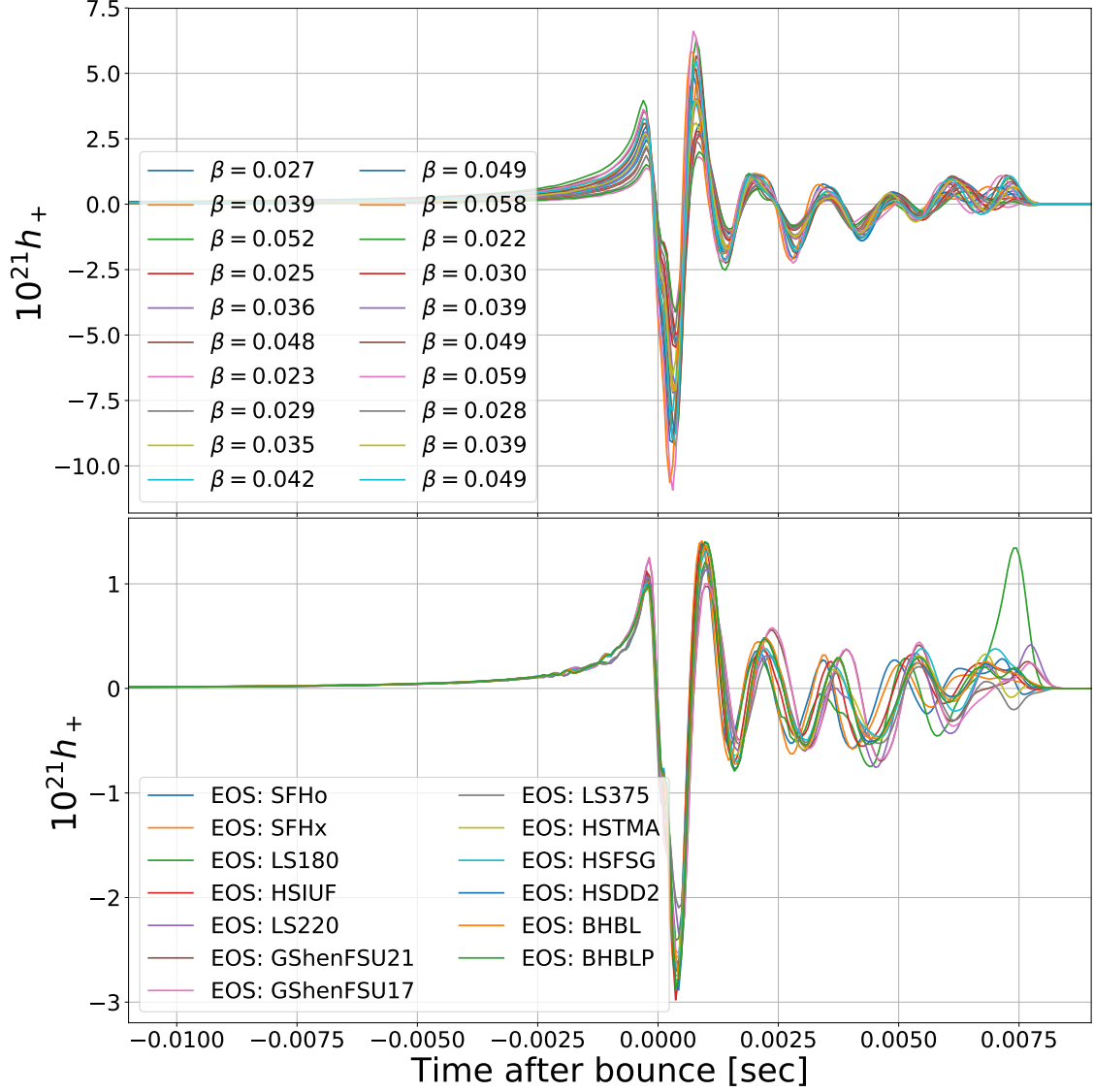
Figure 11: Gravitational wave strain assuming the distance to the progenitor of 10 kpc as function of time for bounce and postbounce oscillation phases of a core-collapse process. The waveforms are zero buffered to make them 1 second long, and the time of bounce is aligned at 0.5 seconds for all the waveforms. The top panel shows the waveforms for the $\texttt{SFHx}$ equation of state with varying rotation rates between $\beta = 0.02$ and $\beta = 0.06$. The strain amplitude at the bounce increases with increasing β, while the postbounce oscillation frequency remains almost the same for all the waveforms corresponding to a given equation of state. Bottom panel shows the waveforms for $\Omega = 2.50$ rad/sec and $A = 467$ km for the equations of state listed in Table 4. The bounce amplitude remains almost the same for the waveforms with the same core rotation rate, while the postbounce oscillation frequency varies for different equations of state.
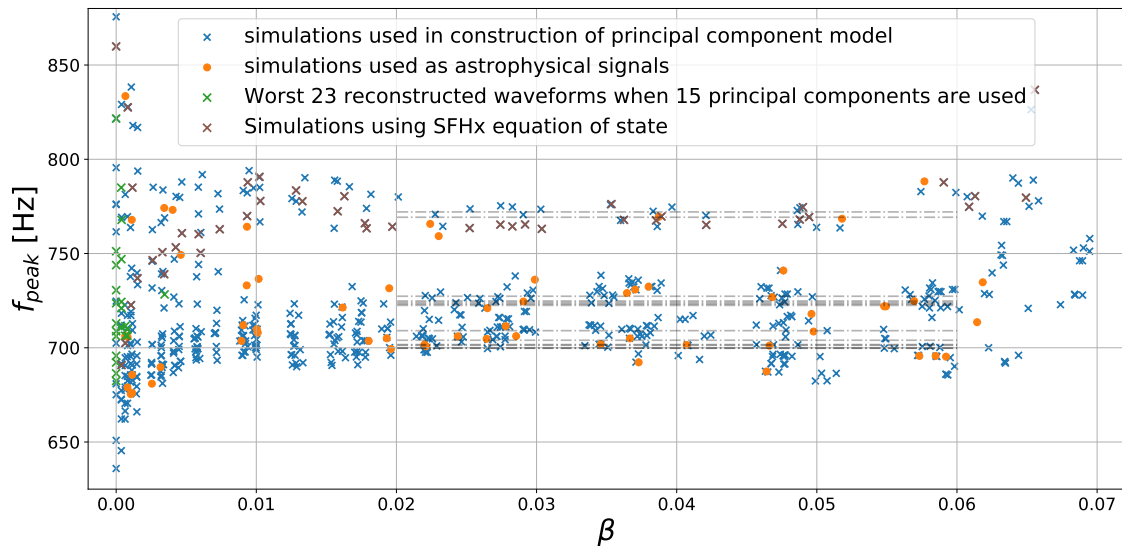
Figure 12: Frequency of postbounce oscillations is plotted on the vertical axis against β of the waveforms on the horizontal axis. The crosses represent the waveforms that are used to build the principal component basis. This also includes the green crosses, showing the waveforms that are affected the most by only considering 15 principal components and not more. The simulations that use the SFHx equation of state are shown in brown crosses. The f_{peak} value for a given equation of state is independent of β for $0.02 \leq \beta \leq 0.06$. The dashed lines represent the average f_{peak} values of the waveforms of a given equation of state in this range, also given in Tab. 4.The orange dots represent the parameter values of the waveforms that are used as astrophysical signals in this study.
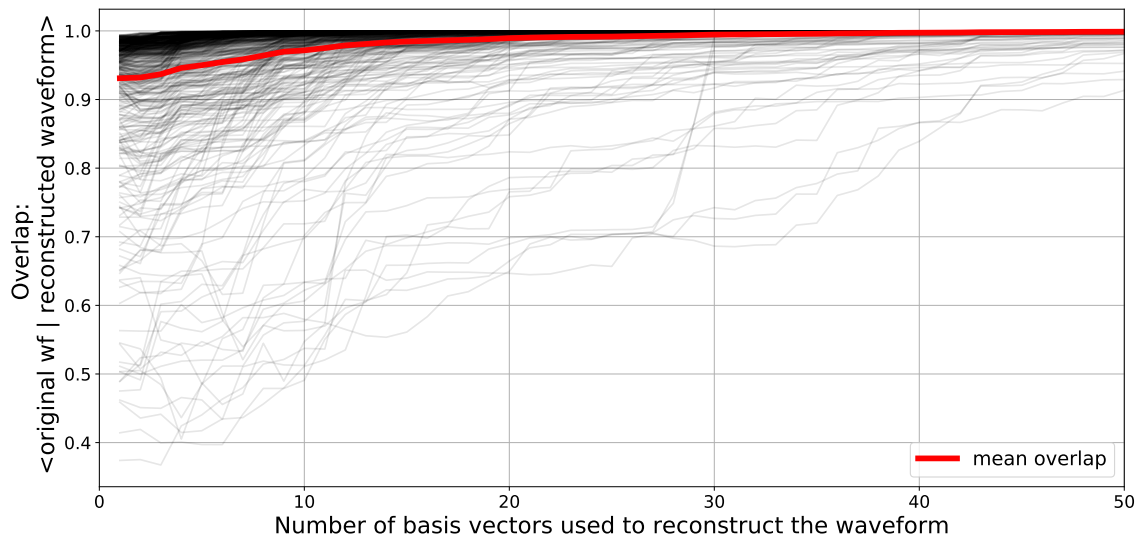
Figure 13: The plot shows how well can a given number of principal components (plotted on the horizontal axis) reconstruct the original waveform. We quantify this by computing the overlap between the original waveform and the reconstructed waveform, and show it on the vertical axis. Each of the waveforms is represented by a grey line, and the mean overlap of all the waveforms as a function of number of basis vectors used for construction is represented by the red line.
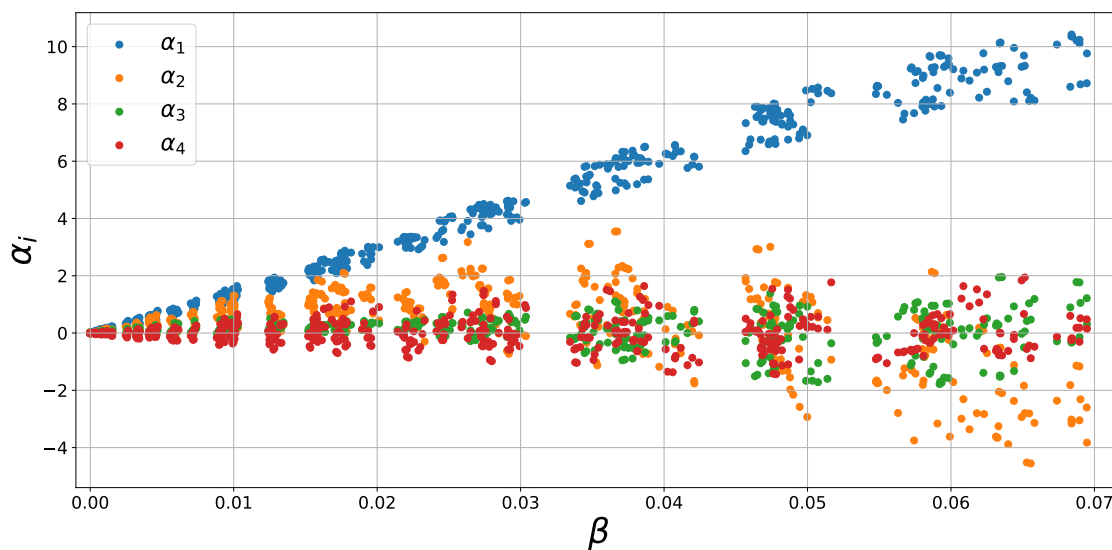
Figure 14: The coefficients of the first four principal components as a function of β. The coefficient of the first principle component, α_1 (shown in blue) is most strongly correlated with β, exhibiting a roughly linear relation. The correlation between the other three coefficients and β can be seen to be weaker. The values of the coefficients spread as β increases because of different equations of state used in simulation of the waveforms.
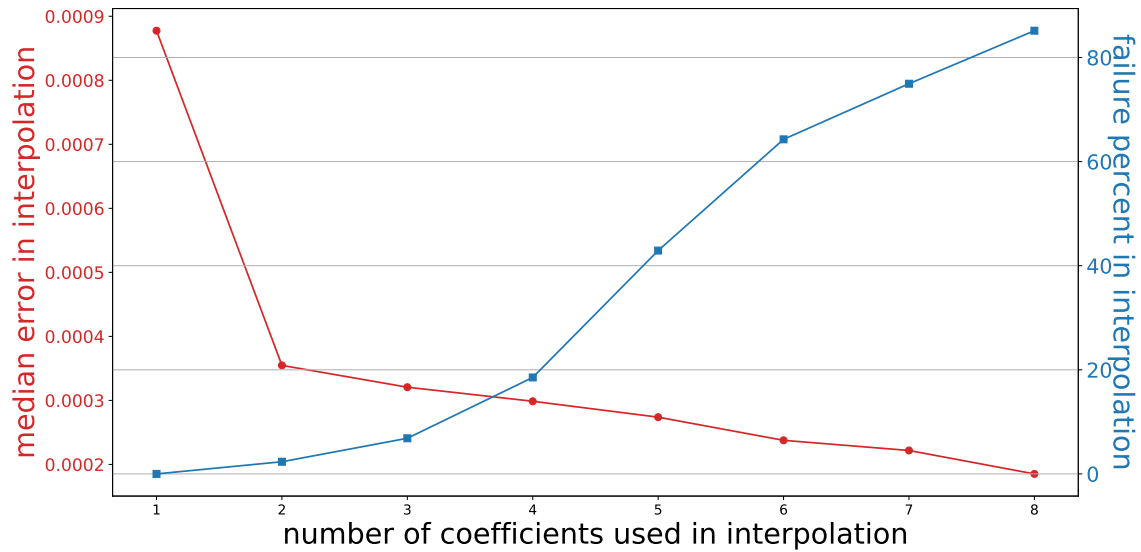
Figure 15: For each waveform in the catalog, a principal component basis set is constructed using all remaining waveforms. Using this basis set, $\beta(\alpha_1, \ldots, \alpha_k)$ maps are constructed using interpolation with the first $k = 2, \ldots, 8$ model parameters, and β of the excluded waveform is estimated using these maps. Least square fit for a straight line is used while using just the first model parameter to construct the map $\beta(\alpha_1)$. The median error in reconstructing β through various maps and the respective failure rate in interpolation are plotted on the vertical axes. Using more number of model parameters reduces the error in interpolation, however increases the number of times the interpolation fails.
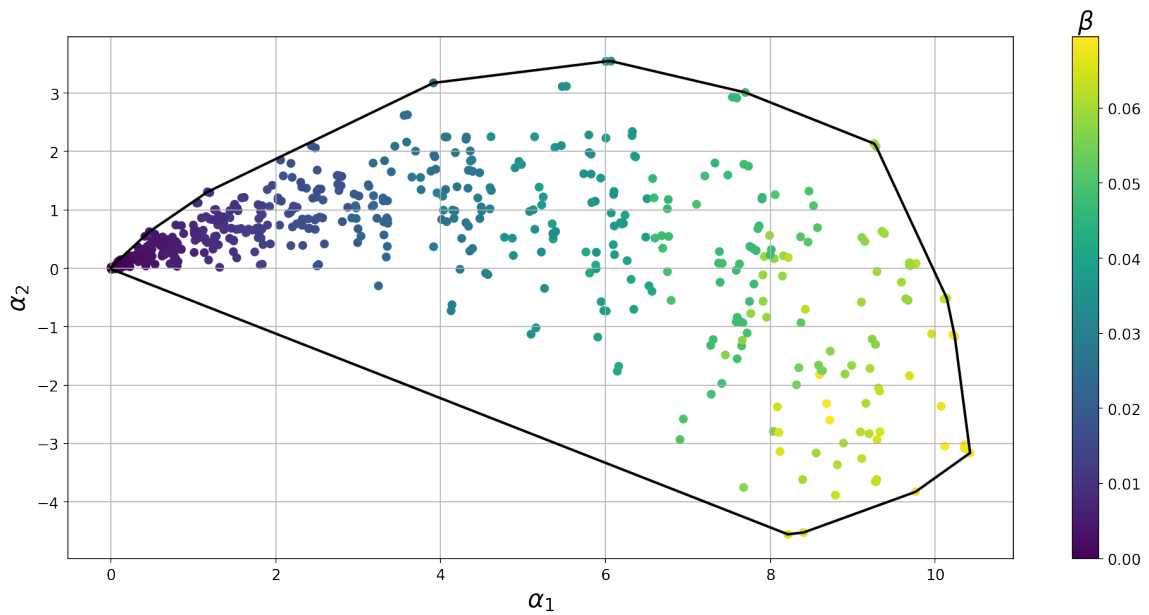
Figure 16: The α_2 (vertical axis) vs α_1 (horizontal axis) parameter plane for the waveforms in the catalog. The colorbar shows the β corresponding to each of the waveforms. The two dimensional convex hull of the all the points is shown by the dashed black line. Interpolation fails for a point outside the convex hull. We can construct a three dimensional convex hull if we also incorporate α_3. We constrain our MCMC samples to be within the three dimensional convex hull.
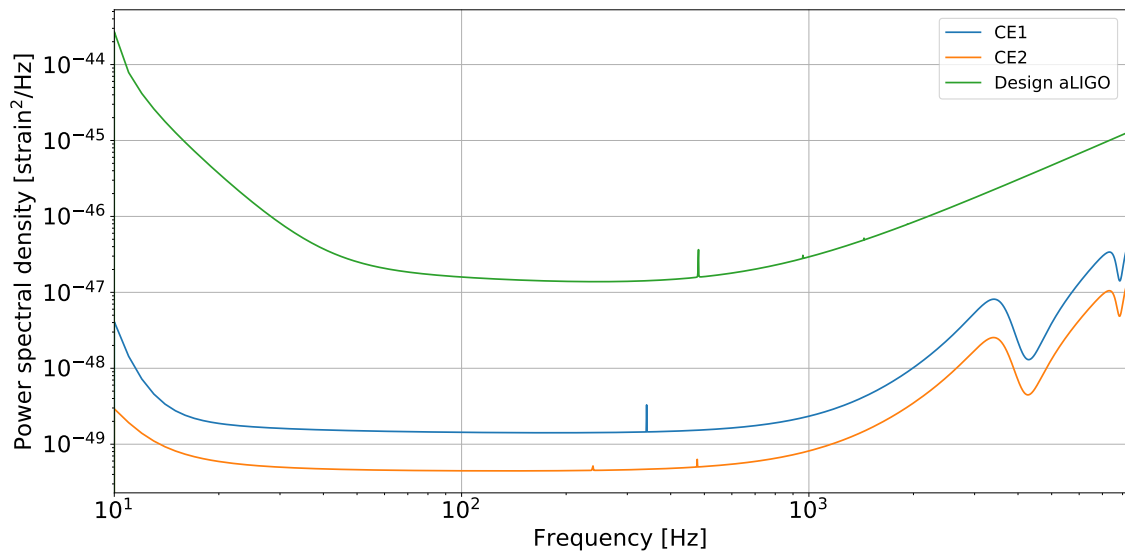
Figure 17: Predicted noise power spectral densities for Advanced LIGO, Cosmic Explorer 1, and Cosmic Explorer 2 detectors.
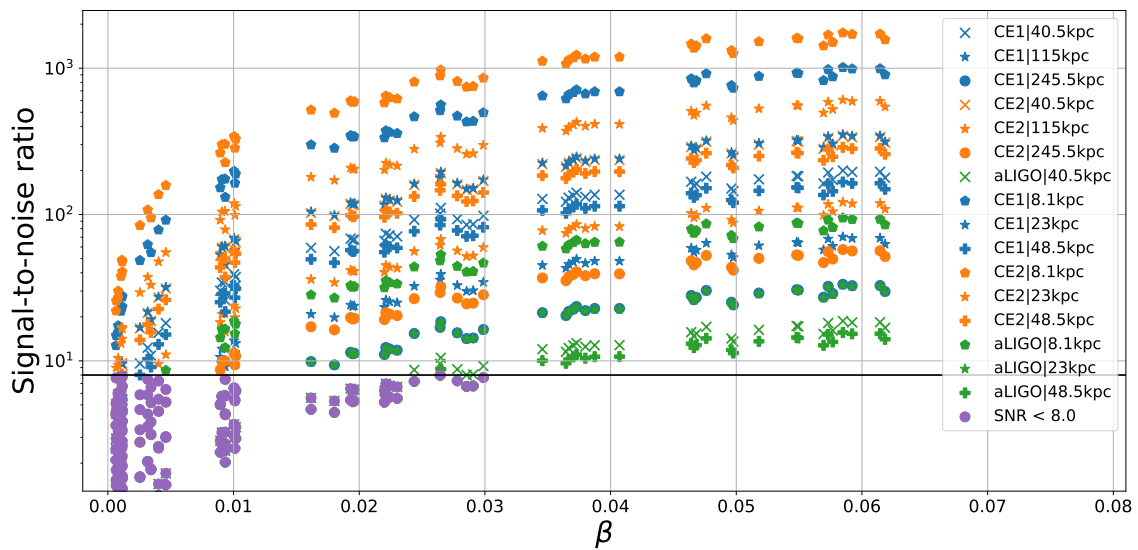
Figure 18: The vertical axis shows the signal-to-noise ratios of waveforms used as astrophysical signals. The horizontal axis shows the β of the core progenitor at bounce. These sources are assumed to be at distances of 8.1 kpc, 23 kpc, 40.5 kpc, 48.5 kpc, 115 kpc, and 242 kpc and the signals are observed in the Cosmic Explorer 1 (CE1), Cosmic Explorer 2 (CE2), and Advanced LIGO (aLIGO) gravitational wave detectors. We ignore the waveforms with signal-to-noise ratios below 8 (shown as purple dots) and do not perform parameter estimation on them.

Detector	Source distance [kpc]	β range	Number of signals	β		f_{peak}	
				Mean 90% credible interval	Mean fractional error	Mean 90% credible interval [Hz]	Mean fractional error
Advanced LIGO	8	$\beta < 0.02$	13	0.004	22 %	289	26 %
		$\beta \geq 0.02$	35	0.004	10 %	7	4 %
	23	$\beta < 0.02$	5	0.01	19 %	780	3 %
		$\beta \geq 0.02$	35	0.009	13 %	39	4 %
	48.5	$\beta < 0.02$	0	–	–	–	–
		$\beta \geq 0.02$	25	0.02	12 %	57	3 %

Table 6: The table here, along with Table 7, summarizes the results of parameters estimation of β and f_{peak} for signal sources at 8 kpc, 23 kpc, 48.5 kpc, and 242 kpc. We have categorized the results for the all the signals on basis of the detector they are observed in, their distance and the corresponding value of β. We present the mean of the 90% credible interval widths and the mean value of the errors and from the posteriors obtained for f_{peak} and β. The average 90% credible interval width of β for sources at 8 kpc observed in Advanced LIGO is 0.004, while for the third generation detectors its an order of magnitude less. The precision to which β can be measured decreases when the β of the signal waveform increases, or the source distance increases. Note that the method to measure f_{peak} for signals with $\beta < 0.02$ is unreliable. We include these results here for completeness.

Detector	Source distance [kpc]	β range	Number of signals	β Mean 90% credible interval	β Mean fractional error	f_{peak} Mean 90% credible interval [Hz]	f_{peak} Mean fractional error
Cosmic Explorer 1	8	$\beta < 0.02$	25	0.0004	26 %	37	18 %
	8	$\beta \geq 0.02$	35	0.0008	6 %	2	3 %
	23	$\beta < 0.02$	20	0.001	21 %	147	11 %
	23	$\beta \geq 0.02$	35	0.002	6 %	5	3 %
	48.5	$\beta < 0.02$	17	0.002	15 %	167	5 %
	48.5	$\beta \geq 0.02$	35	0.003	7 %	11	3 %
	242	$\beta < 0.02$	5	0.007	6 %	205	2 %
	242	$\beta \geq 0.02$	35	0.009	8 %	64	2 %
Cosmic Explorer 2	8	$\beta < 0.02$	25	0.0002	27 %	4	21 %
	8	$\beta \geq 0.02$	35	0.0005	7 %	1	3 %
	23	$\beta < 0.02$	24	0.0005	24 %	120	14 %
	23	$\beta \geq 0.02$	35	0.001	7 %	3	3 %
	48.5	$\beta < 0.02$	18	0.001	18 %	22	10 %
	48.5	$\beta \geq 0.02$	35	0.002	7 %	6	3 %
	242	$\beta < 0.02$	11	0.004	8 %	227	3 %
	242	$\beta \geq 0.02$	35	0.006	8 %	51	3 %

Table 7: Same as Table 6, but for Cosmic Explorer 1 and Cosmic Explorer 2.

The mean width of the 90% credible interval for β for signals sources at the center of the Milky Way with $\beta = 0.04$ is 0.004 when observed in Advanced LIGO, improving to a width of 0.0008 if observed in Cosmic Explorer detectors. For sources at 48.5 kpc it increases to 0.02 for Advanced LIGO detections and 0.003 for Cosmic Explorer detections. We note that the width of the 90% credible intervals increases as the source distance increases. In addition to that, as the value of β of the injected signal increases the 90% credible interval width also increase, even though the signal-to-noise ratio also increases. As discussed in Sec. 3.3, this is because the coefficients for known values of β used to construct the map become sparse for higher values of β and the interpolation suffers. On an average, the 90% credible interval width for signals observed in Cosmic Explorer 1 is 1.5 times that of the signals observed in Cosmic Explorer 2. Fig. 19 shows the 90% credible interval width of the posteriors of β as a function of the injected value of β for all the signals. For the sources at a given distance observed in a particular detector, the 90% credible interval does not vary significantly across the range of injected values of β. For some signals with $\beta < 0.02$, the signal-to-noise ratio is less than 8, and hence we do not perform parameter estimation on them.

For signals sources at a distance of 23 kpc with $\beta < 0.02$ observed in Cosmic Explorer 1, we estimate β with an error of 21%. This increases to 24% for Cosmic Explorer 2. For signal sources at 23 kpc with $\beta > 0.02$, we can estimate β with 6% error for Cosmic Explorer detectors. The error increases as the source distance increases. Fig. 20 shows the α_1 and α_2 posteriors obtained for the signal with $\beta = 0.0299$ at a distance of 23 kpc observed in Cosmic Explorer 1 (blue) and Cosmic Explorer 2 (orange). Since the signal is observed with higher signal-to-noise ratio in Cosmic Explorer 2 than in Cosmic Explorer 1, the posteriors obtained for the former are smaller in area. However, the point with α_1 and α_2 values corresponding to the signal (shown as the red star) is within the 90% credible region of both posteriors. When these posteriors are translated to the posteriors of β, using the map discussed in Sec. 3.3, the difference between the median value of β obtained and the β of the injected signal is higher for Cosmic Explorer 2 than that for Cosmic Explorer 1. Such error is introduced for several signals and leads to lower overall error for Cosmic Explorer 1 than its upgraded counterpart. For Advanced LIGO, β is measured with an error of 9%.
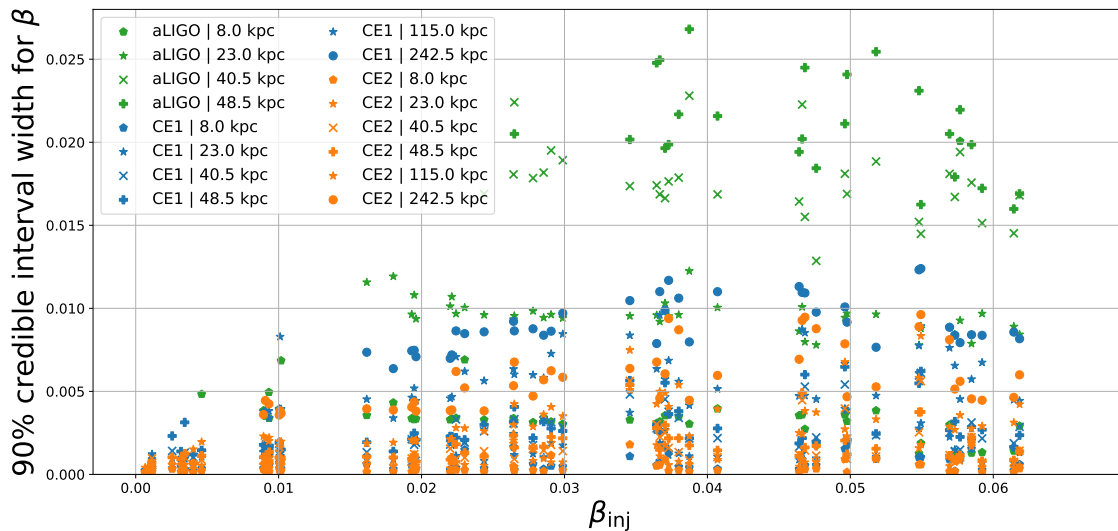
Figure 19: The 90% credible interval width of the posteriors obtained for β as a function of the β of the injected signal waveform. We note that the signals observed in Cosmic Explorer 1 (blue) and Cosmic Explorer 2 (orange) are measured an order of magnitude more precisely than the signals in Advanced LIGO (shown in green). On an average, the 90% credible interval width for signals observed in Cosmic Explorer 1 is 1.5 times that of the signals observed in Cosmic Explorer 2.

For signals with $\beta \geq 0.02$ observed in the third generation detectors, we can measure f_{peak} with an mean error of upto 3%. The average 90% credible intervals obtained for f_{peak} for such signals within the galaxy is 5 Hz. Estimating f_{peak} with such precision restricts the possible equations of state consistent with the f_{peak} values, specially for signals with $0.02 \leq \beta \leq 0.06$. We obtain an average 90% credible intervals for f_{peak} of 7 Hz for signals at the center of Milky way observed in Advanced LIGO noise, with a systematic error of 4%. For sources that are further away, the average 90% credible interval are more that 35 Hz. The systematic error is larger that the range spanned by the mean f_{peak} values of various equations of state listed in Table 4 and we conclude that third-generation gravitational-wave detectors are required to extract nuclear physics from core-collapse supernovae. The method to extract f_{peak} for any waveform with a corresponding $\beta \leq 0.02$ is unreliable, and hence we get large systematic errors and 90% credible intervals for such signals. We include these results for completeness.
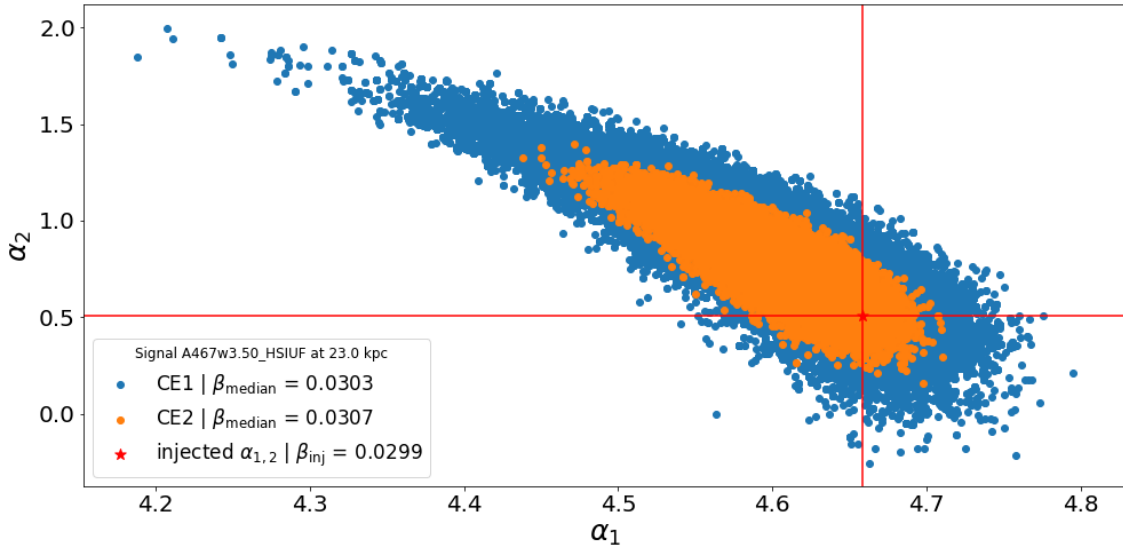
Figure 20: The α_1 and α_2 posteriors obtained for the signal with $\beta = 0.0299$ at 23 kpc observed in Cosmic Explorer 1 (shown in blue) and Cosmic Explorer 2 (shown in orange). The (α_1, α_2) point corresponding to the injected signal (shown as the red star) is within the 90% contour region of both posteriors. The 90% contour region for the posterior of signal observed in Cosmic Explorer 2 is smaller than that of Cosmic Explorer1 because the signal has higher signal-to-noise ratio in the former. However, when these posteriors are transformed into the posteriors of β, the error in median values of β is larger for Cosmic Explorer 2 than Cosmic Explorer 1.

3.6 Conclusion

Practical implementation of Bayesian inference relies on the existence of parameterised gravitational-waveform models that are inexpensive to compute. Such models, with parametrization for the core rotation rate and the postbounce oscillation frequency, do not exist for complete core-collapse supernovae waveforms due to the complexity of the physics involved. In this paper, we address this problem for the first two phases of core-collapse signals, namely the core bounce and the postbounce oscillations. We use principal component analysis to create a parameterised model that extracts the most common features of the bounce signal onto the principal components. We construct a map between the physical parameters and the model parameters (principal components and their coefficients). We use Bayesian inference to measure the coefficients of the first fifteen principal components for a signal observed

in gravitational-wave detectors, and use the inverse of the aforementioned map to obtain posteriors of the physical parameters. In particular, we obtain posterior probability distributions for the ratio of rotational kinetic energy to the potential energy of the core at bounce (β) and the peak frequency of the post bounce oscillations of the protoneutron star (f_{peak}).

β depicts the rotation rate of the inner core of the star at the core bounce. We find the relationship between the model parameters and β by interpolating known values of β from the hyper-volume formed by the model parameters. f_{peak} encodes useful information about the nuclear equation of state, and tells us about the behaviour of hot, dense nuclear matter in the core of the star. We can successfully measure f_{peak} for waveforms with $\beta \geq 0.02$, however the method to extract it fails for waveforms of extremely slowly rotating cores.

For signals with $\beta \geq 0.02$ at a distance of 8 kpc detected in Advanced LIGO, β can be estimated with a 90% credible interval of 0.004 for Advanced LIGO, and 0.0008 for Cosmic Explorer detectors. The width of the 90% credible interval for β increases to 0.002 (0.003) for sources at 23 kpc (48.5 kpc). On an average, the 90% credible interval for β for signals observed in Cosmic Explorer 1 is 1.5 times larger than that for signals observed in Cosmic Explorer 2. We can also estimate f_{peak} to within ~ 6 Hz for signals sources upto the distance of 48.5 kpc with $\beta \geq 0.02$ observed in the third-generation detectors. Using the posteriors on f_{peak}, we can successfully rule out the nuclear equations of state that are inconsistent with the signal. The error in measuring f_{peak} for the signals observed in Advanced LIGO is 4% with an average 90% credible interval width of 6 Hz for sources at the center of the Milky Way. For sources that are further away, the 90% credible interval width increases to more than 20 Hz. We conclude that third-generation detectors are required to constrain the nuclear equation of state from gravitational-wave observations of core-collapse supernovae.

Previous studies have used principal component analysis in Bayesian reconstruction of the signal observed in the detectors [143, 169] or to infer the core-collapse explosion mechanism [138, 139, 140, 141]. Edwards et al [142] used principal component analysis to measure β for signals observed in Advanced LIGO with signal-to-noise ratio 20, and obtained the 90% confidence interval width of 0.06. We demonstrate

a method that uses principal component analysis in Bayesian estimation of physical parameters β and f_{peak}, and to find the dependence of gravitational-waveform morphology on these physical parameters. For a signal comparable to the ones in Edwards *et al.* study, our method yields a confidence interval of 0.02, which is three times smaller than that found by Edwards *et al.*

A more robust map between the model parameters and β can be constructed my populating the model parameter space and using machine learning. We leave the construction of this map and analysis of signals observed in Einstein telescope for future work.

Chapter 4

Measuring the properties of $f-$mode oscillations of a protoneutron star by third generation gravitational-wave detectors

4.1 Introduction

The core of a massive star ($M \geq 8M_\odot$) collapses due to gravity upon achieving the effective Chandrasekhar mass of a massive-star progenitor [134, 37, 40]. The inner part of the core collapses to nuclear densities to form a proto-neutron star. A shockwave is created at the boundary of the protoneutron star and propagates outwards. The shock is initially stopped in its progress outward as a fraction of the kinetic energy of the shock is used to dissociate the heavy nuclei. A fraction of neutrinos produced in the proto-neutron star are trapped behind the shock. This heats up the the shocked region and enhances the turbulent convection, which revives the stalled shock [33]. The joint observation of the photons, neutrinos, and gravitational waves emitted during this process can help reveal the mechanism by which the shock is revived and a neutron star is born.

Core-collapse supernovae are possible sources of gravitational-waves that could

be detected by the proposed third-generation interferometric detectors, such as the Cosmic Explorer [168, 30] and the Einstein Telescope. These observatories will be able to detect a supernova within 100 kpc, which includes the Milky Way galaxy and its satellites [46]. The estimated rate of supernovae for a galaxy the size of Milky Way is 1-3 per century [91, 48, 97].

A number of studies have characterized the gravitational wave signal from the collapse and explosion of the core of a massive star [170, 171, 172, 151, 173, 174, 139, 86, 175, 176]. After decades of improvement in the numerical techniques, we are now much better able to account for the complex hydrodynamics in multi-dimensions, the neutrino interactions, and the hydrodynamical instabilities [177, 136, 178, 179, 39].

This rich and complex physics gives rise to a complex gravitational-wave signal, which in the time domain represents the stochastic nature of matter movements within the star. There is a sharp negative peak in the signal at the time of core bounce, and its amplitude depends on the rotation rate of the core of the progenitor. This is followed by the post-bounce oscillations of the core, that extend for 6-10 ms after the bounce, with an amplitude that depends interestingly on the rotation rate of the core of the progenitor star and its equation of state [51]. The end of post-bounce oscillations mark the onset of "prompt convection" due to the dynamical imposition of a negative entropy gradient as the shock stalls. Starting from $\sim$150 ms after the core bounce, there is a strong, stochastic signal. Moreover, an asymmetrical explosion is accompanied by a growing offset in the mean strain from zero due to "memory"[180, 181, 182].

Even though the signal is highly stochastic in the time domain, the time-frequency spectrogram of the gravitational-wave signal reveals that most of the power lies in a narrow track in the time-frequency plane. Linear perturbation analysis of the proto-neutron star shows that this frequency corresponds to the quadrupolar $f-$mode of the proto-neutron star [175, 176], which start approximately $100 - 400$ ms after the core bounce. These oscillations are excited by the downflows of matter accreted onto the proto-neutron star [172, 175].

Previously, Ref. [183] measured the frequencies associated with the g-mode oscillations of the proto-neutron star using the time-frequency spectrograms of the gravitational-wave strains obtained from simulations. Using the frequency measurement and universal relations, they obtain measurement of the ratio $M_{\mathrm{PNS}}/R_{\mathrm{PNS}}^2$ of

the proto-neutron star, where M_{PNS} is the mass and R_{PNS} is the radius of the proto-neutron star. Ref. [184] develop a phenomenological model of the gravitational-wave signal associated with the dominant mode and use the spectrogram of the strain to measure f-mode frequency evolution and energy. They use Bayesian parameter estimation to measure their model parameters and then obtain frequencies and energies associated with the mode from the posteriors. More recently, Ref. [185] extended the work of Ref. [183] of measuring the f/g mode frequencies of the proto-neutron stars using the strains of 3D and 2D simulations. They use a network of current, and future, detectors to perform a coherent analysis of the detected signal.

Here, we develop a model-independent method to measure the $f-$mode frequencies and the energy emitted in gravitational radiation of the proto-neutron star oscillations by analysing the spectrograms of the gravitational-wave strains obtained from state-of-the art three-dimensional core-collapse supernovae simulations. We develop a novel method of generating time-frequency spectrograms that can be used to reliably measure power in a given track on the spectrogram. We inject the strain obtained through the simulations into several instances of simulated detector noise to measure the frequencies and energies. We vary the distance of the source to test this method for signals with various signal-to-noise ratios. We find that, from simulated observations using the third-generation gravitational-wave detectors, while we can detect the signal out to distances of ≈ 100 kpc, we can measure the frequencies and the energies associated with the $f-$mode oscillations to within 20% error from sources within ≈ 10 kpc distance.

Section 4.2 describes the numerical simulations used in this work, and describes the linear perturbation analysis used to determine the $f-$mode oscillation frequencies. In Section 4.3 we describe our method to construct the short-time Fourier transform and the spectrogram of the gravitational-wave signal obtained from the simulations. In Section 4.4, we describe our main results from the analysis. We summarize our findings in Section 4.5.

4.2 Simulations

In our analysis we used the data obtained from two- and three-dimensional core-collapse supernovae simulations performed with the neutrino-radiation hydrodynamics code FORNAX [186, 187, 188]. The progenitors used in the simulations were calculated by Refs. [189] and [190]. Further details of the simulations can be found in Refs. [175, 136, 176].

We tabulate the models we consider in our works in Tables 8,9,10. We show the mass of the progenitor, the equation of state of the proto-neutron star used in the simulations, and the core-rotation rate in columns 3, 4, and 5 of the table. We also indicate whether the the shock is revived and the star explodes within the time of the simulation. For the three-dimensional simulation models, We use a wide range of progenitors with the ZAMS (Zero-Age Main Sequence) mass ranging from $9M_\odot - 60M_\odot$. We use SFHo equation of state, and all but the $13M_\odot$, $14M_\odot$, and $15M_\odot$ explode within the time of the simulation. For the two-dimensional simulations with core rotation at the time of core bounce, we use a $15M_\odot$ progenitor. We have a total of 14 models with rotation rates ranging from 0.0 rad/sec -6.14 rad/sec. We also include 9 two-dimensional simulations with zero core rotation.

The last three columns show the optimal distances for every simulation, for Advanced LIGO [191], Einstein Telescope [31], and Cosmic Explorer[30]. Optimal distance of a source, for a given detector is defined as the distance at which the signal-to-noise ratio of the optimally-oriented source is equal to eight. It is calculated as,

$$d_{\rm opt} = \frac{1}{\rho_{\rm opt}} \left[2 \int_{f_{\rm low}}^{f_{\rm high}} df \frac{\tilde{h}(f)\tilde{h}^*(f)}{S_n(f)} \right], \tag{4.1}$$

where $\rho_{\rm opt} = 8$ is the signal-to-noise ratio of an optimal detection, $\tilde{h}(f)$ is the strain signal in the Fourier domain, and $S_n(f)$ is the power spectral density of the detector noise. For Advanced LIGO, we use the `aLIGOZeroDetHighPower` [111] power spectral density, with $f_{\rm low} = 10$ Hz. The average of the optimal distances of the waveforms from three-dimensional simulations for Advanced LIGO is 8 kpc. Hence, we can detect a signal coming from the center of the galaxy if it is loud enough. The next generation detectors, Einstein Telescope and Cosmic Explorer, can detect signals coming from the Milky Way galaxy and its satellite galaxies. Their detection range is large enough to cover the entire Milky way but not large enough to reach the nearest galaxy,

Andromeda, which is at 770 kpc. The gravitational-wave signals from core-collapse supernovae observed by the third-generation detectors will have large signal-to-noise ratio.

Label	Progenitor mass ($M_\odot$)	Equation of state	Core rotation rate (rad/sec)	Explosion Status	Optimal Distance (kpc)		
					Advanced LIGO	Einstein Telescope	Cosmic Explorer
s9–3D	9	SFHo	-	Yes	2	25	39
s10–3D	10	SFHo	-	Yes	7	73	116
s11–3D	11	SFHo	-	Yes	6	61	98
s12–3D	12	SFHo	-	Yes	8	79	127
s13–3D	13	SFHo	-	No	7	71	118
s14–3D	14	SFHo	-	No	7	74	121
s15–3D	15	SFHo	-	No	7	72	114
s17–3D	17	SFHo	-	Yes	11	107	171
s18–3D	18	SFHo	-	Yes	11	108	174
s19–3D	19	SFHo	-	Yes	15	141	228
s20–3D	20	SFHo	-	Yes	13	131	214
s25–3D	25	SFHo	-	Yes	13	125	208
s60–3D	60	SFHo	-	Yes	9	93	150

Three-dimensional simulations

Table 8: The Table, along with Tables 9 and 10 summarizes the details of the simulations, including the progenitor mass, equation of state, initial core rotation, and explosion status within the simulated time interval. Based on the gravitational-wave strain obtained from the simulations, we also measure the optimal distance of the strain signal for Advanced LIGO, Einstein Telescope, Cosmic Explorer.

	Label	Progenitor mass ($M_\odot$)	Equation of state	Core rotation rate (rad/sec)	Explosion Status	Optimal Distance (kpc)		
						Advanced LIGO	Einstein Telescope	Cosmic Explorer
Two-dimensional simulations with core rotation	0.0strain	15	SFHo	0.0	No	28	270	427
	0.05strain	15	SFHo	0.05	No	32	324	516
	0.1strain	15	SFHo	0.1	No	32	320	531
	0.2strain	15	SFHo	0.2	No	45	458	735
	0.25strain	15	SFHo	0.25	No	46	466	797
	0.3strain	15	SFHo	0.3	No	34	335	572
	0.4strain	15	SFHo	0.4	No	51	510	863
	0.5strain	15	SFHo	0.5	No	54	534	903
	0.75strain	15	SFHo	0.75	No	59	567	907
	1.0strain	15	SFHo	1.0	No	79	763	1249
	2.0strain	15	SFHo	2.0	No	106	1096	1715
	pi.strain	15	SFHo	3.14	Yes	140	1465	2343
	4.0strain	15	SFHo	4.0	No	145	1539	2511
	5.0strain	15	SFHo	5.0	No	146	1580	2633
	2pi.strain	15	SFHo	6.28	No	123	1312	2316

Table 9: Same as Tables 8 and 10 but for two-dimensional simulations with non-zero progenitor core rotation.

	Label	Progenitor mass ($M_\odot$)	Equation of state	Core rotation rate (rad/sec)	Explosion Status	Optimal Distance (kpc)		
						Advanced LIGO	Einstein Telescope	Cosmic Explorer
Two-dimensional simulations without core rotation	M10–LS220	10	LS220	-	No	15	150	232
	M10–DD2	10	DD2	-	No	17	176	268
	M10–SFHo	10	SFHo	-	Yes	36	361	566
	M13–SFHo	13	SFHo	-	No	30	312	483
	M19–SFHo	19	SFHo	-	Yes	55	534	880
	gw–s11–2D	11	SFHo	-	No	31	307	481
	gw–s19–2D	19	SFHo	-	No	39	401	621
	gw–s25–2D	25	SFHo	-	No	47	446	715
	gw–s60–2D	60	SFHo	-	No	47	460	732

Table 10: Same as Tables 8 and 9 but for two-dimensional simulations without progenitor core rotation.

4.2.1 Linear Perturbation Analysis

In this section, we outline the method of the linear perturbation analysis of the angle-averaged data of the proto-neutron star profile (i.e. integrated over the solid angle Ω). The proto-neutron star is to be modeled with the energy-momentum tensor of a perfect fluid.

$$T_{\mu\nu} = \rho H u^\mu u^\nu + P g_{\mu\nu}, \tag{4.2}$$

where ρ denotes the rest-mass density, P the pressure, u^μ the fluid 4-velocity and $H :=$ $(1+\epsilon+P/\rho)$ the specific enthalpy, ϵ the specific internal energy. Under the assumption of spherical symmetry [1], the space-time metric $g_{\mu\nu}$ in isotropic coordinates, using the $(3+1)$ foliation, can be written as [192, 167, 177, e.g] ,

$$ds^2 = g_{\mu\nu}dx^\mu dx^\nu = -\alpha^2 dt^2 + \psi^4 f_{ij} dx^i dx^j \tag{4.3}$$

where α is the lapse function and the metric for spatial slices is approximated to be conformally related to the flat metric δ_{ij} with a conformal factor ψ^4, set to 1 in all simulations of Tables 8,9,10.

We now perform perturbation analysis on top of this conformally-flat background by linearizing the equations of general relativistic hydrodynamics. In general, the three components of the Lagrangian fluid displacement field, $\boldsymbol{\xi}(\boldsymbol{r},t) \equiv \xi^r \hat{r} + \xi^\theta \hat{\theta} + \xi^\phi \hat{\phi}$ representing the perturbation, can be resolved in terms of three scalar functions by virtue of the Helmholtz decomposition theorem. If one assumes that the radial component of the fluid vorticity equation vanishes at all points of the star, that is, $(\nabla \times \xi)_r = 0$, then one can show that the three components of ξ can now instead be resolved in terms of only two scalar functions. We now decompose these two scalar functions into purely radial functions $(\eta_r(r), \eta_\perp(r))$ supplemented with the spherical harmonics Y_{lm} and mode frequency σ as

$$
\begin{aligned}
\xi^r &= \eta_r Y_{lm} e^{-i\sigma t}, \\
\xi^\theta &= \eta_\perp \frac{1}{r^2} \partial_\theta Y_{lm} e^{-i\sigma t}, \\
\xi^\phi &= \eta_\perp \frac{1}{(r\sin\theta)^2} \partial_\phi Y_{lm} e^{-i\sigma t}.
\end{aligned}
\tag{4.4}
$$

---

[1]The asymmetries are small enough and hence the angle-averaged background can well be approximated as spherically symmetric.

Here, any time dependence of the background state is assumed to be very small compared to the eigen value (i.e. the time derivative of any quantity f, $\partial f / \partial t <<$ f/σ). If σ is real, the system is neutrally stable (i.e. the modes are oscillatory in nature). As the background metric is assumed to be conformally flat, the perturbation of the metric is accomplished by perturbing the lapse function. Decomposing the perturbation to the lapse function in purely radial and spherical harmonics yields

$$\delta \alpha = \delta \hat{\alpha}(r) Y_{lm} e^{-i\sigma t}. \tag{4.5}$$

We define $f_\alpha \equiv \partial_r(\hat{\delta \alpha}/\alpha)$; together with $\hat{\delta \alpha}$ it represents the perturbation in the gravity sector. The timescale associated with neutrino heating and nuclear dissociation is typically $>> 1/\sigma$, hence the perturbations to the fluid properties to be adiabatic in nature, implying,

$$\frac{\partial P}{\partial \rho}|_{\text{adiabatic}} = H c_s^2 = \frac{P}{\rho}\Gamma_1, \tag{4.6}$$

c_s the relativistic sound speed in the fluid, and Γ_1 the adiabatic index. Now the equations of general-relativistic hydrodynamics together with the 00 component of the Einstein equation can be linearized to obtain the following system of equations:

$$\partial_r \eta_r + \left[\frac{2}{r} + \frac{1}{\Gamma_1}\frac{\partial_r P}{P} + 6\frac{\partial_r \psi}{\psi}\right]\eta_r + \frac{\psi^4}{\alpha^2 c_s^2}\left(\sigma^2 - \mathcal{L}^2\right)\eta_\perp - \frac{1}{\alpha c_s^2}\delta \hat{\alpha} = 0, \quad (4.7)$$

$$\partial_r \eta_\perp - \left(1 - \frac{\mathcal{N}^2}{\sigma^2}\right)\eta_r + \left[\partial_r \ln q - \tilde{G}\left(1 + \frac{1}{c_s^2}\right)\right]\eta_\perp - \frac{1}{\alpha \tilde{G}}\frac{\mathcal{N}^2}{\sigma^2}\delta \hat{\alpha} = 0, \quad (4.8)$$

$$\partial_r f_\alpha + 4\pi\left[\partial_r \rho - \frac{\rho}{P\Gamma_1}\partial_r P\right]\eta_r - \frac{4\pi\rho}{P\Gamma_1}q\sigma^2\eta_\perp + \left[\frac{4\pi\rho^2 h}{P\Gamma_1\alpha} - \frac{1}{\alpha}\frac{l(l+1)}{r^2}\right]\delta \hat{\alpha} = 0, \quad (4.9)$$

and

$$\partial_r \delta \hat{\alpha} = f_\alpha \alpha - \tilde{G}\delta \hat{\alpha}. \tag{4.10}$$

In Equations 4.7-4.10, we have collected the combination $\rho h \alpha^{-2}\psi^4$ as q, $\tilde{G}$ is the radial component of gravitational acceleration $\tilde{G} := -\partial_r \ln \alpha$, $\mathcal{N}$ is the relativistic Brunt-Väisälä frequency,

$$\mathcal{N}^2 = \frac{\alpha \delta_r \alpha}{\psi^4}\left(\frac{1}{\Gamma_1}\frac{\partial_r P}{P} - \frac{\partial_r e}{\rho H}\right) \tag{4.11}$$

and $\mathcal{L}$ is the relativistic Lamb shift,

$$\mathcal{L}^2 = \frac{\alpha^2}{\psi^4} c_s^2 \frac{l(l+1)}{r^2} \tag{4.12}$$

The system of equations 4.7-4.10 can be solved by incorporating appropriate boundary conditions: at the outer boundary, set at the radial coordinate where the density $\rho = 10^{10} g/cm^{-3}$ we consider the Lagrangian pressure to vanish and at the inner boundary (i.e. $r = 0$) use the regularity condition of [193]. Mathematically, this reads, at the outer boundary,

$$q\sigma^2 \eta_\perp - \frac{\rho H}{\alpha} \hat{\delta\alpha} + \partial_r P \eta_r = 0 \tag{4.13}$$

and at the inner boundary,

$$\eta_r = \frac{l}{r} \eta_\perp \propto r^{l-1}$$

$$\eta_r|_{r=0} = \eta_\perp|_{r=0} = 0$$

By discretizing the derivatives by means of trapezoidal rules, we can start integrating the set of equations 4.7-4.10 by inverting the 4×4 coefficient matrix at every step to solve for $(\eta_r, \eta_\perp, f_\alpha, \hat{\delta\alpha})$ and then using the bisection method to uniquely determine the solutions by satisfying the outer boundary condition Eq. 4.13. The eigenvalue corresponding to the unique solution thus obtained gives the frequency of oscillation as $\sigma/2\pi$. The lowest frequency oscillation mode is the fundamental oscillation mode (f-mode), with zero radial nodes. We find the f-mode starts few hundred ms after the core bounce for the simulations in Tables 8,9,10 which confirms similar findings in [175]. The f mode thus obtained is then laid on the spectrogram and is found to contribute significantly to the strength of the GW signal after $\sim$ 400 ms. As noted in [175], the higher-order g- or p-modes are not found to be excited in these simulations.

4.3 Spectrogram Analysis

In this section, we describe the construction of the spectrogram of the gravitational-wave strain signal. We use the spectrogram to measure the properties of the fundamental quadrupolar $f-$mode oscillations of the protoneutron star. In particular, we are interested in measuring the frequency of the oscillations and the energy emitted

in the gravitational-wave radiation. The analysis described here is for the fiducial case when the detector noise is not present. In the later sections we will discuss the effect of detector noise in the extraction of the features from the spectrogram and compare it with the output from the analysis described here.

Following [194, 195, 196, 86], the gravitational-wave strain $\mathbf{h_{ij}^{TT}}$ for a for a source at a distance D can be written as

$$\mathbf{h_{ij}^{TT}} = \frac{2G}{c^4 D} \frac{dq_{ij}}{dt}, \tag{4.14}$$

where q_{ij} is the time derivative of the mass quadrupole tensor $\mathcal{Q}_{ij} = \int d^3x \rho(x_i x_j - \frac{1}{3} r^2 \delta_{ij})$. The strain amplitudes of the two polarizations, h_+ and $h_\times$, can be obtained in the slow-motion limit from the linear combinations of the second time derivatives of the components of the transverse traceless mass quadrupole tensor $\mathcal{Q}_{ij}$. The polarization strains as observed along the line of sight (θ, ϕ) are given by

$$h_+ = \frac{G}{c^4 D} \left(\frac{dq_{\theta\theta}}{dt} - \frac{dq_{\phi\phi}}{dt} \right), \tag{4.15}$$

$$h_\times = \frac{2G}{c^4 D} \left(\frac{dq_{\theta\phi}}{dt} \right). \tag{4.16}$$

Here, the time derivatives of the mass quadrupole in spherical coordinates, in terms of those in Cartesian coordinates, are given by

$$q_{\theta\theta} = (q_{xx} \cos^2 \phi + q_{yy} \sin^2 \phi + 2q_{xy} \sin \phi \cos \phi) \cos^2 \theta$$
$$+ q_{zz} \sin^2 \theta - 2(q_{xz} \cos \phi + q_{yz} \sin \phi) \sin \theta \cos \theta, \tag{4.17}$$

$$q_{\phi\phi} = q_{xx} \sin^2 \phi + q_{yy} \cos^2 \phi - q_{xy} \sin \phi \cos \phi, \tag{4.18}$$

$$q_{\theta\theta} = (q_{xx} - q_{yy}) \cos \theta \sin \phi \cos \phi +$$
$$q_{xy} \cos \theta (\cos^2 \phi - \sin^2 \phi)$$
$$+ q_{xz} \sin \theta \sin \phi - q_{yz} \sin \theta \cos \phi. \tag{4.19}$$

The total energy emitted in gravitational waves is given by [196]

$$E_{GW} = \frac{c^3}{5G} \int_0^t \sum_{ij} \left[\frac{d^3 \mathcal{Q}_{ij}}{dt^3} \right]^2 dt, \tag{4.20}$$

which, in terms of gravitational-wave strain is given by

$$
\begin{aligned}
E_{GW} &= \frac{c^3 D^2}{16\pi G} \int_0^t dt \int_{4\pi} d\Omega \left[\left(\frac{dh_+}{dt}\right)^2 + \left(\frac{dh_\times}{dt}\right)^2 \right] \\
&\approx \frac{c^3 D^2}{4G} \int_0^t dt \left[\left(\frac{dh_+}{dt}\right)^2 + \left(\frac{dh_\times}{dt}\right)^2 \right],
\end{aligned}
\tag{4.21}
$$

where the second approximation holds true if the strains are assumed to be nearly independent of line of observation and the integral over the solid angle gives a factor of 4π. The variation in the amplitudes of the strain for different points of observation are $10-15\%$ [197]. For two-dimensional simulations without progenitor core rotation, the approximation does not hold, and we use equations 3-6 in Morozova *et al* [175] to compute the energy from gravitational-wave strain h_+.

Ground-based interferometers will detect a linear combination of the strain polarizations,

$$
s(t) = s_{\text{eff}}(t) + n(t),
\tag{4.22}
$$

where n is the noise in the detector, and effective strain from the astrophysical source is given by,

$$
s_{\text{eff}} = F_+ h_+ + F_\times h_\times.
\tag{4.23}
$$

Here, F_+ and $F_\times$ are the antenna pattern functions of an interferometric detector, and they depend on the sky location (Right ascension, Declination) of the source at a given time, and its polarization angle with respect to the detector arms. The energy estimation from an observation is then given by

$$
E_{GW;\text{eff}} \approx \frac{c^3 D^2}{4G} \int_0^t dt \left(\frac{ds_{\text{eff}}}{dt}\right)^2,
\tag{4.24}
$$

which would be ≈ 0.5 times the energy calculated using both the polarizations individually (i.e. from Equation 4.21).

To compute the energy spectra of the gravitational wave signal we use the spectrogram of the signal

$$
\begin{aligned}
\frac{dE_{GW}^\star}{df} &= \frac{c^3 D^2}{4G} (2\pi f)^2 \left[(\tilde{h}_+)^2 + (\tilde{h}_\times)^2 \right] \\
&\approx \frac{c^3 D^2}{2G} (2\pi f)^2 \left[\tilde{s}_{\text{eff}} \right]^2,
\end{aligned}
\tag{4.25}
$$

where $\tilde{h}$ is the short-time Fourier transform, defined as

$$\tilde{h}(f) = \int_{-\infty}^{\infty} h(t)H(t - \tau_l)e^{-2\pi i f t}dt, \qquad (4.26)$$

and $H(t - \tau_l)$ is the Hann window with offset time τ_l, indexed by l. A window function is applied to each segment to ensure that we don't get Gibb's junk when we take the Fourier transform of the segment. Equation 4.25 gives the energy per unit Hertz for a time-frequency block centered at time τ_l and frequency f. Thus, a spectrogram is the transformation of the short-time Fourier transform to represent the power content in a time-frequency block.

In practice, gravitational-wave strain h is a discrete function of time, obtained either from simulations, or via observations made by a gravitational-wave detector. In order to take the Fourier transform of the time-domain strain data, $h_j \equiv h_+(t_j)$, it must be evenly sampled at time intervals of $\Delta t = t_{j+1} - t_j$ seconds, $\forall j$. The sampling rate, or sampling frequency is given by $f_s = 1/\Delta t$. The data from the simulations is unevenly sampled since the size of each time step in the simulations is governed by the micro- and macro-physics at the time.

We re-sample the data at sampling rates ranging from $16,384$ Hz to $2,097,152$ Hz in powers of two and interpolate using one of the two interpolation schemes: linear interpolation and cubic spline interpolation. We then compute the energy using discretized versions of equations 4.15, 4.16 and 4.21, where now $h(t) \equiv h(t_j)$. We compute the third order time derivative of the the quadruple moment from the second order derivative using the central difference method. Fig. 21 shows the energies on the left ordinate for the model s19-3D computed via the two interpolation methods at various sampling rates. We see that the energy values converge with increasing sampling rate. The dashed curves show the difference between the energy values obtained between two consecutive sampling rates (shown on the right ordinate). This plot gives us a range of energy estimations for data sampled at different frequencies. We choose to use the Cubic spline interpolation and a sampling rate of $16,384$ Hz (or equivalently, sampling interval of $\Delta t = 6.1035 \times 10^{-5}$ seconds) since its is computationally less expensive and is a more realistic choice with regards to the sampling rate used by current and proposed gravitational-wave detectors.

In the next subsection we describe the construction of the short-time Fourier

transform of the discretely-sampled signal, and measurement of the frequencies associated with the $f-$mode from the time-frequency representation. For this purpose, we use 50% overlap of Hann-windowed time-segments, since this configuration does not affect the amplitude of the signal. In the subsection that follows, we discuss the construction of spectrogram that can be used to measure the energy associated with the $f-$mode oscillations. For this, we use 66.65% overlap between two consecutive Hann-windowed segments since this configuration provides equal weights across all the point in the signal for power calculation.

4.3.1 $f-$mode frequency measurement

In order to compute the short-time Fourier transform of the data, we need to divide the data into segments of equal length, say of $T_W = N_W \Delta t$ seconds, and multiply each of these segments with a window function before we take its Fourier transform. There are a variety of windows available for this purpose [198]. In this study, we use the Hann window. We need to ensure that each data point of the waveform is equally weighted when we consider the sums of the windowed waveform segments. This presents a problem at the ends of the waveform, since Hann window starts from (or tapers to) zero. The solution is to first taper both ends of the waveform to zero, and then zero-pad the entire waveform on both ends by multiples of N_W points. Zero-padding the waveform does not change the total power content in the signal since we are only adding zeros to the ends of the data. We use the window size of $T_W = 40$ ms. For tapering, we use the 1024 data points at both ends of the waveform and apply a half cosine window. We zero-pad both ends of the tapered waveform by $N_W = 655$ points. For constructing the short-time Fourier transform of the signal, we use 50% overlap between two consecutive time segments that get multiplied by the Hann window.

The top panel of Fig. 22 shows the gravitational-wave strain data of the plus polarization as a function of time after core bounce for the simulation s19-3D in blue. This three-dimensional simulation uses a progenitor with ZAMS mass of $19 M_\odot$. The equation of state used in the simulation is SFHo. The top panel shows evenly-sampled data in blue, and the data with both ends tapered for construction of the short-time Fourier transform is shown in orange. The bottom panel shows the short-time Fourier transform of the strain. The horizontal axis shows the time after bounce,

the vertical axis shows the frequency. The color bar shows the modulus of the Fourier amplitude. We see the prompt convection signal after ~ 50 ms after the core bounce. The prompt convection phase is followed by the ~ 50 ms long quiescent phase. After this, the dominant part of the signal starts with frequency growing from ~ 500 Hz to ~ 1000 Hz 0.6 sec after core bounce. This signal is caused by matter accreting on the proto-neutron star and exciting its modes, including the $f-$mode. The $f-$mode frequencies obtained by the linear perturbation analysis are shown as red crosses in the bottom panel.

We measure the frequency evolution of the dominant track in the short time Fourier transform. To measure the frequencies, we use the following procedure. We start by analyzing the spectrogram data after t_0 seconds. The vertical orange line in Fig. 22 shows the time $t_0 = 200$ ms after the core bounce. From the linear perturbation analysis we know that the $f-$mode starts around this time. We define a plausible range of the $f-$mode frequencies shown by the two orange quadratic curves in Fig. 23. The quadratic parameters for the lower frequency bound are $a = -700, b = 1800, c = 10$ and for the upper frequency bound are $a = -600, b = 2500, c = 400$ used in the formula $f(t) = at^2 + bt + c$. For each time segment after t_0, we find the highest value of the energy spectrum within the frequency range constrained by the two orange curves. We model the frequency evolution of the $f-$mode as the quadratic function, and use a robust least-squares fit of the maxima in the STFT for each time slice using the `soft-l1` loss function to get the parameters $\{a, b, c\}$ of the quadratic function.

4.3.2 Energy measurement

We are interested in computing the power in each of the time-frequency blocks in the spectrogram associated with the $f-$mode frequencies. To ensure that we can do this correctly, we first compare the power in the entire signal evaluated using the Equation 4.21 (using the time-domain representation of the signal) and via the spectrogram (adding up power in all the time-frequency blocks). However, when we construct the spectrogram, multiplying a data segment with a window function alters the amplitude, and hence, the power, of the signal. To mitigate this problem, we make two consecutive segments of the data overlap by a fixed amount of $T_{\mathcal{O}}$ seconds. We also want to ensure that the relative weighing is the same for all the data points

across different segments. The relative weighing of the data for power calculation is obtained by summing the square of the window values at each data point. That is, for the point j, the weighing will be given by $\sum_l H^2(j\Delta t - \tau_l)$. We want this quantity to be constant across the the entire signal. For the first half of the first window, and the second half of the last window, the relative weighing does not matter since we are zero-padding the ends of the waveform.

Trethewey (2002) [199] show that one cannot simultaneously obtain equal weighing of all data points, and compute the correct power. For Hann windows, one obtains the correct value of average power of the entire signal if consecutive segments overlap by 62.5%. However, in this case, there is variation in the relative weighing of the data points, resulting in amplification of power in certain data segments, whereas reduction in others. This would mean large errors in power estimates within individual time segments, specially if the data are stochastic in nature, like the gravitational-wave strain from a supernova. If two consecutive segments overlap by 66.65%, all the points are equally weighed, but the power calculation is amplified by a factor of 1.125, across all segments. However, we can compute the power with 66.65% overlap, and scale it down by the relevant factor to obtain the correct value of power.

Assuming 66.65% overlap between segments, the time-difference between the start of two consecutive segments is $T_H = T_W - T_{\mathcal{O}}$ seconds, such that $100 \times T_{\mathcal{O}}/T_W = 66.65$. We multiply each segment by a Hann window $H(t_j - \tau_l)$, where τ_l is the time offset of the center of the segment from the start of the signal. The length of the Hann window is equal to the length of the segment. We take the discrete Fourier transform of each segment of the windowed data $h_j H(t_j - \tau_l)$ using `scipy.fftpack.fft`, given by

$$\tilde{y}_{k,\tau_l} = \sum_{j=0}^{N_W - 1} h_j H(t_j - \tau_l) e^{2\pi i j k / N_W}. \tag{4.27}$$

The discrete form of Equations 4.25, 4.26 is given by

$$\frac{\Delta E_{GW}}{\Delta f}(f_k, \tau_j) \sim \frac{D^2 c^3}{2G}(2\pi f_k)^2 \Delta t^2 |\tilde{y}_{k,\tau_j}|^2, \tag{4.28}$$

where we have a factor of 2 instead of 4 in the denominator to account for the power in the negative frequencies. To normalize the effect of the window function, we use

the window normalizatoin factor from Heinzel et al (2002) [198],

$$\frac{S_2}{N_W} = \frac{1}{N_W} \sum_{j=0}^{N_w-1} H^2(t_j).$$

(4.29)

Using this normalization, Equation 4.28 becomes

$$\frac{\Delta E_{GW}}{\Delta f}(f_k, \tau_j) = \frac{D^2 c^3}{2G}(2\pi f_k)^2 \Delta t^2 |\tilde{y}_{k,\tau_j}|^2 \left[\frac{N_W}{S_2}\right].$$

(4.30)

The total Energy can then be written as

$$\begin{aligned}
E_{GW} &= \sum_k \sum_l \frac{\Delta E_{GW}}{\Delta f}(f_k, \tau_j)\Delta f \left[\frac{T_H}{T_W}\right] \\
&= \sum_k \sum_l \frac{D^2 c^3}{2G}(2\pi f_k)^2 \Delta t^2 |\tilde{y}_{k,\tau_j}|^2 \Delta f \left[\frac{N_W T_H}{S_2 T_W}\right],
\end{aligned}$$

(4.31)

where the quantity $\left[\frac{T_H}{T_W}\right]$ is introduced to account for the fact that two consecutive segments overlap by $T_{\mathcal{O}}$ seconds. The factor $\left[\frac{T_H}{T_W}\right]$ corrects for this double-counting and represents the correct fraction of the energy in the time segment. in the final equation, the factor $\left[\frac{N_W T_H}{S_2 T_W}\right]$ for 66.65% overlap is equal to 1.125, the same factor from Trethewey (2000) [199].

Now, we can verify if the energy values obtained from the spectrogram (Equation 4.31) agree with those obtained using the Equation 4.21. We find that the energy values agree within the error range due to interpolation.

Once we have verified that the energies obtained from the time-frequency data agree with those obtained by the time domain data, we can compute the energy associated with a given time-frequency track. In particular, we can compute the energy associated with the $f-$mode oscillation of the protoneutron star.

The top panel in Fig. 23 shows the frequency evolution of the $f-$mode obtained from the spectrogram. For each time-segment, we assume the width of the $f-$mode track to be $6\Delta f$ ($3\Delta f$ above the spectral peak associated with the $f-$mode frequencies, and $3\Delta f$ below it). This width is represented as the two white curves encompassing the peak frequency curve shown in red. We can add up the energy values for all the time-frequency blocks within the width obtained. Doing this for all the time segments after $t = t_0$ will give us the time evolution of the energy associated with the $f-$mode.

The bottom panel of Fig. 23 shows the cumulative energy as a function of time for the simulation s19-3D. The blue curve shows the cumulative energies obtained from the time-domain data (Equation 4.21) and the orange curve shows the cumulative energies obtained by adding up energy values for all time-frequency blocks in the spectrogram. We can see that both match very well. The green curve shows the cumulative energy of the $f-$mode as a function of time measured by adding the energy values in time-frequency blocks only corresponding to the $f-$mode (i.e. within the two white curves in top panel of Fig. 23). The energy obtained in the $f-$mode is $\approx 20 - 40\%$ of the energy from the entire signal. We also compute the energy values obtained from the effective strain observed by a detector and its spectrogram (i.e. from Equation 4.24). We show these energies (multiplied by a factor of 2) in purple and red color in the bottom panel.

We test this method for toy signals of the form $h(t) = A(t)\sin(2\pi f t)$, as well as the solutions for the differential equations for driven simple-harmonic oscillator (for details on this model see Ref. [200]). We find that we get $\approx 20\%$ error in the measurement of the power from the spectrogram as compared to the measurement directly from the time domain signal. The error is higher when stochasticity of the amplitude increases.

4.4 Results

In this section, we describe the results of using the above method for measuring the properties of the $f-$mode for gravitational-wave strains from various simulations.

The left panel of Fig. 24 shows the frequency evolution of the $f-$mode measured from short-time Fourier transform for the three-dimensional simulations. Since the simulations are for a short duration, we start the measurement of the $f-$mode frequencies (and consequently, the energy) from 200 ms after the core bounce. However, this procedure makes the frequency measurement noisy for the time interval $200 - 400$ ms after the core bounce since $f-$mode oscillations are not the most energetic contributors to the gravitational-wave signal. The peak of the Fourier transform may not lie on the frequencies associated with the $f-$mode. One can see that the frequencies at 200 ms lie in the range between 500 Hz - 600 Hz. 600 ms after the core bounce, the frequencies can increase up to 1100 Hz - 1250 Hz. Again, there is no monotonous

dependence of the frequencies with the progenitor mass.

The right panel of Fig. 24 shows the energy in the $f-$mode track obtained from the spectrogram of the gravitational-wave signal, divided by the time when the $f-$mode oscillations are active (i.e. 200 ms to end of simulations). Typically, the higher mass progenitors produce a stronger gravitational-wave signal, and hence the power in the $f-$mode oscillation track is higher for higher progenitor mass. If we look at Fig. 2 of Ref [136], which describes the time evolution of the shock radius of the same progenitors that we use in this study, we find that delayed explosion time also correlates with increased energy emission in the gravitational wave signal. For example, the power measured in $f-$mode for simulations with progenitor masses $10, 19$, and $25M_\odot$ is higher in comparison to other simulations, and the shock expansion associated with the explosion is also delayed. For the progenitors with no explosion during the simulation time, we measure low power in the $f-$mode from the gravitational-wave signal.

Fig. 25 shows the frequency evolution on the left panel and the power in $f-$mode oscillations from the gravitational-wave signal as a function of the core rotation rate on the right panel for simulations with non-zero core rotation. We find that both the frequency evolution and the power of the $f-$mode oscillations depend on the core rotation rate. Mild core rotation (0 - 0.75 rad/sec) increases the quadrupole moment and hence the power in gravitational-wave radiation. Increasing the core rotation rate increases the centrifugal support on the accreting matter that excites the proto-neutron star oscillations, resulting in reduced power in the oscillations. The frequencies are also affected and we can see two distinct groups of the frequency tracks. For the core rotation rates of $0-0.5$ rad/sec, where the centrifugal forces are not affecting the $f-$mode oscillations, we see we see similar time dependence for the frequencies as for the simulations with no core rotation — they rise from $\approx 850-900$ Hz at 400 ms after the core bounce to ≈ 1700 Hz at 1 second after the core bounce. As the core rotation rate increases, the frequencies decrease, as is seen in the simulations with 0.75 rad/sec and 1.0 rad/sec core rotation rates. Further, for the higher rotation rates (greater than 1.0 rad/sec), the centrifugal forces are large and the frequencies decrease - starting from $\approx 600-800$ Hz at 400 ms after the core bounce to ≈ 1200 Hz at 1 second after the core bounce.

The left panel of Fig. 26 shows the interpolated $f-$mode frequency evolution

measured from the short-time Fourier transforms of the simulations listed in the figure. These are two-dimensional simulations with progenitors having zero core rotation rate at the core bounce. We assume that the $f-$mode starts at ~ 400 ms after the core bounce. There is no monotonic trend with respect to the mass of the progenitor star for the frequency evolution of the $f-$mode oscillations. There is also no monotonic dependence on the equation of state used in the simulation. The stiffest equation of state, DD2, used for the simulation `M10-DD2` produces the smallest frequencies (for times ~ 600 ms after the core bounce). Whereas, the softest equation of state, SFHo, used for simulation `M10-SFHo`, produces frequencies lower than a relatively stiffer equation of state LS220. This has been already discussed in Morozova *et al.* [175], where the authors obtained the frequency evolution from linear perturbation analysis of the proto-neutron star. Here we verify the frequency evolution by measuring the frequencies from the short-time Fourier transform. The right panel of Figure 26 shows the power in the $f-$mode track obtained from the spectrogram of the gravitational-wave signal. Again we see that the higher mass progenitors typically have higher power in the $f-$mode oscillation track. The results of energy measurement for all the waveforms are summarized in Tables 11, 12.

We also repeat the analysis on the spectrogram of signals embedded in simulated detector noise. We assume the source distances to range from 1 kpc to 60 kpc. For each distance, we inject the signal in 10000 instances of detector noise. To generate the simulated noise instances, we use the designed power spectral density for Advanced LIGO and the proposed third generation detectors, Cosmic Explorer and Einstein Telescope.

We assume that the time of core bounce will be measured by the neutrino detectors such as ICECUBE[201], Super-Kamiokande [164], and DUNE [165] to within 4 ms [167, 166, 38]. We measure the $f-$mode frequencies 200 ms after the time of core bounce. We also assume that the distance to the progenitor is known *a priori*, so that when we measure the energy in the $f-$mode via the spectrogram, we can scale it (by the square of the distance) to obtain the energy in gravitational-waves associated with the $f-$mode.

For closer sources, the signal is strong and the noise does not affect the $f-$mode

Label	$E_{GW}(10^{-8}M_\odot c^2)$			
	Time Domain	Spectrogram	Fractional Error	$f-$mode energy
s9-3D	0.0014	0.0015	7 %	0.0002
s10-3D	0.073	0.084	15 %	0.016
s11-3D	0.03	0.03	6 %	0.005
s12-3D	0.05	0.05	1 %	0.012
s13-3D	0.012	0.011	9 %	0.002
s14-3D	0.028	0.031	10 %	0.003
s15-3D	0.026	0.029	8 %	0.006
s17-3D	0.12	0.13	14 %	0.03
s18-3D	0.13	0.15	10 %	0.03
s19-3D	0.33	0.38	16 %	0.081
s20-3D	0.18	0.21	16 %	0.27
s25-3D	0.13	0.16	21 %	0.07
s60-3D	0.024	0.027	13 %	0.008

Table 11: In this table we show the energy in the gravitational-wave signal computed from the time-domain representation of the signal (equation 4.21), and from the spectrogram (equation 4.25) for three-dimensional simulations. We show the error in measurement of the energy from the spectrogram of the signal. In the last column, we show the energy measured from the spectrogram in the track associated with the $f-$mode oscillations.

Label	$E_{GW}(10^{-8}M_\odot c^2)$			
	Time Domain	Spectrogram	Fractional Error	$f-$mode energy
0.0strain	1.2	1.5	22 %	0.81
0.05strain	0.92	1.08	18 %	0.41
0.1strain	0.97	1.15	19 %	0.49
0.2strain	1.43	1.63	14 %	0.82
0.25strain	1.09	1.34	22 %	0.71
0.3strain	1.47	1.77	20 %	1.09
0.4strain	2.28	2.92	28 %	1.60
0.5strain	3.75	4.38	17 %	2.38
0.75strain	5.63	6.47	15 %	2.82
1.0strain	7.9	8.7	9.4 %	2.54
2.0strain	5.7	6.3	10 %	0.44
pi.strain	7.44	8.13	9.3 %	0.01
4.0strain	5.07	4.07	20 %	5e-4
5.0strain	2.41	2.56	6 %	5e-5
2pistrain	0.96	3.3	242 %	9e-8
M10-LS220	0.21	0.24	13 %	0.07
M10-DD2	0.16	0.17	11 %	0.04
M10-SFHo	1.57	1.86	19 %	0.43
M13-SFHo	0.93	1.09	17 %	0.47
M19-SFHo	5.27	6.80	29 %	2.12
gw-s11-2D	1.54	1.89	22 %	0.65
gw-s19-2D	1.47	1.74	18 %	0.69
gw-s25-2D	4.52	5.46	20 %	1.44
gw-s60-2D	4.14	5.48	32 %	2.49

Table 12: Same as Table 11 but for two-dimensional simulations.

frequency measurement. As the source distance increases, the $f-$mode peaks are picked more randomly. This is because the gravitational-wave strain amplitude from the signal is dominated by the detector noise. Consequently, the least-square fit is also affected.

In Figs. 27,28,29, we show the results of our analysis for the $f-$mode frequency and energy measurement when the signal is embedded in detector noise. For each case, we generate a short-time Fourier transform and measure the $f-$mode frequencies. We then interpolate the measured frequencies, and compare them with those for the case when the signal was not embedded in simulated detector noise. We do this by computing the root-mean-squared error in the frequencies, given by

$$\sigma_f = \sqrt{\frac{1}{N_f} \sum_{1}^{N_f} \Delta_f^2}. \tag{4.32}$$

Here, $\Delta_f^2 = (f_{\text{with noise}} - f_{\text{noiseless}})^2$ and N_f is the number of time columns of the $f-$mode. After measuring the $f-$mode frequencies, we use them to measure the energy in the corresponding track on the spectrogram. Since this track now has the gravitational-wave signal from a core-collapse as well as the detector noise, the measurement will yield the energy in the sum of the two. This way, we can place an upper bound on the energy in gravitational-wave radiation associated with the $f-$mode.

In Figs. 27,28,29, on the left panels, we show error in frequency measurement (σ_f) on the vertical axis and distance to the source on the horizontal axis. The blue curve shows the median of the inner product obtained from 10000 injections into simulated Cosmic Explorer noise, whereas the green curve shows the same for the Einstein Telescope. The fill represents the 90th quantile measurements of σ_f. We see that as distance increases, σ_f also increases. we can measure the $f-$mode frequencies to within 10% error for sources within the Milky Way galaxy.

The right panel shows the relative error in measurement of the energy in the $f-$mode from the spectrogram based on the frequencies measured from the short-time Fourier transform,

$$\sigma_E = \frac{E_{f-\text{mode}|\text{noiseless}} - E_{f-\text{mode}|\text{with noise}}}{E_{f-\text{mode}|\text{noiseless}}}. \tag{4.33}$$

We find that we overestimate the energy by up to $\approx 20\%$ for higher mass exploding

models with source distances within the Milky Way galaxy.

In Fig. 30 we show the time evolution of the ratio $\frac{f_{\text{f-mode}}}{\sqrt{G\rho_c}}$ for the three-dimensional simulations, where ρ_c is the central density of the protoneutron star. We find that the ratio linearly increases with time, and obtain the fit $y = 0.23t + 0.06$ using linear regression, where t is the time after bounce. The fit is shown in red in Fig. 30. Using this fit, and the frequency evolution from the spectrogram of the strain measured in a detector, we can measure $\rho_c(t)$. In Fig. 31 the central density $\rho_c(t)$ of the 19 $M_\odot$ star obtained from simulation is shown in red. We also measure ρ_c for the 10000 injections of the signal associated with the model $s19 - 3D$ in Cosmic Explorer, assuming the source distance to be 10 kpc. Given the linear fit for $\frac{f_{\text{f-mode}}}{\sqrt{G\rho_c}}$ and quadratic fits for $f(t)$, $\rho_c(t)$ is a $\sim t^2$ function of time after bounce. We obtain ρ_c values for various times and for various injection instances. The two-dimensional histogram for ρ_c is shown in grey-scale, with the colormap normalized to the logarithm of counts in each $\rho_c - t$ bin. We can see from the plot that we can measure the central density of the core of the star using the frequency evolution measured from the spectrogram.

4.5   Conclusion

Here, we have developed a model-independent method to measure the frequencies and energies associated with the quadrupolar oscillations of a proto-neutron star. We use gravitational-wave signals from two- and three-dimensional core-collapse simulations.

We construct the short-time Fourier transform of these signals to extract the $f-$mode frequencies. We then construct a spectrogram of the signal in a way that provides equal weights in power to all the data points of the signal.

We first test the energy measurement from the spectrogram of the signal by comparing it to the energy computed using the time-domain data. We find that the total energy measured using the spectrogram is within 20% of the energy measured using the time domain data. We then use the frequency evolution of the $f-$mode measured via the short-time Fourier transform to extract the energy from the time-frequency blocks associated with the $f-$mode oscillations using the spectrogram. We find that the $f-$mode energies can be as high as 40% of the total energy emitted in gravitational radiation during a core-collapse.

We find that the energy associated with the $f-$mode oscillations typically increases with the progenitor mass. The energy also depends on the delayed explosion times and the success of explosion. Simulations having higher shock stall times before the onset of explosion emit more gravitational-wave radiation since the oscillations are excited for a longer time. Additionally, the energy of the $f-$mode also increases monotonically with the rotation rate of the core, up to a certain value of core rotation rate. Centrifugal forces dominate for faster core rotations, and cease the activation of the oscillations of the proto-neutron star.

To understand how the detector noise will affect this analysis, we inject the gravitational-wave signals into simulated Cosmic Explorer and Einstein telescope noise and then extract the $f-$mode frequencies and measure the energies. We vary the distance to the source, but limit it to within the Milky Way galaxy. We find that for waveforms from three-dimensional simulations, we can measure the $f-$mode frequencies for sources up to 20 kpc within an RMS error of 5 Hz, and the $f-$mode energies within 20% fractional error, when the gravitational-wave signal is assumed to be detected by a third-generation observatory. For waveforms from two-dimensional simulations with core rotation, we can measure the frequencies for sources up to 20 kpc to within 2 Hz RMS error and energies to within 10% fractional error.

Measurement of the frequencies and energies of the $f-$mode oscillations can provide us more information about the mechanism of the supernova explosion. We can also infer the central density of the proto-neutron star and the turbulence energy within the system.
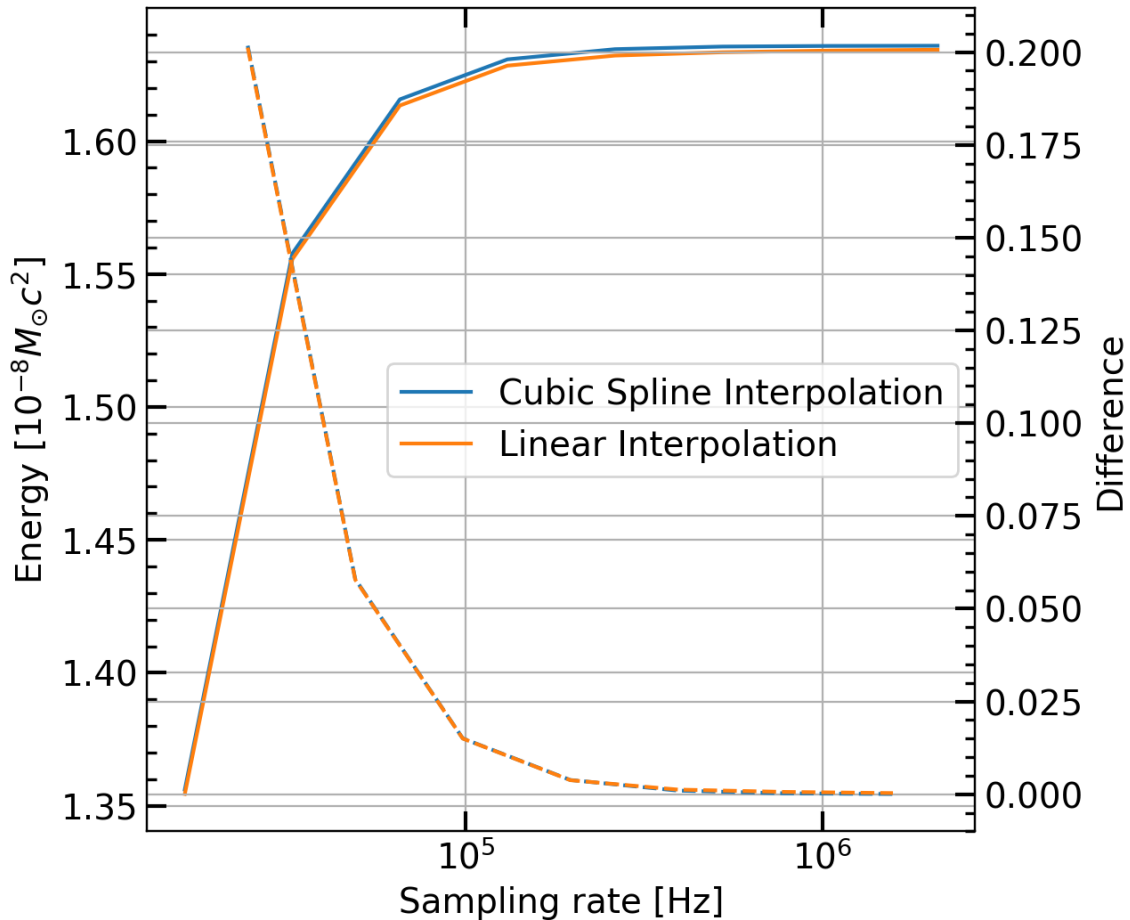
Figure 21: The figure shows the energy (in $10^{-8}M_\odot c^2$) obtained for the simulation s19-3D as a function of the sampling rate used to resample the data from the simulations. The solid blue curve represent the case when Cubic interpolation is used whereas the orange curve shows the case when Linear interpolation is used. The corresponding dashed curves show the difference between energy values obtained for a particular sampling frequency and the one lower. We can see that the values converge as the sampling frequency is increased.
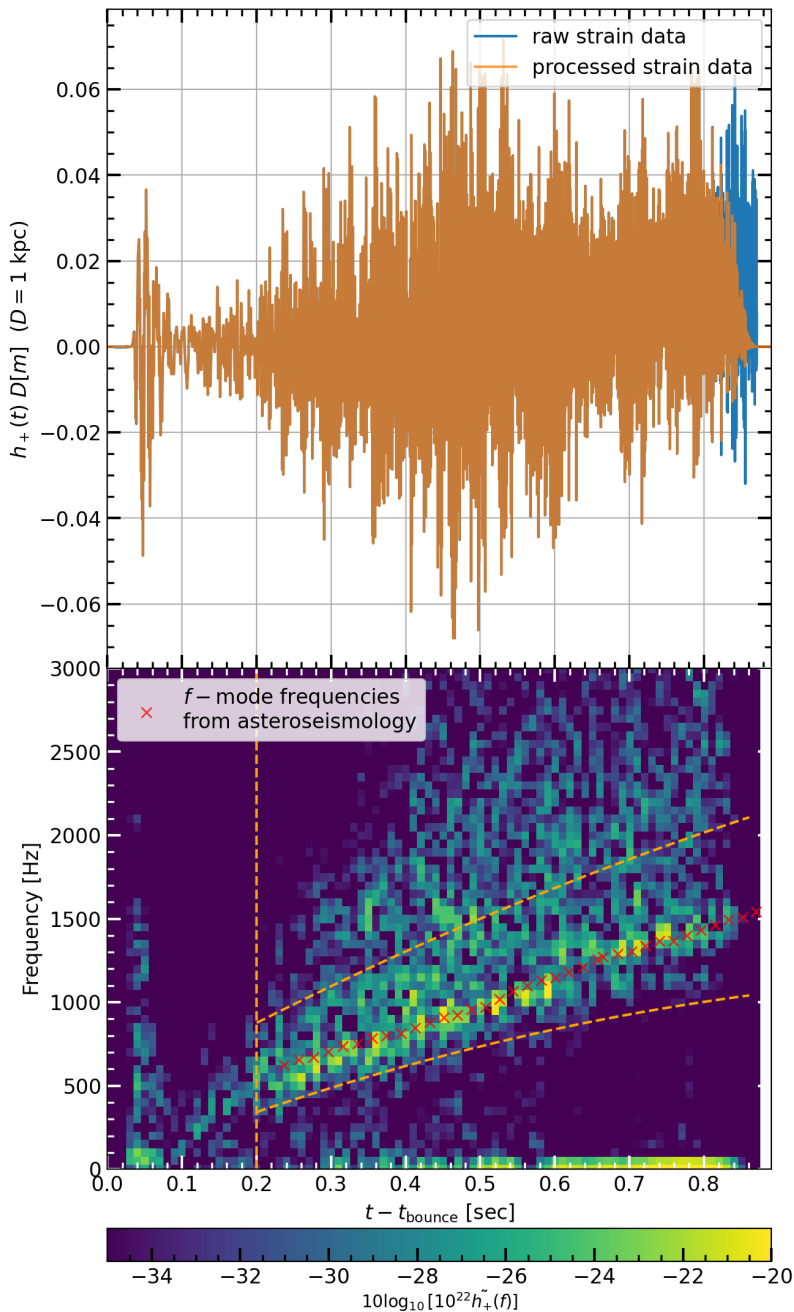
Figure 22: The figure shows the strain (top) and its spectrogram (bottom) of the 3D simulation `s19-3D`. The strain data has been uniformly sampled at 16,384 Hz. The ends have been tapered to zero by applying half cosine windows to the first and last 1024 points of the data. Then, the data are zero-padded by 0.04 seconds on either end. The spectrogram of this signal is shown on the bottom panel. The $f-$mode frequencies, obtained from linear perturbation analysis, start at 200ms and go from 500 Hz to 1000 Hz at 0.6 seconds after the core bounce, and are shown as red crosses in the bottom panel. The vertical orange line shows the time $t_0 = 200$ ms after the core bounce. The two orange parabolic curves define the frequency range within which the algorithm looks for the peak in the spectra.
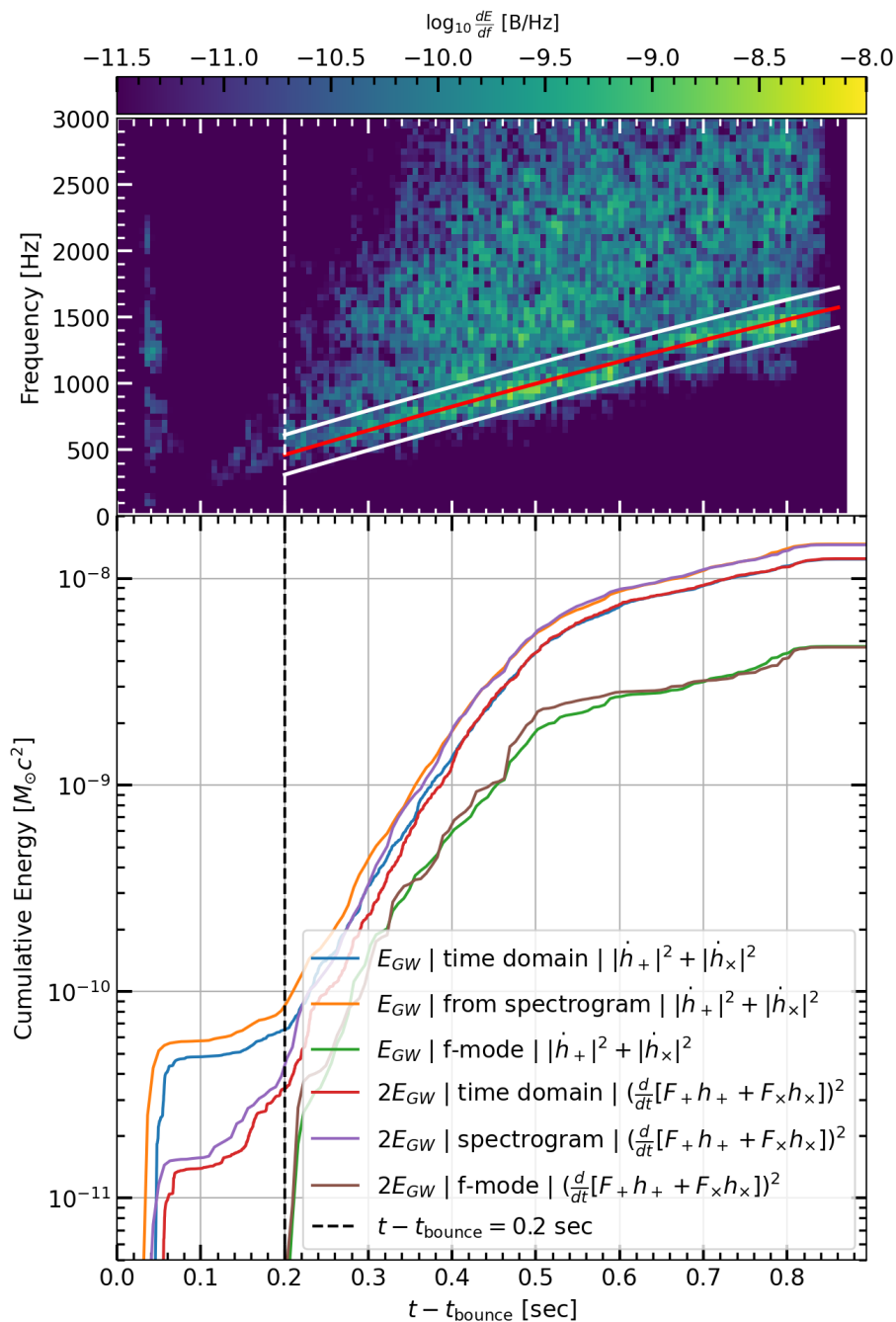
Figure 23: The top panel in the figure shows the spectrogram of the 3D simulation s19-3D. The red curve shows the quadratic fit to the fundamental f−mode frequencies measured by picking the frequencies corresponding to the peak in spectra and the two white curves represent the width of the track. The energy of the mode is measured by summing the energy of the time-frequency blocks within the white curves. The blue, orange, and green curves in the bottom panel show the cumulative energy measured from the time domain representation of the signal, its spectrogram, and for the f−mode from the spectrogram, respectively, and summed for the individual polarizations h_+ and $h_\times$. The red, purple, and brown curves show two times the energies for the same for the effective strain as observed in a interferometer.
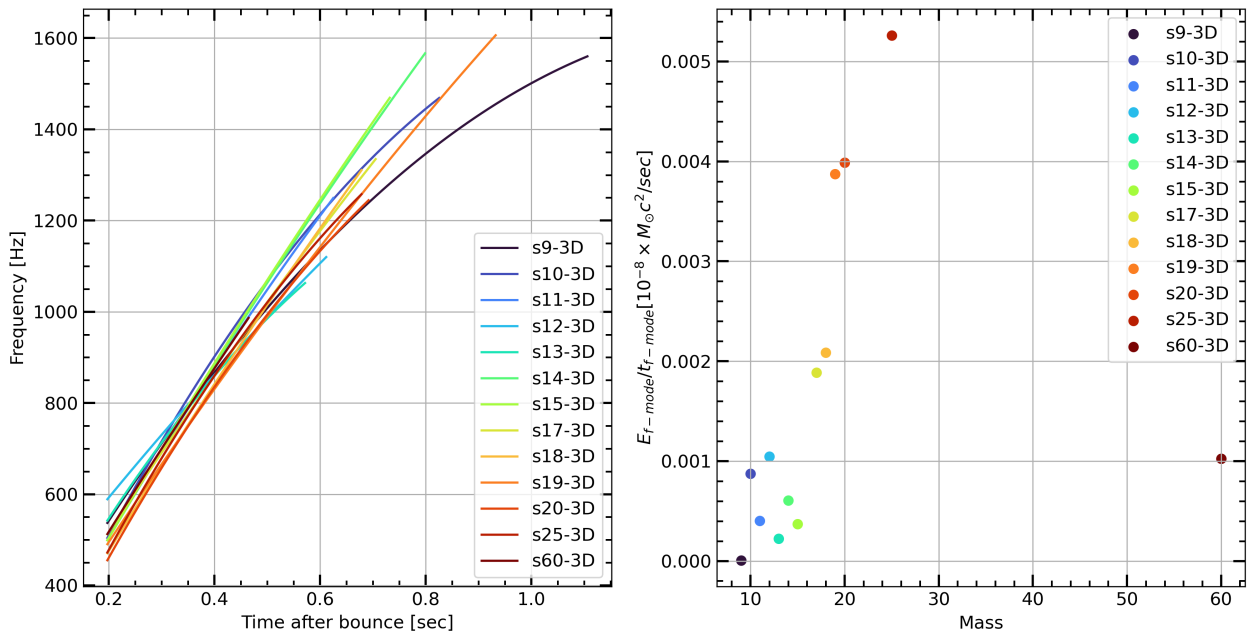
Figure 24: The figure shows the frequency evolution (left) and power (right) measured for the $f-$mode oscillations from the gravitational-wave strains of the three-dimensional simulations. The frequency increases with time, owing to the shrinking of the proto-neutron star. We find that the power in the gravitational-waves associated with the $f-$mode oscillations generally increases as the progenitor mass increases.
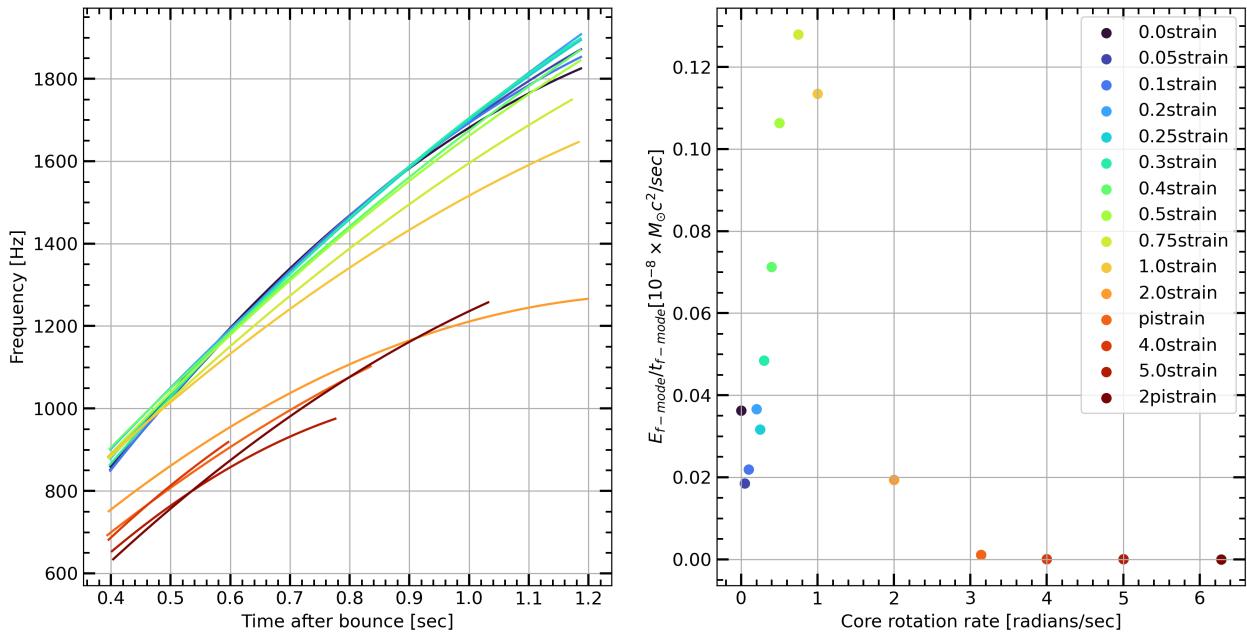
Figure 25: The figure shows the frequency evolution (left) and power (right) measured for the $f-$mode oscillations from the gravitational-wave strains of the two-dimensional simulations with core rotation. The frequency increases with time, owing to the shrinking of the proto-neutron star. We find that the power in the gravitational-waves associated with the $f-$mode oscillations increases monotonically as the progenitor core rotation rate increases, up till $\Omega = 0.75$ rad/sec, and then decreases as centrifugal forces dominate.
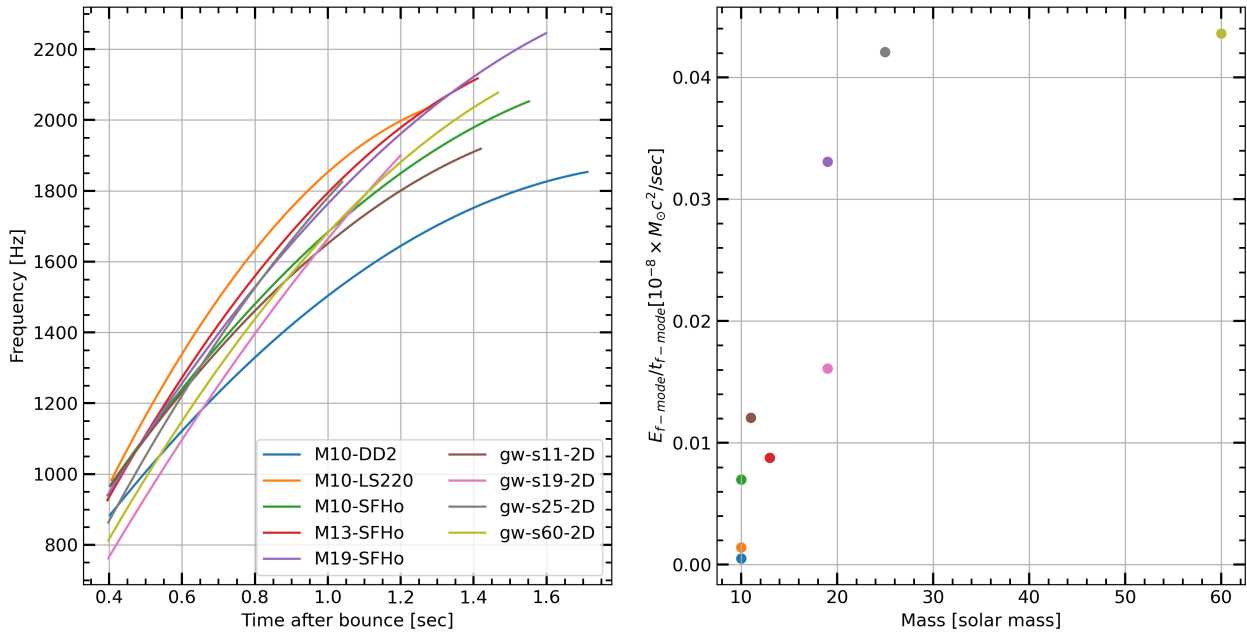
Figure 26: The figure shows the frequency evolution (left) and power (right) measured for the $f-$mode oscillations from the gravitational-wave strains of the two-dimensional simulations without core rotation. The frequency increases with time, owing to the shrinking of the proto-neutron star. We find that the power in the gravitational-waves associated with the $f-$mode oscillations generally increases as the progenitor mass increases.
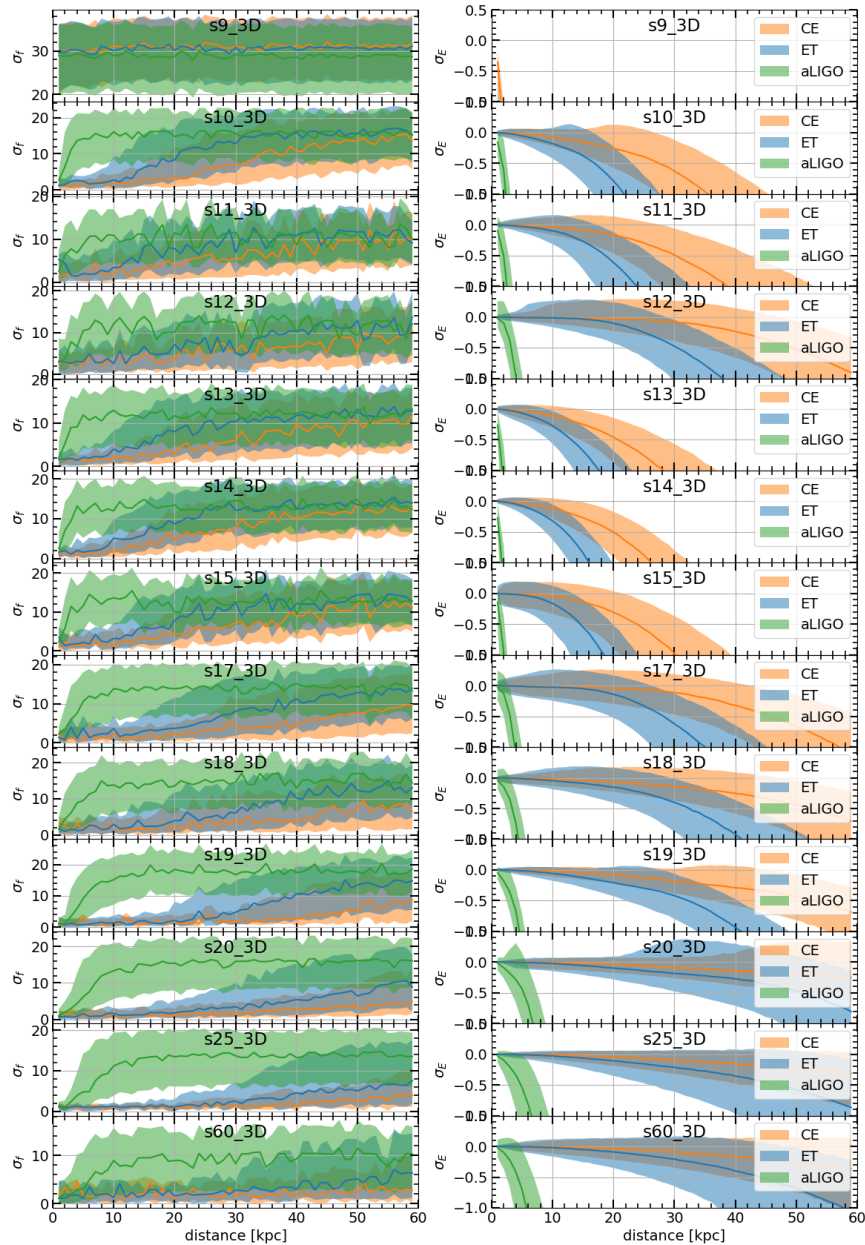
Figure 27: The left panels of the figure show the root-mean-squared error in measurement of frequency evolution of f-mode (σ_f) for waveforms from three-dimensional simulations. The right panel shows the error in measurement of energy in the $f-$mode oscillations (σ_E). The orange line shows the median obtained from measurement in 10000 noise instances of Cosmic Explorer noise, with the fill representing the 90th quantile. The blue curve represents the results for Einstein Telescope, and the green curve for Advanced LIGO.
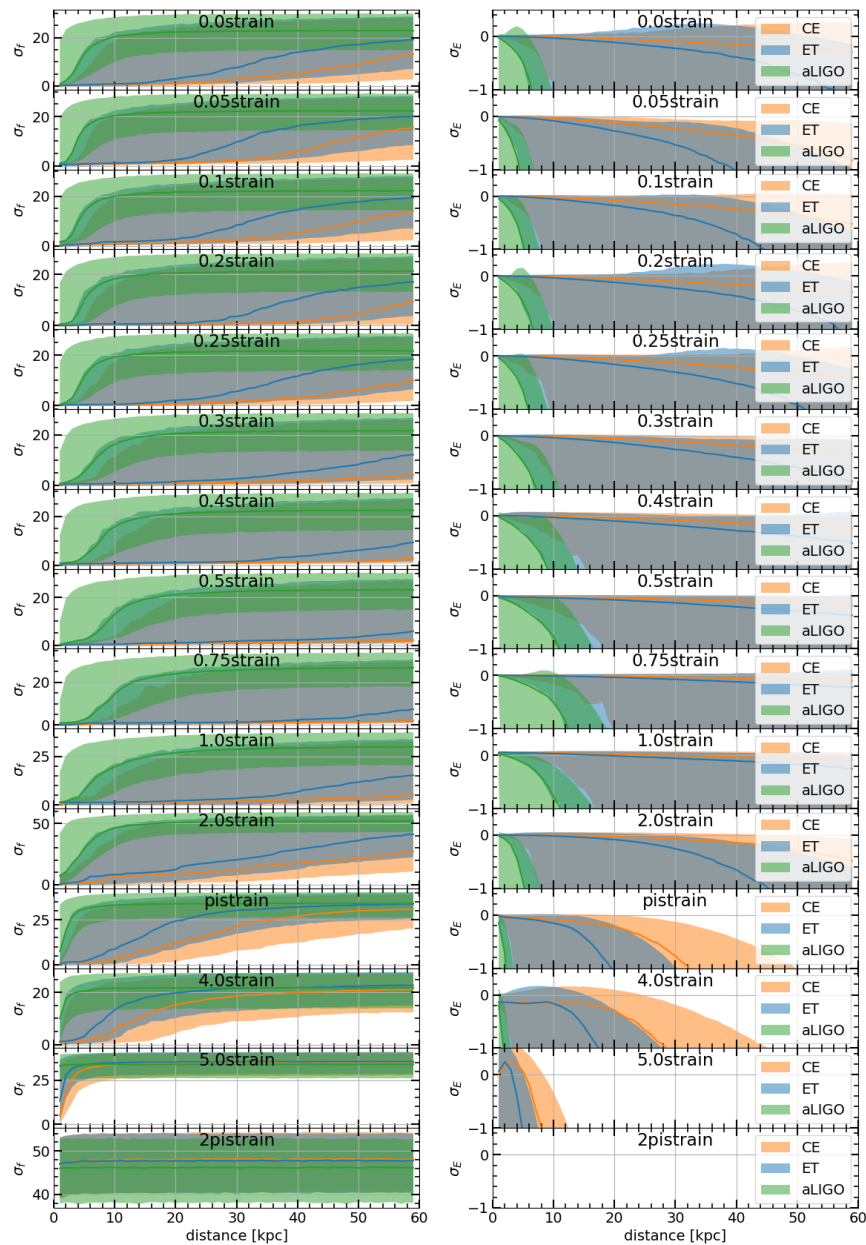
Figure 28: The left panels of the figure show the root-mean-squared error in measurement of frequency evolution of f-mode (σ_f) for waveforms from two-dimensional simulations with core rotation. The right panel shows the error in measurement of energy in the $f-$mode oscillations (σ_E). The orange line shows the median obtained from measurement in 10000 noise instances of Cosmic Explorer noise, with the fill representing the 90th quantile. The blue curve represents the results for Einstein Telescope, and the green curve for Advanced LIGO.
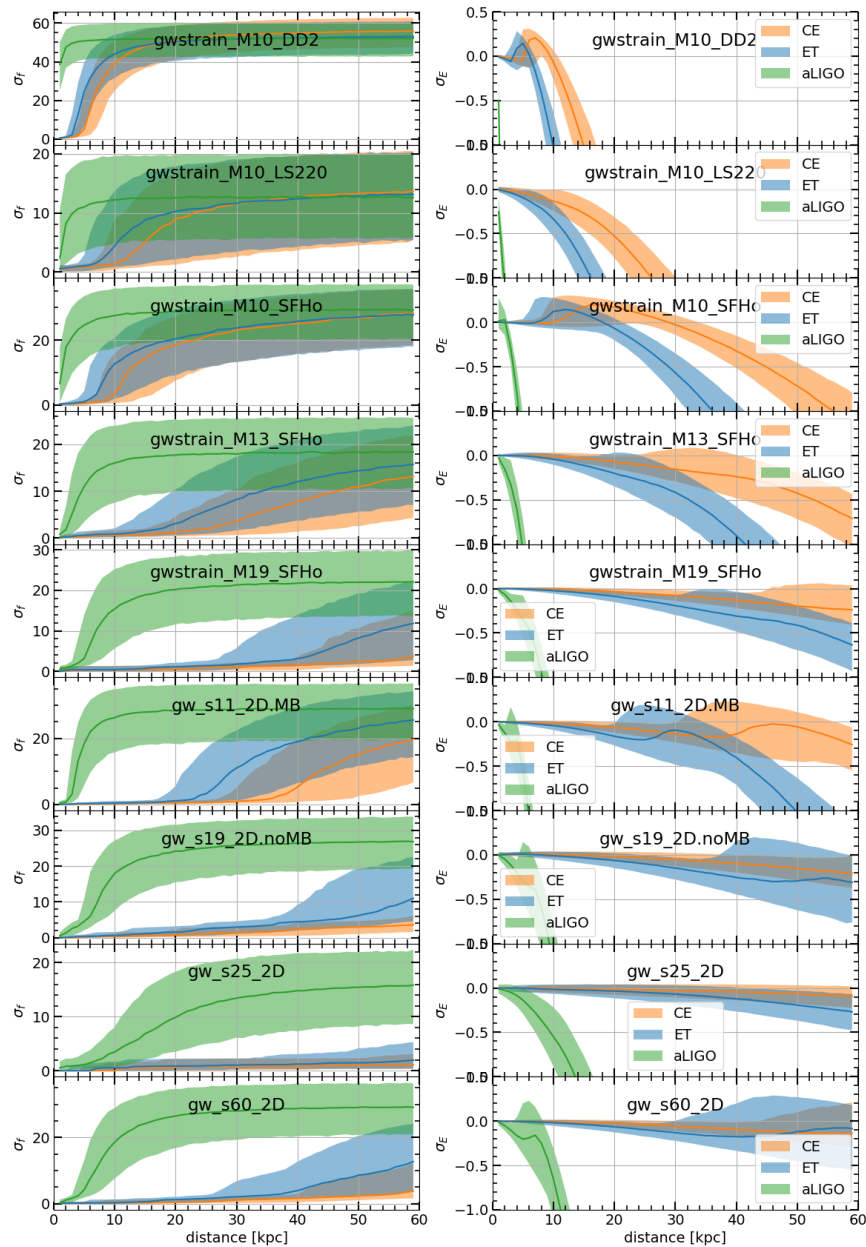
Figure 29: The left panels of the figure show the root-mean-squared error in measurement of frequency evolution of f-mode (σ_f) for waveforms from two-dimensional simulations with zero core rotation. The right panel shows the error in measurement of energy in the $f-$mode oscillations (σ_E). The orange line shows the median obtained from measurement in 10000 noise instances of Cosmic Explorer noise, with the fill representing the 90th quantile. The blue curve represents the results for Einstein Telescope, and green curve for Advanced LIGO.
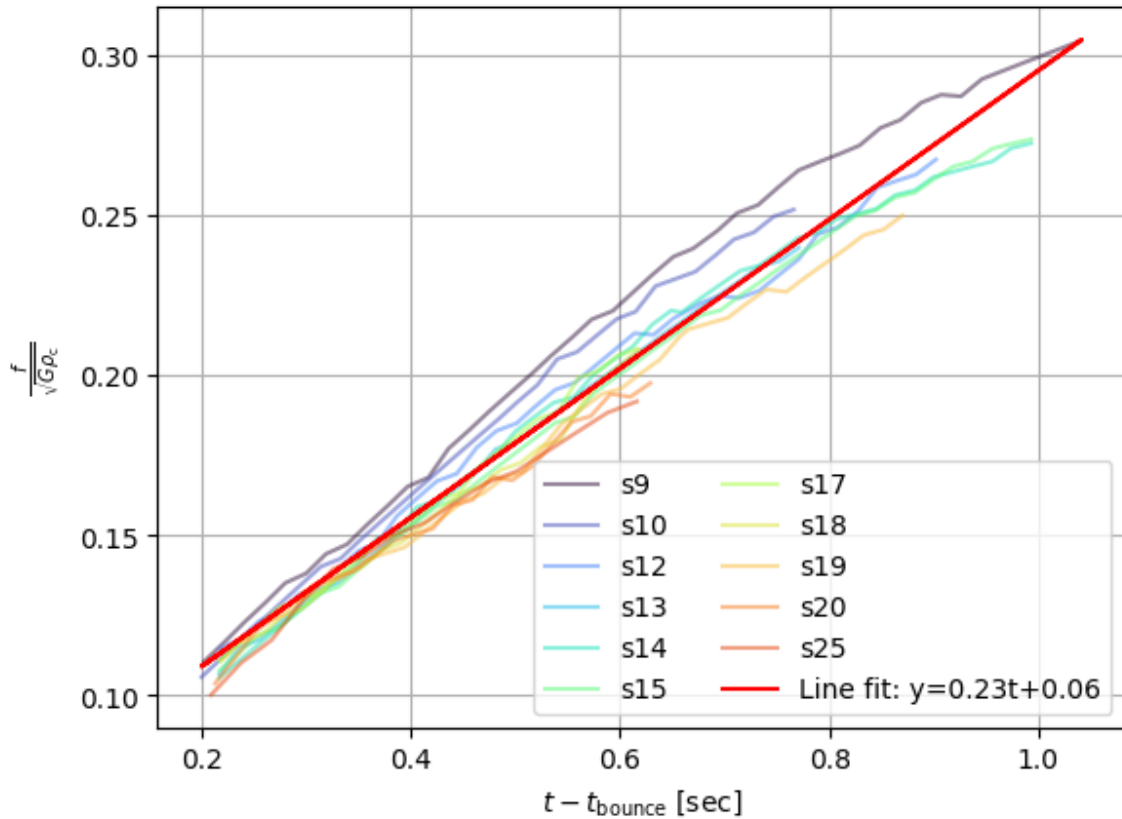
Figure 30: $\frac{f_{\text{f-mode}}}{\sqrt{G\rho_c}}$ as a function of time for the three-dimensional simulations, where ρ_c is the central density of the protoneutron star. The frequencies are obtained from linear perturbation analysis whereas the ρ_c values are obtained from the simulation data. We obtain a linear fit $\frac{f_{\text{f-mode}}}{\sqrt{G\rho_c}} = 0.23t + 0.06$ (shown in red) using the data for all the simulations.
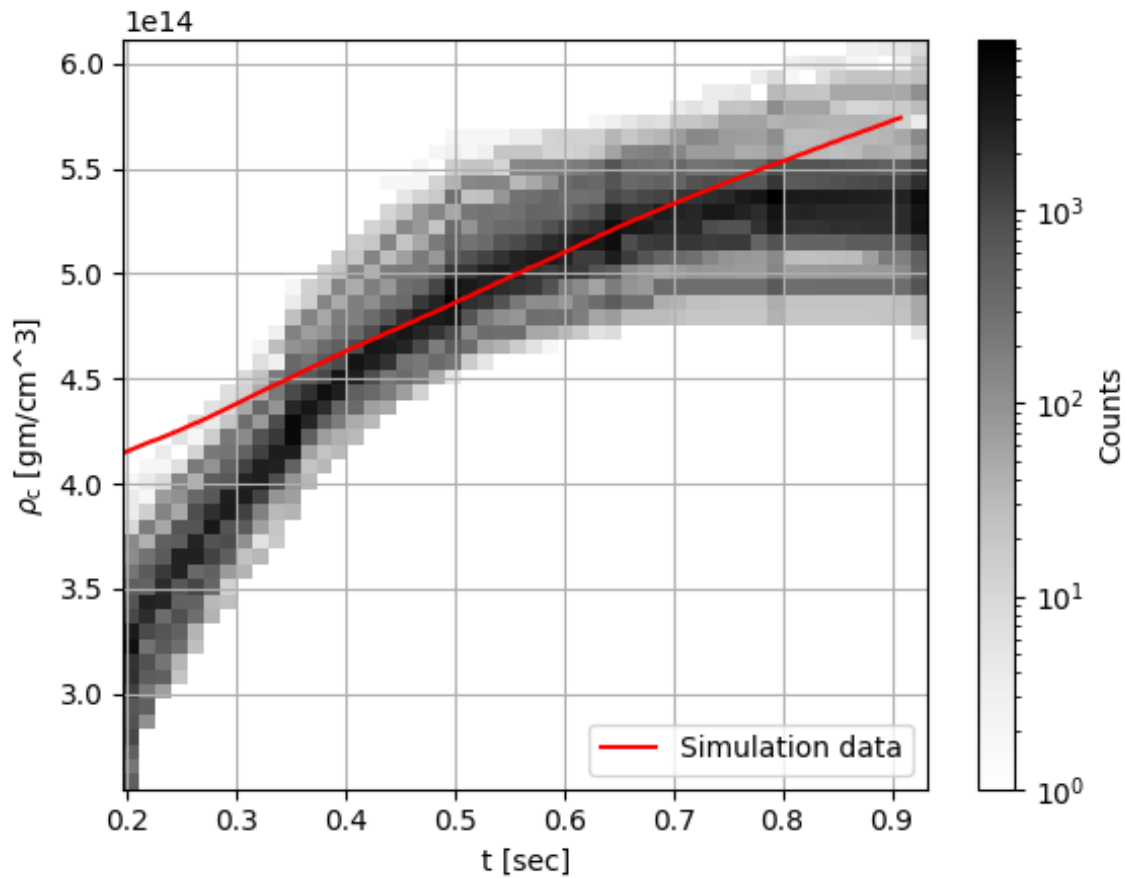
Figure 31: We plot the time evolution of ρ_c for the 19 $M_\odot$ model in red, as obtained from the three-dimensional simulation. We obtain ρ_c for each injection instance when the source is assumed to be at 10 kpc and the signal is detected in Cosmic Explorer. We plot the two-dimensional histogram for the $\rho_{\text{inj}}(t_b)$ where inj is the injection instance and t_b is the time after bounce. The counts for such histogram is shown on the colorbar.

Chapter 5

Reproducing the Results for NICER Observation of PSR J0030+0451

5.1 Introduction

Reproducibility of research—the ability to arrive at a consistent result given the same raw data and original analysis method—is a critical element of scientific discovery. Reproducibility provides the necessary level of trust in the published results and enables researchers to build upon that work. Since more scientific studies are using computation as a tool, reproducibility challenges arise from the computational point of view—- especially the availability of data, software, the needed execution environment, and tools, as well as documentation used in the original analysis.

NICER is a payload onboard the International Space Station and the X-ray Timing Instrument (XTI) is dedicated to observing X-rays from galactic pulsars [202]. Based on NASA's open science and open data policy, the data observed by NICER is released to the public to advance scientific research. One of NICER's aims is to measure the masses and radii of neutron stars. These measurements constrain the neutron-star equation of state, the relation between the pressure and density of the neutron star. Measuring this equation of state requires a computationally-intensive analysis of the NICER data. To fully understand and leverage the results of the equation of state analyses, the astrophysics community needs to be able to reproduce and modify the

original results so that they can: (i) check the robustness of the original result; (ii) build new analyses using the original result, or (iii) extend the original analysis to address new and different questions.

To measure the equation of state using PSR J0030+0451, Riley *et al.* developed the analysis software *X-PSI* [1] (X-Ray Pulse Simulation and Inference) [203]. *X-PSI* includes a Bayesian analysis framework to measure the pulsar's mass and equatorial radius (hence infer the equation of state) using the observed NICER data. We explore whether the analysis of the pulsar PSR J0030+0451 by Riley *et al.* [61] can be reproduced and modified to test the robustness of the result.

Miller *et al.* [204] has the same NICER observations of PSR J0030+0451 to produce an independent analysis using different software, models, and methods to measure the mass and radius of the pulsar. They arrived at measurements of mass and radius of PSR J0030+0451 that were slightly different from, but consistent with, the results of Riley *et al.* This is an example of *replicability* of research: using the same data but different methods to arrive at a consistent result. The conclusion can be drawn that the results are replicable; an analysis of the data leads to a consistent mass and radius result for the pulsar. However, it does not verify that an external entity could use the existing software stack created by Riley *et al.* to achieve the same result, nor does it demonstrate that another group could modify or extend this analysis.

Unlike our previous work on reproducing the detection of GW150914 by LIGO [205], none of the authors of this reproducibility effort were involved in the original analysis. This work is entirely based on the papers, data, software, and documentation provided to the public by the authors of the original study by Riley *et al.* First, we reproduce the results in Figure 19 of Riley *et al.*, which shows the measurement of the mass and the radius of the target pulsar obtained from the analysis. We note the lessons learned and challenges we faced during the reproducibility process, as was done in our previous works where we reproduced the images of the M87 black hole published by the EHT collaboration [206, 207] and reproduced the detection of GW150914 [205]. We discuss the challenges encountered while acquiring the input data, installing and using the software (including setting up the required dependencies and environment), writing configuration files, job submission scripts, and post-processing the job output.

---

[1]https://github.com/xpsi-group/xpsi.git

Ultimately, we were successfully able to reproduce the measurements done in the original analysis.

Going beyond our previous work, after reproducing the original analysis, we demonstrate that Riley *et al.* provides sufficient information to allow a third party to modify the analysis in the new work. We use this functionality to test the robustness of the methods to the prior probability distributions chosen for the Bayesian analysis. Specifically, we expand the previous space on the pulsar radius from 16 km to 25 km and change the sampler configuration for the Bayesian analysis. We find that changing the upper limit of the prior does not change the posterior distribution statistically significantly, demonstrating the result's robustness to the choice of radius prior. We increase the number of sampler points used to sample the posterior probability space from 1000 to 4000 and find that the posterior probability distribution does not change, demonstrating the robustness of the analysis. As part of our work, we repackage *X-PSI* and its software dependencies into a Docker container. This aids in the portability of the data and the software and streamlines the reproduction of the original analysis. The container is fully documented and contains the scripts for the entire workflow used in our reanalysis, and is available at Docker Hub[2].

This article is organized as follows. First, we describe the original analysis and provide background information on measuring the mass and radius of neutron stars from X-ray data. Then, we describe our effort to reproduce the analysis and note the computational challenges. Finally, we summarize the lessons we learned when reproducing the Riley *et al.* analysis and provide guidelines for improvement of the reproducibility of such computationally intensive analyses.

5.2   Analysis Of PSR J0030+0451

Figure 32 shows a schematic overview of the analysis by Riley *et al.* including the observation of the X-rays by NICER, modeling of the X-ray emission from the pulsar surface, and estimation of the mass and radius of the pulsar using the observational data and the models. The parts of analysis performed by Riley *et al.* using *X-PSI* are shown as green boxes.

The mass and radius of the neutron star are imprinted on the X-rays emitted

---

[2]https://hub.docker.com/r/chaitanyaafle/nicer

by hot spots on the neutron star's surface through the relativistic effect of their propagation through the spacetime curvature induced by the star. The X-ray pulse profile detected by a distant observer encodes the neutron star's compactness, the ratio of the star's mass to its radius. NICER measures X-ray counts as a function of time for a target pulsar, as illustrated in a box (1) of Figure 32. Since the photon count profile of the signal is identical for each rotation of the pulsar, the signal can be phase-folded into a single pulse profile, which gives photon count as a function of the phase of the rotation of the pulsar, as shown in Figure 32 on the top right. Creating a phase-folded data set is a pre-processing step performed by the NICER instrument team and creates a derived data set used by subsequent analyses. This data set, released using Zenodo, is the starting point for the Riley *et al.* analyses.

To measure the mass and radius of the star, a model H is created that describes the X-ray emission from the hotspots and uses relativistic ray-tracing of the emitted radiation to predict the pulse profile observed by a distant observer. The parameters of this model are represented by $\vec{\theta}$ and include the mass and radius of the neutron star, the parameters describing the geometry of the hotspots, the distance to the pulsar, the inclination angle of the axis of rotation to the line of view. In box (2) of Figure 32, we show the geometry of the hotspots assumed for two models that we use for reproducing the results from the original analysis.

For a given model H, Bayes' theorem is used to infer the posterior probability distribution of the model parameters given a realization of the observed data (box (3) in Figure 32) according to

$$p(\vec{\vartheta}|\vec{d}(t), H) = \frac{p(\vec{d}(t)|\vec{\vartheta}, H)p(\vec{\vartheta}|H)}{p(\vec{d}(t)|H)}. \tag{5.1}$$

Here $p(\vec{\vartheta}|H)$ is the probability density of the parameters based on theory, assumptions, or previous observations (the prior); $p(\vec{d}(t)|\vec{\vartheta}, H)$ is the joint probability distribution as a function of parameters given fixed data (the likelihood); and $p(\vec{d}(t)|H)$ is the marginalized likelihood, also called evidence.

The goal of Riley *et al.* is to produce posterior probability measurements of the mass, radius, and other model parameters for a given pulse-profile model and a set of NICER observations of the pulsar J0030+0451. Box (4) in Figure 32 shows an example schematic of a two-dimensional marginalized posterior of mass and radius.

Each parameter's marginalized posterior probability distribution is obtained using the `MULTINEST` [208] implementation of the nested sampling algorithm.

Riley *et al.* explored several hotspot geometry models to determine which model was most favored. However, we only consider the two of the most likely used models from their analysis and focus on the posterior probabilities for the parameters of these models. To keep the scope of our work reasonable, we neglect models with lower evidence values or higher complexity.

The hotspot geometry used in the most favoured model of Riley *et al.* involves two hot regions on the pulsar's surface. The first hotspot is a hot circular disk, whereas the higher temperature in the second hot region lies in the arc-shaped region. This model is named 'ST+PST' (Single Temperature + Protruding Single Temperature), shown in Figure 32. Using this model, Riley *et al.* found that the mass of the pulsar PSR J0030+0451 is $M = 1.34^{+0.15}_{-0.16}\ M_\odot$, and the equatorial radius is $R_{\rm eq} = 12.71^{+1.14}_{-1.19}$ km. The bounds mentioned here are the 16% and 84% quantiles from the posterior distribution obtained. The compactness $M/R_{\rm eq}$ is measured to be $0.16^{+0.01}_{-0.01}$. In comparison, Miller *et al.* [204] measured the mass and radius to be $M = 1.44^{+0.15}_{-0.14}\ M_\odot$ and $R_{\rm eq} = 13.02^{+1.24}_{-1.06}$ km. The second Riley *et al.* model we investigate is 'ST+EST' (Single Temperature + Eccentric Single temperature), which differs from ST+PST in that the second hot region is an eccentric annular ring. The model ST+EST gives larger radius and mass ($R_{\rm eq} = 13.89^{+1.14}_{-1.30}$ km and $M = 1.46^{+0.17}_{-0.18}\ M_\odot$, respectively).

5.3 Computational Considerations

The *X-PSI* code used by Riley *et al.* is an open-source code written primarily in Python 2.7, with additional Cython support. As noted in our previous work, Python code presents challenges in reproducibility due to its need for libraries that may not be installed (or may be installed at a different version) on the platform where the code is executed to reproduce an analysis. To address this, Riley *et al.* provided a Python 2.7 Conda environment to install the code and its dependencies. Although this does not isolate the code in the same was as containerization, it facilitates the installation of *X-PSI* and necessary libraries at the correct version.

The documentation provided by Riley *et al.* indicated that they used v0.1 of *X-PSI* to infer the properties of PSR J0030+0451; this tagged code was made available on GitHub and was straightforward to obtain and install. Riley *et al.* also released a Zenodo repository[3] that contains the phase-folded X-ray data from NICER used as input to the analysis, the configuration files for *X-PSI* v0.1, the submit scripts for the job, the output files of the job, and the files containing the posterior samples for each analysis. This thorough release of data and configuration files makes it possible to reproduce the original analysis, given sufficient computational resources. The repository comes with a `README.txt` that briefly describes each file and its use. For our analysis, we use the configuration files from the repository, changing the paths to the input data and output files wherever necessary.

The *X-PSI* analysis is computationally expensive. For example, obtaining marginalized posteriors for the ST+PST Bayesian analysis took 42,453 wall clock hours (see Table 2. from Riley *et al.*). The analysis involves $\mathcal{O}(10^8)$ likelihood evaluations each taking $\mathcal{O}(1)$ second of evaluation time. The likelihood calculation involves simulating hotspots on the star's surface, ray tracing the radiation to include relativistic effects, and creating an instance of the X-ray pulse that a distant observer would detect, making likelihood evaluation the most expensive step. While running *X-PSI* on a single compute node was straightforward, the likelihood evaluations must be executed on multiple compute nodes in parallel to complete the analysis within a reasonable time. To execute the analysis in parallel across multiple compute nodes, *X-PSI* uses the Message Passing Interface (MPI) library.

To distribute the software and input data on each compute node, we used the CERN Virtual Machine File System (CVMFS). This shared filesystem makes scientific software easily available and accessible on HPC clusters. The software stack for interprocess communication uses the `mpi4py` library [209] to create Python bindings to MPI libraries written in C++ and installed as dynamic shared libraries. The object code in these libraries executes the inter-process communication using system calls. Our main reproducibility challenge was to produce a containerized version of *X-PSI* that could execute the analysis using MPI across multiple (possibly heterogeneous) compute nodes.

Following our previous experience, we created a Docker image containing the

---

[3]https://doi.org/10.5281/zenodo.5506838

complete *X-PSI* software stack for execution as a stand-alone image. Using a base Debian Miniconda image[4], we installed *X-PSI* and the required dependencies in it using the files provided by Riley *et al.*. While the Docker container streamlines the installation of *X-PSI* and its dependencies, it presents a problem of running the analysis in parallel on multiple compute nodes as code running each docker container running on a compute cluster needs to communicate with the other containers. While this is possible, it is challenging without administrative control of the host machines.

Singularity provides a controlled, containerized environment with the advantage that codes running in the image can access the network capabilities of the host. Unlike Docker's full virtual machine containerization, Singularity creates images that overlay on the host machine. Therefore, if the host's operating system is configured to allow interprocess communication for MPI (as is common in cluster environments), it can be used by code running in the Singularity image. For this to work, the Singularity image must contain the exact version of the `mpi4py` and the MPI-shared libraries as the host machine. To address this challenge, we used scripts by the Open Science Grid team that convert Docker containers into Singularity images.

We use HTCondor as the job scheduler and the Syracuse University Gravitational-wave Group (SUGWG) cluster for our analysis. This is a heterogeneous combination of Intel® Xeon® Gold 6248R @3.00GHz, E5-2660v2 @2.20GHz, E5-2698v3 @2.30GHz, X5650 @2.67GHz, X5550 @2.67GHz, E5-2620 0 @2.00GHz, and AMD EPYC 7702P, EPYC 7543 processors). The cluster uses a CentOS operating system configured to allow codes to use OpenMPI [210] implementation of MPI.

Since the Docker container (and hence the derived Singularity image) used to host *X-PSI* has a Debian operating system, we made a copy of the OpenMPI shared libraries that are installed on the SUGWG compute nodes, deployed it in the container, and configured the runtime linker so that the Python interpreter inside the container could access these libraries. This ensures that the OpenMPI within the container has identical paths and configurations to the host compute nodes. The analysis can then be launched using the HTCondor job scheduler. HTCondor uses `mpirun` to execute *X-PSI* from inside the Singularity container across multiple compute nodes. Figure 33 shows the schematic depicting the software setup.

---

[4]https://hub.docker.com/r/continuumio/miniconda

5.4   Reproducing the J0030 Result

We reproduce the original analyses using the ST+PST and ST+EST models using the above software setup. Additionally, we submit jobs using the ST+PST and ST+EST models with broader radius priors than the original analyses. Table 13 shows the job statistics and summary of results obtained for the analysis in Riley *et al.* and for our work. We also show the information provided in the Zenodo release by Riley *et al.*. The results from the data in the Zenodo repository and those in the publication are different because Riley *et al.* post-processed the posterior samples (present in the Zenodo repository) to re-evaluate the evidence. We do not repeat this post-processing step since we do not have access to a working post-processing script used by the original study's authors.

Figure 34 shows the posteriors for the model ST+PST from the Zenodo repository (results used by Riley *et al.*) in blue, from the reproducibility analysis in orange, and for the analysis with the broader radius priors in green. Figure 35 shows when the model ST+EST was used. The figures show one and two-dimensional marginal posteriors for the mass M (in solar masses), the equatorial radius R_{eq} (in km), and the compactness M/R_{eq} (in solar mass/km) of the pulsar. The original and reanalysis analysis involved 19 parameters (for ST+PST and ST+EST models). For brevity, we show the posteriors for only three parameters, mass, radius, and compactness.

We find that we can reproduce the results from the original analyses. We get the exact measurement for the three quantities of interest with the same 68 percentile confidence interval. The minor differences in the posteriors are statistical, and one expects this order of fluctuation after each repetition of the analysis. Since Markov Chain Monte Carlo sampling is random, one cannot obtain identical reproduction of the positions of the sample points. The samples exploring the posterior space accumulate around the region with high probability. There would be some fluctuation at the periphery of this distribution, which is reflected in the deviations in the 99% contour lines, where the sampler population density is sparse. The inner 68% and 95% contour lines in the posterior from the reanalysis show much less deviation from the posterior of the original analysis.

Moreover, the value for evidence we get for the reanalysis is close to the value reported in the original paper. Again, there would be statistical fluctuation over

repetition, and one would not expect the evidence to be precisely the same. The values obtained are within the margin of fluctuation one would expect from run to run.

Post-processing and plotting the output of the Bayesian analysis proved to be an obstacle to the reproducibility of the original results. Although the Zenodo repository had all the configuration files and submitted scripts to start the analysis, the post-processing and plotting scripts were absent. These scripts are necessary to produce a figure that is identical to the figure that was published. The documentation of *X-PSI* describes the post-processing module of the software. However, the documentation describes v0.5 of *X-PSI*, which is backward incompatible with v0.1 used in the original analysis. We found that the post-processing module of *X-PSI* failed to process the output files from `MULTINEST`. Instead, we used the post-processing modules and scripts from PyCBC Inference [156]–a Python toolkit for Bayesian analysis of gravitational-wave signals–to plot all the posteriors. We converted the `.dat` files produced by the `MULTINEST` sampler into PyCBC-readable `.hdf` files and used the `pycbc_plot_posterior` script on these files. This emphasizes the importance of releasing the set of all the executables used in the original analysis, including the post-processing and the plotting scripts.

In addition to reproducing the original analyses, we also explore the effects of using broader prior bounds for the radius. The original analysis put the upper bound at 16 km for the neutron star's radius. We change it to 25 km and found that the posteriors are unaffected. This test is useful for the model ST+EST, where the posteriors are cut off at the upper bound of the prior. We aim to check if the posteriors were affected if the prior base was increased. Since the posteriors do not change significantly, we conclude that the data observed by the NICER instrument is informative and that our choice of priors does not heavily influence the Bayesian analysis. The posteriors for the analyses with broader radius priors for models ST+PST and ST+EST are shown in green in Figures 34 and 35, respectively.

For the model ST+PST, we also perform an analysis with an increased number of live points used by the sampler to sample the posterior probability distribution. The original analysis used 1000 live points, and we increased it to 4000 live points to check the robustness of the result to the sampler configuration. The posteriors do not significantly change when the number of live points for the sampler increases.

5.5   Lessons Learned

We compiled a list of challenges we encountered while reproducing the analysis and noted the lessons learned. We discuss the guidelines to make computational analysis, such as that done by Riley *et al.*, reproducible. Table 14 lists whether the data, software, and documentation components were available, incomplete, or unavailable before our reproducibility study.
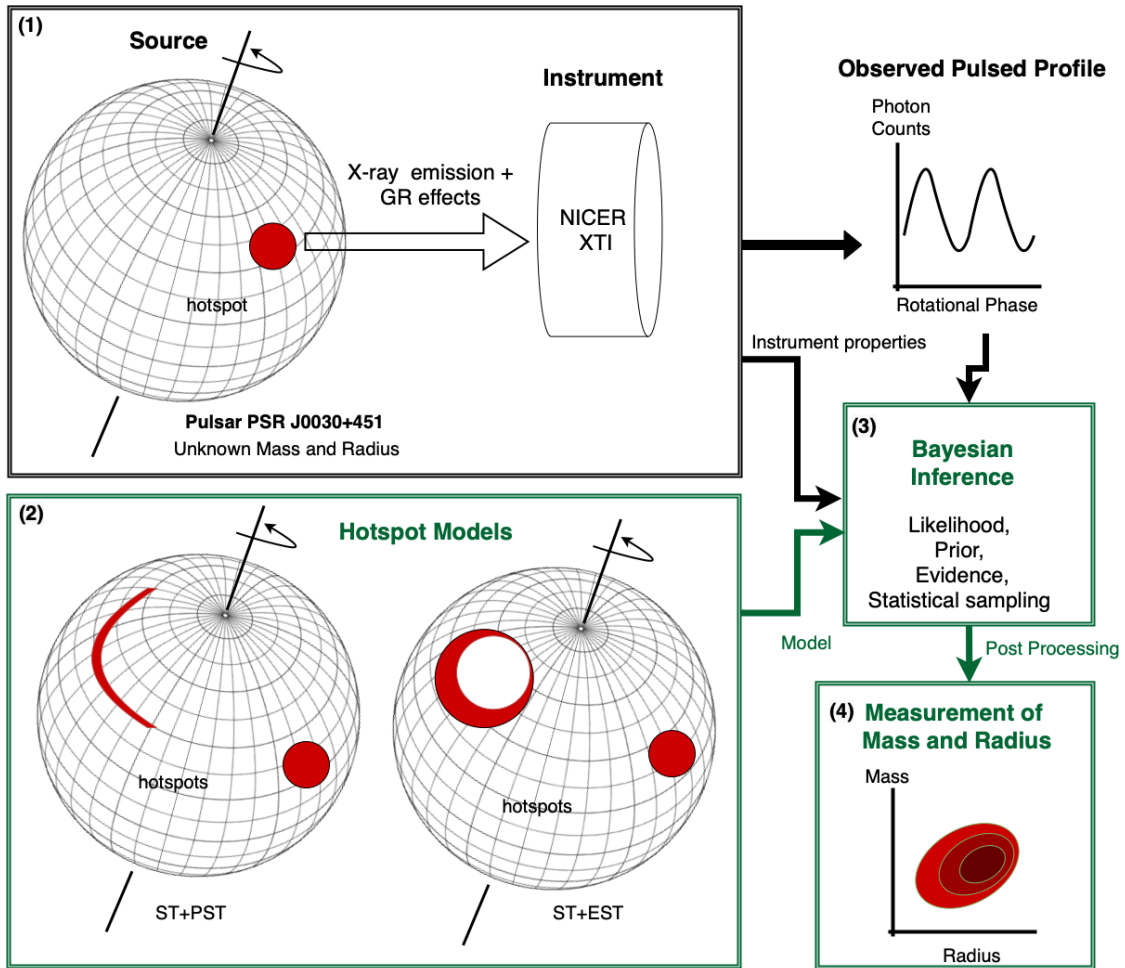
Figure 32: Schematic showing how the mass and radius of PSR J0030+0451 can be measured using X-ray data observed by NICER. The parts of the analysis done by Riley *et al.* using *X-PSI* are shown as green boxes. *X-PSI* uses the data observed by NICER (box 1 and the observed pulse profile), and the hotspot models that simulate the X-ray emission from the pulsar (box 2), to perform Bayesian parameter estimation (box 3) and measure the posterior probabilities for mass and radius of the target pulsar (box 4). The two examples of hotspot models shown in the figure are 'ST+PST' (Single Temperature + Protruding Single Temperature) and 'ST+EST' (Single Temperature + Eccentric Single temperature).
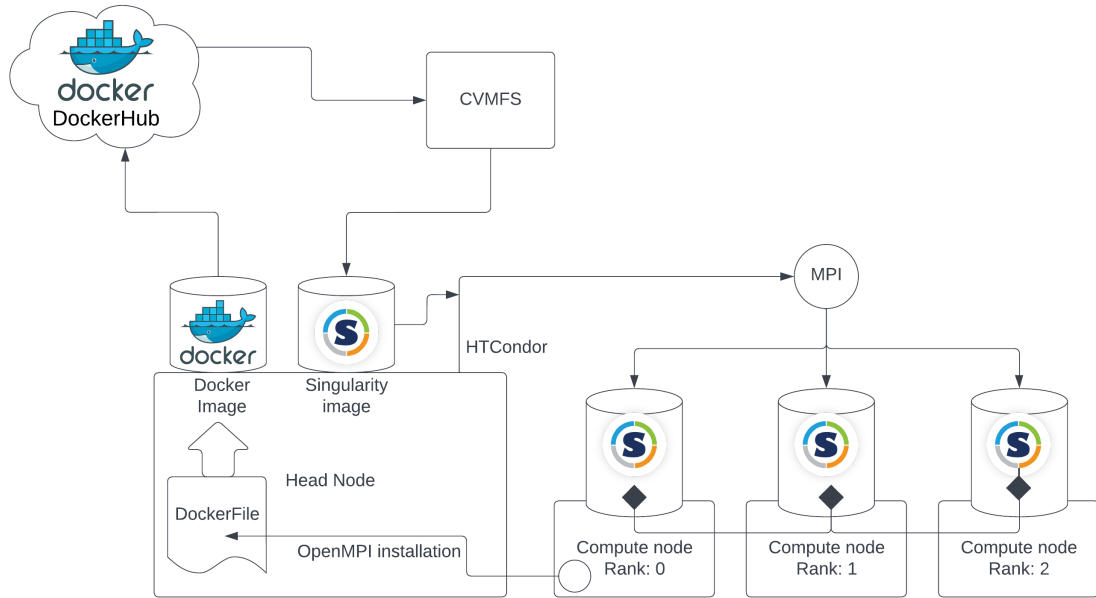
Figure 33: Schematic showing the software components used in our workflow execution. We create a Docker image on the login node on the `sugwg-condor` cluster which has the replica of the OpenMPI installation present on any of the compute nodes. This Docker image is then pushed to Docker Hub cloud storage. CVMFS converts the Docker container into a Singularity container and makes it available for use on the cluster. We use the HTCondor job scheduler to deploy the Singularity containers on the compute nodes, thus fulfilling the parallelization requirements of the analysis.

Model		Results in Riley *et al.*	Zenodo release	Reproducibility analysis	Broader radius priors	4000 live points
ST+PST	$\ln Z$	-36368.28	-36366.65	-36365.52	-36365.24	-36364.39
	Mass $[M_\odot]$	$1.34^{+0.15}_{-0.16}$	$1.34^{+0.15}_{-0.15}$	$1.34^{+0.16}_{-0.15}$	$1.36^{+0.16}_{-0.16}$	$1.35^{+0.16}_{-0.16}$
	Eq. Radius [km]	$12.71^{+1.14}_{-1.19}$	$12.7^{+1.1}_{-1.2}$	$12.8^{+1.2}_{-1.2}$	$12.9^{+1.2}_{-1.2}$	$12.9^{+1.3}_{-1.2}$
	Z evaluations	78,343,018	78,343,018	157,814,515	139,593,698	589,513,174
	Replacements	57,972	57,972	56,896	56,596	225,856
	Posterior Samples	20,177	12,242	11,896	11,749	46,488
	CPU hours	42,453	42,453	48,384	55,296	179,712
	Number of cores	960	960	288	384	288
ST+EST	$\ln Z$	-36367.81	-36366.17	-36366.14	-36366.16	-
	Mass $[M_\odot]$	$1.46^{+0.17}_{-0.18}$	$1.46^{+0.17}_{-0.18}$	$1.46^{+0.17}_{-0.17}$	$1.47^{+0.19}_{-0.19}$	-
	Eq. Radius [km]	$13.89^{+1.14}_{-1.30}$	$13.9^{+1.1}_{-1.3}$	$13.8^{+1.2}_{-1.2}$	$14^{+1.4}_{-1.4}$	-
	Z evaluations	88,965,106	88,965,106	89,850,127	143,920,078	-
	Replacements	53,149	53,149	53,098	52,358	-
	Posterior Samples	20,177	12,242	10,944	10,828	-
	CPU hours	61,210	61,210	48,384	55,296	-
	Number of cores	960	960	288	480	-

Table 13: Summary of job statistics for the original analysis published by Riley *et al.* in the Zenodo repository, and the reanalyses. We show the key results in the first section of the models ST+PST and ST+EST for the Bayesian evidence ($\ln Z$) obtained from the analysis, and the measurement of mass and the equatorial radius of the target pulsar. The results in Riley *et al.* are obtained after post-processing the data they obtained from the job. The latter has been publicly released in the Zenodo repository, so the computational details (CPU hours, number of cores) for these two columns will be the same. In contrast, the evidence values and measurements of mass and radius will differ.
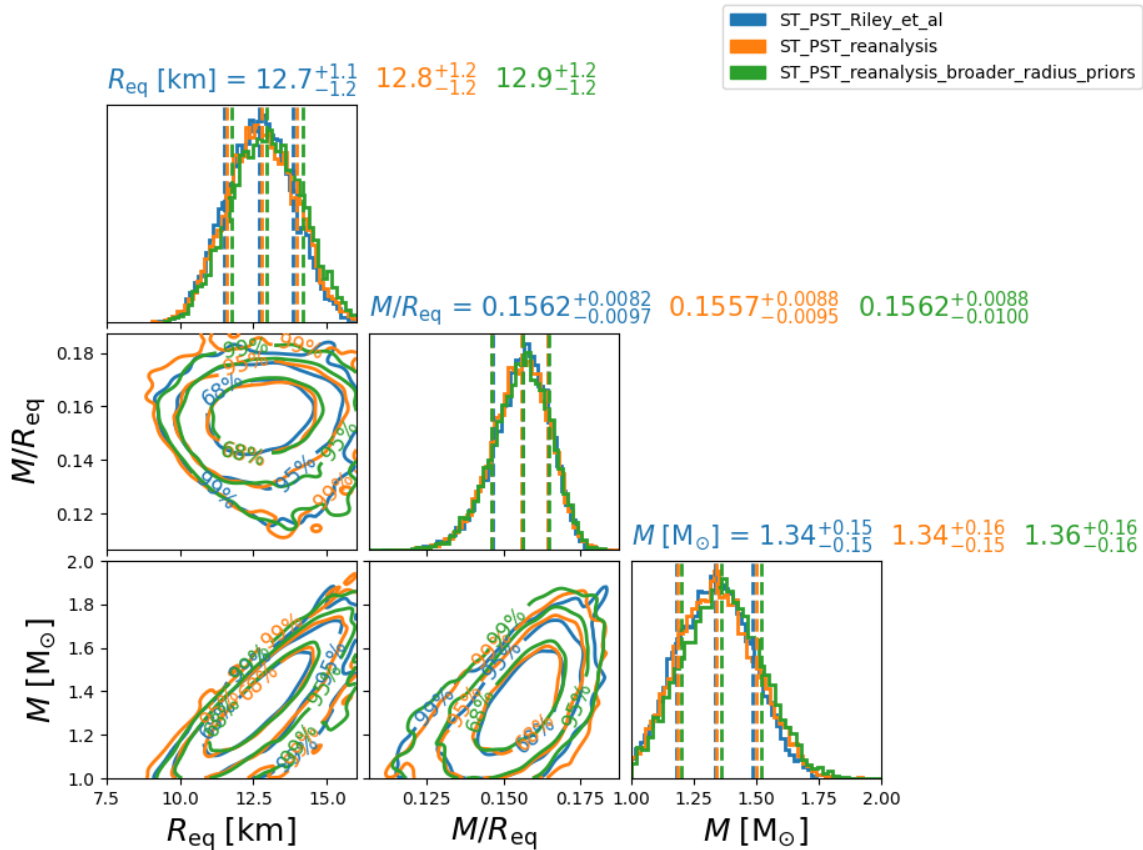
Figure 34: Comparison of posterior probability distributions for mass, radius, and compactness of J0030 obtained by Riley *et al.* (blue), reproducing the analysis (orange), and for the analysis with the broader radius priors (green), using the hotspot model ST+PST. The corner plot shows the three parameters' one and two-dimensional marginal posteriors. The priors used for the re-analysis are the same as in the original analysis.
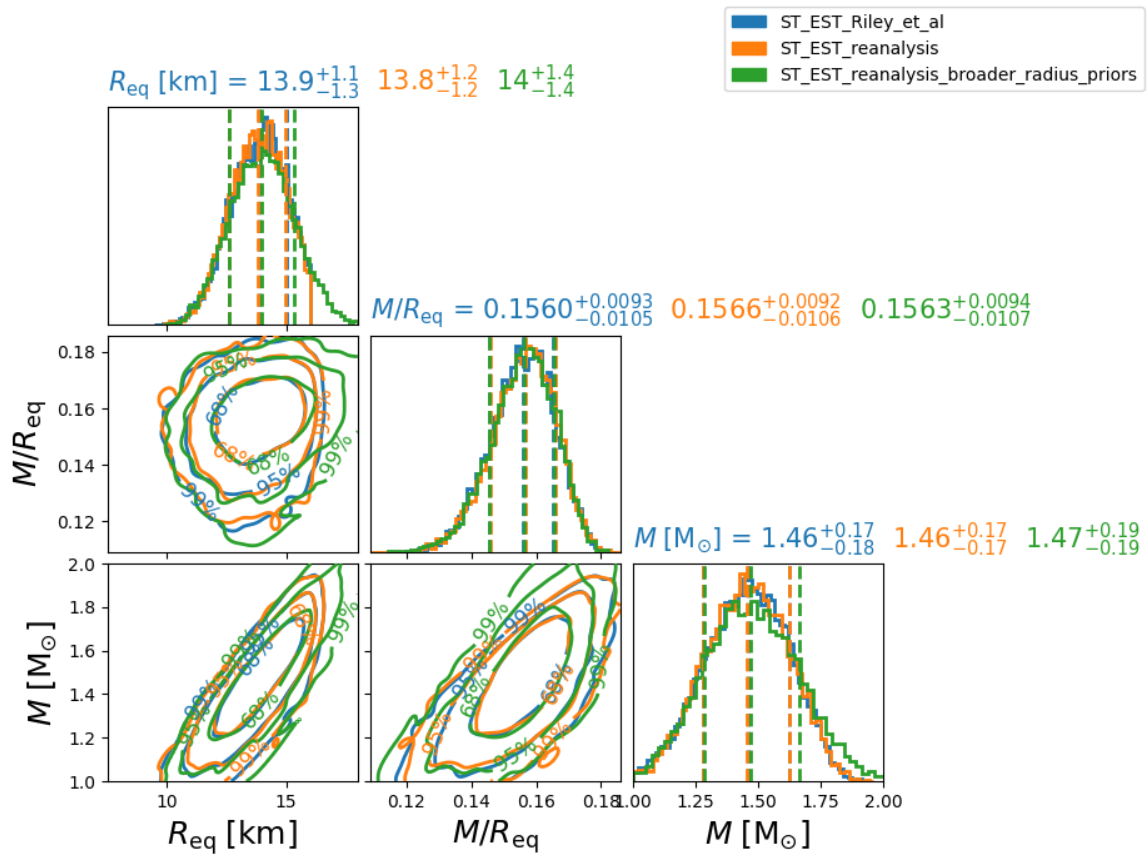
Figure 35: Comparison of posterior probability distributions for mass, radius, and compactness of J0030 obtained by Riley *et al.* (blue), reproducing the analysis (orange), and for the analysis with the broader radius priors (green), using the hotspot model ST+EST. The corner plot shows the three parameters' one and two-dimensional marginal posteriors. The priors used for the re-analysis are the same as in the original analysis.

Data

Raw input data	Unavailable	
Processed input data	Available	https://doi.org/10.5281/zenodo.5506838
Output data	Available	https://doi.org/10.5281/zenodo.5506838

Software

Code	v0.1 Available [203]	https://github.com/xpsi-group
Documentation	Available for v0.5	https://xpsi-group.github.io/xpsi/
Software dependencies	Available	
Configuration files	Available	
Post-processing scripts	Unavailable	

Table 14: Availability of data, scripts, code, and documentation before our reproducibility study.

Input Data Availability. The raw data for the NICER observation of PSR J0030+451 was not made available by Riley *et al.* through their Zenodo repository. However, processed data was included in the Zenodo release and had accompanying documentation.

Software Availability. Riley *et al.* use *X-PSI* v0.1 to analyze PSR J0030+451 data. The code is open source and publicly available on GitHub.

Software Documentation. *X-PSI* comes with extensive, publicly-accessible documentation. Since the framework of the code is modular, the documentation goes over each module in depth, explaining the physics associated with it and providing examples. However, the code and its documentation have evolved significantly since they were used for the original analysis. The documentation during our reproducibility effort relates to *X-PSI* v0.5, whereas the original analysis used *X-PSI* v0.1.

Software Installation and Dependencies. The instructions for installation of *X-PSI* include information about all the software dependencies. They also provide `.yml` files that can be used to create a virtual environment with the basic dependencies resolved. The installation manual has clear instructions for installing the sampler and the parallelization software.

Configuration files. The Zenodo repository has all the configuration files used by *X-PSI* to generate the hotspot models. The availability of the configuration files was crucial to successfully reproducing the results. The configuration files shared in the Zenodo repository streamline the setup of the jobs. Combined with the documentation, modifying the original analysis and changing the sampler configuration and the prior bounds for radius was easy.

Computational Resources The original analysis of Riley *et al.* used the Dutch national SURFsara supercomputer Cartesius. As is common in attempts to reproduce analyses, we did not have access to these computational resources or the original environment used by Riley et al. To execute *X-PSI* on the large-scale resources available to us, we had to adapt the *X-PSI* deployment to fit a different scheduler and create an overlay container that could run on this cluster. By demonstrating that this is possible, we show that it is possible to overcome access the barrier to reproducibility presented by access to computing resources.

Post-processing Scripts. The unavailability of the post-processing scripts to analyze the output data from the analysis and plot the posteriors made it unfeasible

for us to generate the same plot as the one present in the publication of the original results. We had to use PyCBC software to plot the posterior distributions. Post-processing scripts are a crucial part of the software workflow in reproducibility. The scripts to process the raw data are also absent.

Output Data Availability. The Zenodo repository included the posterior output files for all the analysis jobs performed by the original study's authors. The output files included all the files generated by the sampler `MULTINEST`, including the posterior file and the history of all the sample points throughout the analysis. It also includes the output of the jobs — including the job scheduler logs and error messages generated by *X-PSI* during the analysis.

5.6   Conclusions

Conducting reproducible research is an essential step towards open science. In this article, we described the procedure and challenges involved in reproducing the measurement of mass and radius of the pulsar PSR J0030+451 from the X-ray data observed by NICER.

Given the release of the Zenodo repository containing the data and the configuration scripts used for the original analysis, we were able to reproduce the analysis by Riley *et al.* to measure the mass and the radius of PSR J0030+451. The post-processing scripts plot the posteriors using the output file produced by *X-PSI* is absent. We could not use the code and its documentation to plot the posteriors as shown in the original publication. Instead, after converting the output file to an `.hdf` file, we used the post-processing module of PyCBC to plot the posteriors. This highlights the importance of releasing the entire set of scripts, from data processing to post-processing of the analysis output, to be released in a containerized format to reproduce the analysis.

Apart from reproducing the measurement, we changed the prior probabilities of the radius from the original analysis, increasing the upper bound from 16 km to 25 km. Despite the broader range of possible radii from the prior, we get the exact posterior distribution as the original analysis. We also increased the number of points used by the sampler from 1000 to 4000 and found no significant change in the posterior probability distribution.

Our work also shows that that is possible to reproduce analyses that require large-scale computational resources without access to the original hardware. This is significant, as access to resources is often a major barrier to reproducibility. Scientists wishing to reproduce findings might not have allocations on the original resources, or the original resource may have been decommissioned. Using the Singularity overlay container shows that executing MPI code across a heterogeneous cluster that uses a different operating system than the original hardware is possible.

To aid future researchers who want to reproduce the analysis of PSR J0030+451 data, the Docker container created for our analysis is publicly available[5]. The specific tag of the container used for the reproducibility analyses is '8d3b23d'. The Dockerfile is also available publicly on the GitHub repository accompanying this article [6]. We provide the post-processing script and the PyCBC installation required to produce the posterior corner plots.

---

[5] https://hub.docker.com/r/chaitanyaafle/nicer
[6] https://github.com/sugwg/nicer-reproducibility-J0030

Chapter 6

Conclusions

Neutron stars provide a unique opportunity for us to understand the behavior of dense matter. In order to extract fundamental physics from these laboratories, we need to observe and analyze the astrophysical signals from them. In this thesis, we discussed methods to analyze gravitational-wave signals from core-collapse supernovae—the birthplace of neutron stars, and X-rays from the surface of galactic pulsars. First, we discussed how to optimize Cosmic Explorer, the next-generation gravitational-wave detector, to maximize its range to detect core-collapse supernovae. Based on three-dimensional simulations for core-collapse and the corresponding gravitational-wave waveform emitted, the detection range for these waveforms is limited to within our galaxy even in the era of third-generation detectors. The event rate is two supernovae per century for the Milky Way. We find from the waveforms that, to detect core-collapse supernovae with an event rate of one per year, the gravitational-wave detectors need a strain sensitivity of 3×10^{-27} Hz$^{-1/2}$ in a frequency range from 100 Hz to 1500 Hz. We also explore detector configurations technologically beyond the scope of third-generation detectors. We find with these improvements, the event rate for gravitational-wave observations from supernovae is still low, but is improved to one in twenty years. However, if detected by Cosmic Explorer in conjunction with the electromagnetic and neutrino signals, the gravitational-wave signal from a supernova will be spectacular and will be able to answer a host of fundamental physics questions.

We have investigated the ability of gravitational-wave observatories to extract the properties of the collapsing progenitor from the gravitational waves radiated. We use simulations of supernovae that explore a variety of progenitor core rotation rates and

nuclear equations of state and examine the ability of current and future observatories to determine these properties using gravitational-wave parameter estimation. We use principal component analysis of the simulation catalog to determine the dominant features of the waveforms and create a map between the measured properties of the waveform and the physical properties of the progenitor star. We use Bayesian parameter inference and the parameter map to calculate posterior probabilities for the physical properties given a gravitational-wave observation. We demonstrate our method on a random sample of the waveform catalog that was excluded from construction of the principal component analysis and estimate the ratio of the progenitor's core rotational kinetic energy to potential energy (β) and the post bounce oscillation frequency. For a supernova at the distance of the galactic center (8.1 kpc) with $\beta = 0.02$ our method can estimate β with a 90% credible interval of 0.004 for Advanced LIGO, improving to 0.0008 for Cosmic Explorer, the proposed third-generation detector. We demonstrate that if the core is rotating sufficiently rapidly for a signal source within the Milky Way observed by Cosmic Explorer, our method can also extract the post bounce oscillation frequency of the protoneutron star to a precision of within 5 Hz (90% credible interval) allowing us to constrain the nuclear equation of state. For a supernova at the distance of the Magellanic Clouds (48.5 kpc) Cosmic Explorer's ability to measure these parameters decreases slightly to 0.003 for rotation and 11 Hz for the postbounce oscillation frequency (90% credible interval). Sources in Magellanic Clouds with $\beta < 0.02$ will be too distant for Advanced LIGO to measure these properties.

We have analyzed the gravitational-wave strain signals from two- and three-dimensional simulations of core-collapse supernovae generated using the code FORNAX, including a subset of the two-dimensional simulations having non-zero core rotation at the core bounce. A dominant source of time changing quadrupole moment is the $l = 2$ fundamental mode ($f-$ mode) oscillation of the proto-neutron star. From the time-frequency spectrogram of the gravitational-wave strain we see that, starting ~ 400 ms after the core bounce, most of the power lies within a narrow track that represents the frequency evolution of the $f-$mode oscillations. The $f-$mode frequencies obtained from linear perturbation analysis of the angle-averaged profile of the protoneutron star corroborate what we observe in the spectrograms of the gravitational-wave signal. We explore the measurability of the $f-$mode frequency

evolution of protoneutron star for a supernova signal observed in the third-generation gravitational-wave detectors. Measurement of the frequency evolution can reveal information about the masses, radii, and densities of the proto-neutron stars. We find that if the third generation detectors observe a supernova within 10 kpc, we can measure these frequencies to within $\sim$90% accuracy. We can also measure the energy emitted in the fundamental $f-$mode using the spectrogram data of the strain signal. We find that the energy in the $f-$mode can be measured to within 20% error for signals observed by Cosmic Explorer using simulations with successful explosion, assuming source distances within 10 kpc. In the future, we plan to jointly analyze the gravitational-wave signal with the neutrino signal from supernovae, since the primary instigators for both is the accreting matter on the proto-neutron star. Similar analysis of the time-frequency spectrograms can also be done for the postmerger signal of a binary neutron star merger.

We reproduced the results of Riley et al., in which they reported Bayesian parameter measurements of the mass and the star's radius using pulse-profile modeling of the X-ray data of the pulsar PSR J0030+0451 observed by NASA's Neutron Star Interior Composition Explorer (NICER) mission. We reproduce their result using the open-source software X-PSI and publicly available data within expected statistical errors. We note the challenges we faced in reproducing the results and demonstrate that the analysis can be reproduced and reused in future works by changing the prior distribution for the radius and the sampler configuration. We find no significant change in the measurement of the mass and radius, demonstrating that the original result is robust to these changes. Finally, we provide a containerized working environment that facilitates third-party reproduction of the measurements of mass and radius of PSR J0030+0451 using the NICER observations. This is the first step in creating a joint electromagnetic—gravitational-wave analysis pipeline. In the future, we plan to combine the X-ray data for PSR J0030+0451, PSR J0740+6620, and GW170817 to provide joint, multi-messenger constraints on the neutron star equation of state.

Bibliography

[1] Roland Schilling. Angular and frequency response of lisa. *Classical and Quantum Gravity*, 14(6):1513, 1997.

[2] Reed Essick, Salvatore Vitale, and Matthew Evans. Frequency-dependent responses in third generation gravitational-wave detectors. *Physical Review D*, 96(8):084004, 2017.

[3] Rhondale Tso, Davide Gerosa, and Yanbei Chen. Optimizing LIGO with LISA forewarnings to improve black-hole spectroscopy. *arXiv preprint arXiv:1807.00075*, 2018.

[4] K. Hebeler, J. D. Holt, J. Menendez, and A. Schwenk. Nuclear forces and their impact on neutron-rich nuclei and neutron-rich matter. *Ann. Rev. Nucl. Part. Sci.*, 65:457–484, 2015.

[5] James M. Lattimer and Madappa Prakash. The Equation of State of Hot, Dense Matter and Neutron Stars. *Phys. Rept.*, 621:127–164, 2016.

[6] C. Drischler, J. W. Holt, and C. Wellenhofer. Chiral Effective Field Theory and the High-Density Nuclear Equation of State. *Ann. Rev. Nucl. Part. Sci.*, 71:403–432, 2021.

[7] J. M. Lattimer and M. Prakash. The physics of neutron stars. *Science*, 304:536–542, 2004.

[8] G. Baym and C. Pethick. Physics of Neutron Stars. *Ann. Rev. Astron. Astrophys.*, 17:415–443, 1979.

[9] M. Oertel, M. Hempel, T. Klähn, and S. Typel. Equations of state for supernovae and compact stars. *Rev. Mod. Phys.*, 89(1):015007, 2017.

[10] Debarati Chatterjee and Isaac Vidaña. Do hyperons exist in the interior of neutron stars? *Eur. Phys. J. A*, 52(2):29, 2016.

[11] Gordon Baym, Tetsuo Hatsuda, Toru Kojo, Philip D. Powell, Yifan Song, and Tatsuyuki Takatsuka. From hadrons to quarks in neutron stars: a review. *Rept. Prog. Phys.*, 81(5):056902, 2018.

[12] J. M. Lattimer. Neutron Stars and the Nuclear Matter Equation of State. *Ann. Rev. Nucl. Part. Sci.*, 71:433–464, 2021.

[13] Richard C. Tolman. Static solutions of Einstein's field equations for spheres of fluid. *Phys. Rev.*, 55:364–373, 1939.

[14] J. R. Oppenheimer and G. M. Volkoff. On massive neutron cores. *Phys. Rev.*, 55:374–381, 1939.

[15] G. Raaijmakers et al. Constraining the dense matter equation of state with joint analysis of NICER and LIGO/Virgo measurements. *ApJ*, 893(1):L21, 2020.

[16] Andreas Bauswein, Niels-Uwe F Bastian, David B Blaschke, Katerina Chatziioannou, James A Clark, Tobias Fischer, and Micaela Oertel. Identifying a first-order phase transition in neutron-star mergers through gravitational waves. *Physical review letters*, 122(6):061102, 2019.

[17] Slavko Bogdanov et al. Snowmass 2021 Cosmic Frontier White Paper: The Dense Matter Equation of State and QCD Phase Transitions. In *Snowmass 2021*, 9 2022.

[18] J. Aasi et al. Advanced LIGO. *Class. Quant. Grav.*, 32:074001, 2015.

[19] F. Acernese et al. Advanced Virgo: a second-generation interferometric gravitational wave detector. *Class. Quant. Grav.*, 32(2):024001, 2015.

[20] B. P. Abbott et al. Prospects for observing and localizing gravitational-wave transients with Advanced LIGO, Advanced Virgo and KAGRA. *Living Rev. Rel.*, 21(1):3, 2018.

[21] B. P. Abbott et al. Binary Black Hole Mergers in the first Advanced LIGO Observing Run. *Phys. Rev. X*, 6(4):041015, 2016. [Erratum: Phys.Rev.X 8, 039903 (2018)].

[22] Benjamin P. Abbott et al. GW170104: Observation of a 50-Solar-Mass Binary Black Hole Coalescence at Redshift 0.2. *Phys. Rev. Lett.*, 118(22):221101, 2017. [Erratum: Phys.Rev.Lett. 121, 129901 (2018)].

[23] B. . P. . Abbott et al. GW170608: Observation of a 19-solar-mass Binary Black Hole Coalescence. *Astrophys. J. Lett.*, 851:L35, 2017.

[24] B. P. Abbott et al. GWTC-1: A Gravitational-Wave Transient Catalog of Compact Binary Mergers Observed by LIGO and Virgo during the First and Second Observing Runs. *Phys. Rev.*, X9(3):031040, 2019.

[25] B. P. Abbott et al. GW170814: A Three-Detector Observation of Gravitational Waves from a Binary Black Hole Coalescence. *Phys. Rev. Lett.*, 119(14):141101, 2017.

[26] B. P. Abbott et al. Observation of Gravitational Waves from a Binary Black Hole Merger. *Phys. Rev. Lett.*, 116(6):061102, 2016.

[27] B. P. Abbott et al. GW170817: Observation of Gravitational Waves from a Binary Neutron Star Inspiral. *Phys. Rev. Lett.*, 119(16):161101, 2017.

[28] B. P. Abbott et al. Multi-messenger Observations of a Binary Neutron Star Merger. *Astrophys. J. Lett.*, 848(2):L12, 2017.

[29] Benjamin P. Abbott et al. Sensitivity of the Advanced LIGO detectors at the beginning of gravitational wave astronomy. *Phys. Rev. D*, 93(11):112004, 2016. [Addendum: Phys.Rev.D 97, 059901 (2018)].

[30] Matthew Evans et al. A Horizon Study for Cosmic Explorer: Science, Observatories, and Community. 9 2021.

[31] M. Punturo et al. The Einstein Telescope: A third-generation gravitational wave observatory. *Class. Quant. Grav.*, 27:194002, 2010.

[32] W. Baade and F. Zwicky. On Super-novae. *Proceedings of the National Academy of Science*, 20(5):254–259, May 1934.

[33] Stirling A. Colgate and Richard H. White. The Hydrodynamic Behavior of Supernovae Explosions. *Astrophys. J.*, 143:626, 1966.

[34] S.E. Woosley, A. Heger, and T.A. Weaver. The evolution and explosion of massive stars. *Rev. Mod. Phys.*, 74:1015–1071, 2002.

[35] Alexander Heger, C.L. Fryer, S.E. Woosley, N. Langer, and D.H. Hartmann. How massive single stars end their life. *Astrophys. J.*, 591:288–300, 2003.

[36] ChristianD. Ott. The Gravitational Wave Signature of Core-Collapse Supernovae. *Class. Quant. Grav.*, 26:063001, 2009.

[37] Hans-Thomas Janka. Explosion Mechanisms of Core-Collapse Supernovae. *Ann. Rev. Nucl. Part. Sci.*, 62:407–451, 2012.

[38] B. Müller. Neutrino Emission as Diagnostics of Core-Collapse Supernovae. *Ann. Rev. Nucl. Part. Sci.*, 69:253–278, 2019.

[39] Chris L. Fryer and Kimberly C.B. New. Gravitational waves from gravitational collapse. *Living Rev. Rel.*, 14:1, 2011.

[40] Adam Burrows. Colloquium: Perspectives on core-collapse supernova theory. *Rev. Mod. Phys.*, 85:245, 2013.

[41] Hans A. Bethe and James R. Wilson. Revival of a stalled supernova shock by neutrino heating. *Astrophys. J.*, 295:14–23, 1985.

[42] Margaret E. Burbidge, G. R. Burbidge, William A. Fowler, and F. Hoyle. Synthesis of the elements in stars. *Rev. Mod. Phys.*, 29:547–650, 1957.

[43] Grant J. Mathews, Luca Boccioli, Jun Hidaka, and Toshitaka Kajino. Review of uncertainties in the cosmic supernova relic neutrino background. *Mod. Phys. Lett. A*, 35(25):2030011, 2020.

[44] S.E. Gossan, P. Sutton, A. Stuver, M. Zanolin, K. Gill, and C.D. Ott. Observing Gravitational Waves from Core-Collapse Supernovae in the Advanced Detector Era. *Phys. Rev. D*, 93(4):042002, 2016.

[45] B.P. Abbott et al. Optically targeted search for gravitational waves emitted by core-collapse supernovae during the first and second observing runs of advanced LIGO and advanced Virgo. *Phys. Rev. D*, 101(8):084002, 2020.

[46] Varun Srivastava, Stefan Ballmer, Duncan A. Brown, Chaitanya Afle, Adam Burrows, David Radice, and David Vartanyan. Detection Prospects of Core-Collapse Supernovae with Supernova-Optimized Third-Generation Gravitational-wave Detectors. *Phys. Rev.*, D100(4):043026, 2019.

[47] S. V. Bergh and G. A. Tammann. Galactic and extragalactic supernova rates. *Ann. Rev. Astron. Astrophys.*, 29:363–407, 1991.

[48] E. Cappellaro, M. Turatto, D. Yu. Tsvetkov, O. S. Bartunov, C. Pollas, R. Evans, and M. Hamuy. The Rate of supernovae from the combined sample of five searches. *Astron. Astrophys.*, 322:431–441, 1997.

[49] Weidong Li, Ryan Chornock, Jesse Leaman, Alexei V. Filippenko, Dovi Poznanski, Xiaofeng Wang, Mohan Ganeshalingam, and Filippo Mannucci. Nearby Supernova Rates from the Lick Observatory Supernova Search. III. The Rate-Size Relation, and the Rates as a Function of Galaxy Hubble Type and Colour. *Mon. Not. Roy. Astron. Soc.*, 412:1473, 2011.

[50] Roland Diehl et al. Radioactive Al-26 and massive stars in the galaxy. *Nature*, 439:45–47, 2006.

[51] Sherwood Richers, Christian D. Ott, Ernazar Abdikamalov, Evan O'Connor, and Chris Sullivan. Equation of State Effects on Gravitational Waves from Rotating Core Collapse. *Phys. Rev.*, D95(6):063019, 2017.

[52] Ernazar Abdikamalov, Sarah Gossan, Alexandra M. DeMaio, and Christian D. Ott. Measuring the Angular Momentum Distribution in Core-Collapse Supernova Progenitors with Gravitational Waves. *Phys. Rev.*, D90(4):044001, 2014.

[53] Harald Dimmelmeier, Christian D. Ott, Andreas Marek, and H.-Thomas Janka. The Gravitational Wave Burst Signal from Core Collapse of Rotating Stars. *Phys. Rev. D*, 78:064056, 2008.

[54] M. A. Dupret et al. Theoretical amplitudes and lifetimes of non-radial solar-like oscillations in red giants. *Astron. Astrophys.*, 506:57, 2009.

[55] Jim Fuller, Matteo Cantiello, Daniel Lecoanet, and Eliot Quataert. The spin rate of pre-collapse stellar cores: wave-driven angular momentum transport in massive stars. *The Astrophysical Journal*, 810(2):101, 2015.

[56] Alexander Heger, S. E. Woosley, and H. C. Spruit. Presupernova evolution of differentially rotating massive stars including magnetic fields. *Astrophys. J.*, 626:350–363, 2005.

[57] Christian D. Ott, Adam Burrows, Todd A. Thompson, Eli Livne, and Rolf Walder. The spin periods and rotational profiles of neutron stars at birth. *Astrophys. J. Suppl.*, 164:130–155, 2006.

[58] M. Coleman Miller and Frederick K. Lamb. Observational Constraints on Neutron Star Masses and Radii. *Eur. Phys. J. A*, 52(3):63, 2016.

[59] Feryal Özel and Paulo Freire. Masses, Radii, and the Equation of State of Neutron Stars. *Ann. Rev. Astron. Astrophys.*, 54:401–440, 2016.

[60] S. M. Morsink et al. The Oblate Schwarzschild Approximation for Light Curves of Rapidly Rotating Neutron Stars. *ApJ*, 663(2):1244, 2007.

[61] Thomas E. Riley et al. A *NICER* View of PSR J0030+0451: Millisecond Pulsar Parameter Estimation. *Astrophys. J. Lett.*, 887(1):L21, 2019.

[62] Junaid Aasi, BP Abbott, Richard Abbott, Thomas Abbott, MR Abernathy, Kendall Ackley, Carl Adams, Thomas Adams, Paolo Addesso, RX Adhikari, et al. Advanced ligo. *Classical and quantum gravity*, 32(7):074001, 2015.

[63] F Acernese, M Agathos, K Agatsuma, D Aisa, N Allemandou, A Allocca, J Amarni, P Astone, G Balestri, G Ballardin, et al. Advanced virgo: a second-generation interferometric gravitational wave detector. *Classical and Quantum Gravity*, 32(2):024001, 2014.

[64] Benjamin P Abbott, Richard Abbott, TD Abbott, MR Abernathy, Fausto Acernese, Kendall Ackley, Carl Adams, Thomas Adams, Paolo Addesso, RX Adhikari, et al. Observation of gravitational waves from a binary black hole merger. *Physical review letters*, 116(6):061102, 2016.

[65] Benjamin P Abbott, R Abbott, TD Abbott, MR Abernathy, F Acernese, K Ackley, C Adams, T Adams, P Addesso, RX Adhikari, et al. Gw151226: Observation of gravitational waves from a 22-solar-mass binary black hole coalescence. *Physical review letters*, 116(24):241103, 2016.

[66] Benjamin P Abbott, Rich Abbott, TD Abbott, Fausto Acernese, Kendall Ackley, Carl Adams, Thomas Adams, Paolo Addesso, RX Adhikari, VB Adya, et al. Gw170817: observation of gravitational waves from a binary neutron star inspiral. *Physical Review Letters*, 119(16):161101, 2017.

[67] The LIGO Scientific Collaboration, the Virgo Collaboration, B.~P. Abbott, R Abbott, T.~D. Abbott, S Abraham, F Acernese, K Ackley, C Adams, R.~X. Adhikari, and Et al. GWTC-1: A Gravitational-Wave Transient Catalog of Compact Binary Mergers Observed by LIGO and Virgo during the First and Second Observing Runs. *arXiv e-prints*, nov 2018.

[68] Tejaswi Venumadhav, Barak Zackay, Javier Roulet, Liang Dai, and Matias Zaldarriaga. New binary black hole mergers in the second observing run of advanced ligo and advanced virgo. *arXiv preprint arXiv:1904.07214*, 2019.

[69] Alexander H Nitz, Collin Capano, Alex B Nielsen, Steven Reyes, Rebecca White, Duncan A Brown, and Badri Krishnan. 1-ogc: The first open gravitational-wave catalog of binary mergers from analysis of public advanced ligo data. *The Astrophysical Journal*, 872(2):195, 2019.

[70] Alejandro Torres-Forné, Pablo Cerdá-Durán, Martin Obergaulinger, Bernhard Muller, and José A Font. Universal relations for gravitational-wave asteroseismology of proto-neutron stars. *arXiv preprint arXiv:1902.10048*, 2019.

[71] Sherwood Richers, Christian D Ott, Ernazar Abdikamalov, Evan O'Connor, and Chris Sullivan. Equation of state effects on gravitational waves from rotating core collapse. *Physical Review D*, 95(6):063019, 2017.

[72] Ernazar Abdikamalov, Sarah Gossan, Alexandra M DeMaio, and Christian D Ott. Measuring the angular momentum distribution in core-collapse supernova progenitors with gravitational waves. *Physical Review D*, 90(4):044001, 2014.

[73] Benjamin P Abbott, Richard Abbott, TD Abbott, MR Abernathy, F Acernese, K Ackley, C Adams, T Adams, P Addesso, RX Adhikari, et al. First targeted search for gravitational-wave bursts from core-collapse supernovae in data of first-generation laser interferometer detectors. *Physical Review D*, 94(10):102001, 2016.

[74] BP Abbott, R Abbott, TD Abbott, S Abraham, F Acernese, K Ackley, C Adams, RX Adhikari, VB Adya, C Affeldt, et al. All-sky search for short gravitational-wave bursts in the second advanced ligo and advanced virgo run. *arXiv preprint arXiv:1905.03457*, 2019.

[75] S E Gossan, P Sutton, A Stuver, M Zanolin, K Gill, and C D Ott. Observing gravitational waves from core-collapse supernovae in the advanced detector era. *Phys. Rev. D*, 93(4):42002, feb 2016.

[76] Weidong Li, Jesse Leaman, Ryan Chornock, Alexei V Filippenko, Dovi Poznanski, Mohan Ganeshalingam, Xiaofeng Wang, Maryam Modjaz, Saurabh Jha, Ryan J Foley, and Others. Nearby supernova rates from the Lick Observatory Supernova Search–II. The observed luminosity functions and fractions of supernovae in a complete sample. *Monthly Notices of the Royal Astronomical Society*, 412(3):1441–1472, 2011.

[77] Weidong Li, Ryan Chornock, Jesse Leaman, Alexei V Filippenko, Dovi Poznanski, Xiaofeng Wang, Mohan Ganeshalingam, and Filippo Mannucci. Nearby supernova rates from the Lick Observatory Supernova Search–III. The rate–size relation, and the rates as a function of galaxy Hubble type and colour. *Monthly Notices of the Royal Astronomical Society*, 412(3):1473–1507, 2011.

[78] M L Graham, D J Sand, C J Bildfell, C J Pritchet, D Zaritsky, H Hoekstra, D W Just, S Herbert-Fort, S Sivanandam, and R J Foley. {THE} {TYPE} {II} {SUPERNOVA} {RATE} {INz}$~$ 0.1 {GALAXY} {CLUSTERS} {FROM}

{THE} {MULTI}-{EPOCH} {NEARBY} {CLUSTER} {SURVEY}. *The Astrophysical Journal*, 753(1):68, jun 2012.

[79] Lin Xiao and J J Eldridge. Core-collapse supernova rate synthesis within 11 Mpc. *Monthly Notices of the Royal Astronomical Society*, 452(3):2597–2605, 2015.

[80] D. Radice, V. Morozova, A. Burrows, D. Vartanyan, and H. Nagakura. Characterizing the Gravitational Wave Signal from Core-collapse Supernovae. *Astrophysical J.*, 876:L9, May 2019.

[81] J. W. Murphy, C. D. Ott, and A. Burrows. A Model for Gravitational Wave Emission from Neutrino-Driven Core-Collapse Supernovae. *Astrophysical J.*, 707:1173–1190, December 2009.

[82] V. Morozova, D. Radice, A. Burrows, and D. Vartanyan. The Gravitational Wave Signal from Core-collapse Supernovae. *Astrophysical J.*, 861:10, July 2018.

[83] Bernhard Müller, Hans-Thomas Janka, and Andreas Marek. A NEW MULTI-DIMENSIONAL GENERAL RELATIVISTIC NEUTRINO HYDRODYNAMICS CODE OF CORE-COLLAPSE SUPERNOVAE. III. GRAVITATIONAL WAVE SIGNALS FROM SUPERNOVA EXPLOSION MODELS. *The Astrophysical Journal*, 766(1):43, mar 2013.

[84] Pablo Cerdá-Durán, Nicolas DeBrye, Miguel A. Aloy, José A. Font, and Martin Obergaulinger. GRAVITATIONAL WAVE SIGNATURES IN BLACK HOLE FORMING CORE COLLAPSE. *The Astrophysical Journal*, 779(2):L18, dec 2013.

[85] T. Kuroda, T. Takiwaki, and K. Kotake. Gravitational wave signatures from low-mode spiral instabilities in rapidly rotating supernova cores. *Phys. Rev. D*, 89(4):044011, February 2014.

[86] H. Andresen, B. Müller, E. Müller, and H.-T. Janka. Gravitational wave signals from 3D neutrino hydrodynamics simulations of core-collapse supernovae. *Mon. Not. Roy. Astr. Soc.*, 468:2032–2051, June 2017.

[87] K. N. Yakunin, A. Mezzacappa, P. Marronetti, E. J. Lentz, S. W. Bruenn, W. R. Hix, O. E. B. Messer, E. Endeve, J. M. Blondin, and J. A. Harris. The Gravitational Wave Signal of a Core Collapse Supernova Explosion of a 15M$_\odot$ Star. *ArXiv e-prints*, January 2017.

[88] Takami Kuroda, Kei Kotake, Kazuhiro Hayama, and Tomoya Takiwaki. Correlated Signatures of Gravitational-Wave and Neutrino Emission in Three-Dimensional General-Relativistic Core-Collapse Supernova Simulations. *Astrophys. J.*, 851(1):62, 2017.

[89] Jade Powell and Bernhard Müller. Gravitational wave emission from 3d explosion models of core-collapse supernovae with low and normal explosion energies. *arXiv preprint arXiv:1812.05738*, 2018.

[90] John M Scalo. The stellar initial mass function. *Fundamentals of cosmic physics*, 11:1–278, 1986.

[91] Scott M Adams, CS Kochanek, John F Beacom, Mark R Vagins, and KZ Stanek. Observing the next galactic supernova. *The Astrophysical Journal*, 778(2):164, 2013.

[92] E Cappellaro, M Turatto, D Yu Tsvetkov, OS Bartunov, C Pollas, R Evans, and M Hamuy. The rate of supernovae from the combined sample of five searches. *Astron. Astrophys*, 322:431–441, 1997.

[93] FX Timmes and SE Woosley. Gamma-ray line signals from 26al and 60fe in the galaxies of the local group. *The Astrophysical Journal Letters*, 481(2):L81, 1997.

[94] Michael J Pierce, Douglas L Welch, Robert D McClure, Sidney van den Bergh, Renè Racine, and Peter B Stetson. The hubble constant and virgo cluster distance from observations of cepheid variables. *Nature*, 371(6496):385, 1994.

[95] GA Tammann, W Loeffler, and A Schroeder. The galactic supernova rate. *The Astrophysical Journal Supplement Series*, 92:487–493, 1994.

[96] Massimo Capaccioli, Massimo Della Valle, Mauro D'Onofrio, and Leonida Rosino. Properties of the nova population in m31. *The Astronomical Journal*, 97:1622–1633, 1989.

[97] G. A. Tammann, W. Loeffler, and A. Schroeder. The Galactic supernova rate. *Astrophysical Journal, Supplement*, 92:487–493, June 1994.

[98] Wendy L Freedman and Barry F Madore. An empirical test for the metallicity sensitivity of the cepheid period-luminosity relation. *The Astrophysical Journal*, 365:186–194, 1990.

[99] S Mattila and WPS Meikle. Supernovae in the nuclear regions of starburst galaxies. *Monthly Notices of the Royal Astronomical Society*, 324(2):325–342, 2001.

[100] M. T. Botticella, S. J. Smartt, R. C. Kennicutt, E. Cappellaro, M. Sereno, and J. C. Lee. A comparison between star formation rate diagnostics and rate of core collapse supernovae within 11 Mpc. *Astron. and Astrophys.*, 537:A132, Jan 2012.

[101] S Mattila, Tomas Dahlén, Andreas Efstathiou, Erkki Kankare, Jens Melinder, Almudena Alonso-Herrero, MÁ Pérez-Torres, S Ryder, P Väisänen, and Göran Östlin. Core-collapse supernovae missed by optical surveys. *The Astrophysical Journal*, 756(2):111, 2012.

[102] Matthew D Kistler, Hasan Yüksel, Shin'ichiro Ando, John F Beacom, and Yoichiro Suzuki. Core-collapse astrophysics with a five-megaton neutrino detector. *Physical Review D*, 83(12):123008, 2011.

[103] Sidney van den Bergh and Gustav A Tammann. Galactic and extragalactic supernova rates. *Annual Review of Astronomy and Astrophysics*, 29(1):363–407, 1991.

[104] Viktoriya Morozova, David Radice, Adam Burrows, and David Vartanyan. The Gravitational Wave Signal from Core-collapse Supernovae. *The Astrophysical Journal*, 861(1):10, jun 2018.

[105] Lee Samuel Finn and David F Chernoff. Observing binary inspiral in gravitational radiation: One interferometer. *Physical Review D*, 47(6):2198, 1993.

[106] Benjamin P Abbott, R Abbott, TD Abbott, MR Abernathy, F Acernese, K Ackley, C Adams, T Adams, P Addesso, RX Adhikari, et al. All-sky search for short gravitational-wave bursts in the first advanced ligo run. *Physical Review D*, 95(4):042003, 2017.

[107] S Klimenko, G Vedovato, M Drago, F Salemi, V Tiwari, GA Prodi, C Lazzaro, K Ackley, S Tiwari, CF Da Silva, et al. Method for detection and reconstruction of gravitational wave transients with networks of advanced detectors. *Physical Review D*, 93(4):042004, 2016.

[108] Ryan Lynch, Salvatore Vitale, Reed Essick, Erik Katsavounidis, and Florent Robinet. Information-theoretic approach to the gravitational-wave burst detection problem. *Physical Review D*, 95(10):104046, 2017.

[109] Warren G Anderson, Patrick R Brady, Jolien DE Creighton, and Eanna E Flanagan. Excess power statistic for detection of burst sources of gravitational radiation. *Physical Review D*, 63(4):042003, 2001.

[110] Benjamin P Abbott, R Abbott, TD Abbott, MR Abernathy, F Acernese, K Ackley, C Adams, T Adams, P Addesso, RX Adhikari, et al. Observing gravitational-wave transient gw150914 with minimal assumptions. *Physical Review D*, 93(12):122004, 2016.

[111] LIGO Scientific Collaboration. LIGO Algorithm Library - LALSuite. free software (GPL), 2018.

[112] The LIGO Scientific Collaboration. Gravitational Wave Interferometer Noise Calculator.

[113] Adam Burrows, David Radice, and David Vartanyan. Three-dimensional supernova explosion simulations of 9-, 10-, 11-, 12-, and 13-M$\odot$ stars. *Mon. Not. Roy. Astron. Soc.*, 485(3):3153–3168, 2019.

[114] Alessandra Buonanno, Yanbei Chen, and Nergis Mavalvala. Quantum noise in laser-interferometer gravitational-wave detectors with a heterodyne readout scheme. *Physical Review D*, 67(12):122005, 2003.

[115] Benjamin P Abbott, R Abbott, T D Abbott, M R Abernathy, K Ackley, C Adams, P Addesso, R X Adhikari, V B Adya, C Affeldt, and Others. Exploring the sensitivity of next generation gravitational wave detectors. *Classical and Quantum Gravity*, 34(4):44001, 2017.

[116] Alessandra Buonanno and Yanbei Chen. Improving the sensitivity to gravitational-wave sources by modifying the input-output optics of advanced interferometers. *Physical Review D*, 69(10):102004, 2004.

[117] Denis Martynov, Haixing Miao, Huan Yang, Francisco Hernandez Vivanco, Eric Thrane, Rory Smith, Paul Lasky, William E East, Rana Adhikari, Andreas Bauswein, and Others. Exploring the sensitivity of gravitational wave detectors to neutron star physics. *arXiv preprint arXiv:1901.03885*, 2019.

[118] W Keith Hastings. Monte carlo sampling methods using markov chains and their applications. 1970.

[119] James Kennedy and Russell Eberhart. Particle swarm optimization. *Proceedings of ICNN'95 - International Conference on Neural Networks*, pages 1942–1948, 1995.

[120] Sheila Dwyer, Daniel Sigg, Stefan W Ballmer, Lisa Barsotti, Nergis Mavalvala, and Matthew Evans. Gravitational wave detector with cosmological reach. *Physical Review D*, 91(8):082001, 2015.

[121] Haixing Miao, Huan Yang, and Denis Martynov. Towards the design of gravitational-wave detectors for probing neutron-star physics. *Phys. Rev. D*, 98(4):44044, aug 2018.

[122] Karsten Danzmann, LISA Study Team, and Others. LISA: Laser interferometer space antenna for gravitational wave measurements. *Classical and Quantum Gravity*, 13(11A):A247, 1996.

[123] Sukanta Bose, Kabir Chakravarti, Luciano Rezzolla, BS Sathyaprakash, and Kentaro Takami. Neutron-star radius from a population of binary neutron star mergers. *Physical review letters*, 120(3):031102, 2018.

[124] Kentaro Takami, Luciano Rezzolla, and Luca Baiotti. Constraining the equation of state of neutron stars from binary mergers. *Physical Review Letters*, 113(9):091104, 2014.

[125] Harald Dimmelmeier, Christian D. Ott, Andreas Marek, and H.-Thomas Janka. Gravitational wave burst signal from core collapse of rotating stars. *Phys. Rev. D*, 78:064056, Sep 2008.

[126] A Burrows, L Dessart, E Livne, C.˜D. Ott, and J Murphy. Simulations of Magnetically Driven Supernova and Hypernova Explosions in the Context of Rapid Rotation. *Astrophysical J.*, 664:416–434, jul 2007.

[127] A Heger, S E Woosley, and H C Spruit. Presupernova Evolution of Differentially Rotating Massive Stars Including Magnetic Fields. *The Astrophysical Journal*, 626(1):350–363, jun 2005.

[128] A. Marek, H. T. Janka, and E. Müller. Equation-of-state dependent features in shock-oscillation modulated neutrino and gravitational-wave signals from supernovae. *Astron. and Astrophys.*, 496(2):475–494, Mar 2009.

[129] Stefan Hild, Hartmut Grote, Martin Hewitson, Harald Lück, JR Smith, KA Strain, Benno Willke, and Karsten Danzmann. Demonstration and comparison of tuned and detuned signal recycling in a large-scale gravitational wave detector. *Classical and Quantum Gravity*, 24(6):1513, 2007.

[130] Robert Lawrence Ward. *Length sensing and control of a prototype advanced interferometric gravitational wave detector*. PhD thesis, California Institute of Technology, 2010.

[131] Brian J Meers. Recycling in laser-interferometric gravitational-wave detectors. *Physical Review D*, 38(8):2317, 1988.

[132] Vladimir B Braginsky and F Ya Khalili. Quantum nondemolition measurements: the route from toys to tools. *Reviews of Modern Physics*, 68(1):1, 1996.

[133] Benjamin P Abbott, R Abbott, TD Abbott, F Acernese, K Ackley, C Adams, T Adams, P Addesso, RX Adhikari, VB Adya, et al. Gw170817: Implications for the stochastic gravitational-wave background from compact binary coalescences. *Physical review letters*, 120(9):091101, 2018.

[134] H. A. Bethe. Supernova mechanisms. *Rev. Mod. Phys.*, 62:801–866, 1990.

[135] H. Thomas Janka, Tobias Melson, and Alexander Summa. Physics of Core-Collapse Supernovae in Three Dimensions: a Sneak Preview. *Ann. Rev. Nucl. Part. Sci.*, 66:341–375, 2016.

[136] Adam Burrows, David Radice, David Vartanyan, Hiroki Nagakura, M. Aaron Skinner, and Joshua Dolence. The Overarching Framework of Core-Collapse Supernova Explosions as Revealed by 3D Fornax Simulations. *Mon. Not. Roy. Astron. Soc.*, 491(2):2715–2735, 2020.

[137] Ik Siong Heng. Rotating stellar core-collapse waveform decomposition: A principal component analysis approach. *Class. Quant. Grav.*, 26:105005, 2009.

[138] J. Logue, Christian D. Ott, Ik Siong Heng, P. Kalmus, and James H.C. Scargill. Inferring Core-Collapse Supernova Physics with Gravitational Waves. *Phys. Rev. D*, 86:044023, 2012.

[139] Jade Powell, Sarah E. Gossan, Joshua Logue, and Ik Siong Heng. Inferring the core-collapse supernova explosion mechanism with gravitational waves. *Phys. Rev. D*, 94(12):123012, 2016.

[140] Jade Powell, Marek Szczepanczyk, and Ik Siong Heng. Inferring the core-collapse supernova explosion mechanism with three-dimensional gravitational-wave simulations. *Phys. Rev.*, D96(12):123013, 2017.

[141] Vincent Roma, Jade Powell, Ik Siong Heng, and Ray Frey. Astrophysics with core-collapse supernova gravitational wave signals in the next generation of gravitational wave detectors. 2019.

[142] Matthew C. Edwards, Renate Meyer, and Nelson Christensen. Bayesian parameter estimation of core collapse supernovae using gravitational wave simulations. *Inverse Prob.*, 30:114008, 2014.

[143] Christian Rover, Marie-Anne Bizouard, Nelson Christensen, Harald Dimmelmeier, Ik Siong Heng, and Renate Meyer. Bayesian reconstruction of gravitational wave burst signals from simulations of rotating stellar core collapse and bounce. *Phys. Rev.*, D80:102004, 2009.

[144] S. E. Woosley and Alexander Heger. Nucleosynthesis and Remnants in Massive Stars of Solar Metallicity. *Phys. Rept.*, 442:269–283, 2007.

[145] Harald Dimmelmeier, Jerome Novak, Jose A. Font, Jose M. Ibanez, and Ewald Muller. 'Mariage des maillages': A New numerical approach for 3D relativistic core collapse simulations. *Phys. Rev. D*, 71:064023, 2005.

[146] Harald Dimmelmeier, Jose A. Font, and Ewald Muller. Relativistic simulations of rotational core collapse. 2. Collapse dynamics and gravitational radiation. *Astron. Astrophys.*, 393:523–542, 2002.

[147] T. Zwerger and E. Mueller. Dynamics and gravitational wave signature of axisymmetric rotational core collapse. *Astron. Astrophys.*, 320:209–227, 1997.

[148] Soumi De, Christopher M. Biwer, Collin D. Capano, Alexander H. Nitz, and Duncan A. Brown. Posterior samples of the parameters of binary black holes from Advanced LIGO, Virgo's second observing run. 2018.

[149] B.P. Abbott et al. GW170817: Measurements of neutron star radii and equation of state. *Phys. Rev. Lett.*, 121(16):161101, 2018.

[150] L A Wainstein and V D Zubakov. *Extraction of signals from noise*. Prentice-Hall, Englewood Cliffs, NJ, 1962.

[151] Christian D. Ott, E. Abdikamalov, E. O'Connor, C. Reisswig, R. Haas, P. Kalmus, S. Drasco, A. Burrows, and E. Schnetter. Correlated Gravitational Wave and Neutrino Signals from General-Relativistic Rapidly Rotating Iron Core Collapse. *Phys. Rev. D*, 86:024026, 2012.

[152] Jim Fuller, Hannah Klion, Ernazar Abdikamalov, and Christian D. Ott. Supernova Seismology: Gravitational Wave Signatures of Rapidly Rotating Core Collapse. *Mon. Not. Roy. Astron. Soc.*, 450(1):414–427, 2015.

[153] M. Bayes and M. Price. An Essay towards Solving a Problem in the Doctrine of Chances. *Philosophical Transactions (1683-1775)*, 1763.

[154] E. T. Jaynes. *Probability Theory: The Logic of Science.* CUP, 2003.

[155] L. A. Wainstein and V. D. Zubakov. *Extraction of Signals from Noise.* 1970.

[156] C. M. Biwer, Collin D. Capano, Soumi De, Miriam Cabero, Duncan A. Brown, Alexander H. Nitz, and V. Raymond. PyCBC Inference: A Python-based parameter estimation toolkit for compact binary coalescence signals. *Publ. Astron. Soc. Pac.*, 131:024503, 2019.

[157] Daniel Foreman-Mackey, David W. Hogg, Dustin Lang, and Jonathan Goodman. emcee: The MCMC Hammer. *Publ. Astron. Soc. Pac.*, 125:306–312, 2013.

[158] WD Vousden et al. 2016. https://github.com/willvousden/ptemcee.

[159] WD Vousden, Will M Farr, and Ilya Mandel. Dynamic temperature selection for parallel tempering in markov chain monte carlo simulations. *Monthly Notices of the Royal Astronomical Society*, 455(2):1919–1937, 2016.

[160] Joshua S. Speagle. DYNESTY: a dynamic nested sampling package for estimating Bayesian posteriors and evidences. *MNRAS*, 493(3):3132–3158, April 2020.

[161] John Skilling. Nested Sampling. In Rainer Fischer, Roland Preuss, and Udo Von Toussaint, editors, *American Institute of Physics Conference Series*, volume 735 of *American Institute of Physics Conference Series*, pages 395–405, November 2004.

[162] John Skilling. Nested sampling for general Bayesian computation. *Bayesian Analysis*, 1(4):833–859, 2006.

[163] R. Abbasi et al. IceCube Sensitivity for Low-Energy Neutrinos from Nearby Supernovae. *Astron. Astrophys.*, 535:A109, 2011. [Erratum: Astron.Astrophys. 563, C1 (2014)].

[164] M. Ikeda et al. Search for Supernova Neutrino Bursts at Super-Kamiokande. *Astrophys. J.*, 669:519–524, 2007.

[165] R. Acciarri et al. Long-Baseline Neutrino Facility (LBNF) and Deep Underground Neutrino Experiment (DUNE): Conceptual Design Report, Volume 2: The Physics Program for DUNE at LBNF. 12 2015.

[166] Takaaki Yokozawa, Mitsuhiro Asano, Tsubasa Kayano, Yudai Suwa, Nobuyuki Kanda, Yusuke Koshio, and Mark R. Vagins. Probing the Rotation of Core-collapse Supernova With a Concurrent Analysis of Gravitational Waves and Neutrinos. *Astrophys. J.*, 811(2):86, 2015.

[167] Irene Tamborra. Supernova Neutrinos: New Challenges and Future Directions. *J. Phys. Conf. Ser.*, 888(1):012040, 2017.

[168] David Reitze et al. Cosmic Explorer: The U.S. Contribution to Gravitational-Wave Astronomy beyond LIGO. *Bull. Am. Astron. Soc.*, 51:035, 2019.

[169] Sofia Suvorova, Jade Powell, and Andrew Melatos. Reconstructing Gravitational Wave Core-Collapse Supernova Signals with Dynamic Time Warping. *Phys. Rev. D*, 99(12):123012, 2019.

[170] E. Mueller and H.-T. Janka. Gravitational radiation from convective instabilities in Type II supernova explosions. *Astron. Astrophys.*, 317:140–163, January 1997.

[171] K. Kotake, S. Yamada, and K. Sato. Gravitational radiation from axisymmetric rotational core collapse. *Phys. Rev. D*, 68(4):044023, August 2003.

[172] Jeremiah W. Murphy, Christian D. Ott, and Adam Burrows. A Model for Gravitational Wave Emission from Neutrino-Driven Core-Collapse Supernovae. *Astrophys. J.*, 707:1173–1190, 2009.

[173] K. Hayama, T. Kuroda, K. Kotake, and T. Takiwaki. Coherent network analysis of gravitational waves from three-dimensional core-collapse supernova models. *Phys. Rev. D*, 92(12):122001, December 2015.

[174] K. N. Yakunin, A. Mezzacappa, P. Marronetti, S. Yoshida, S. W. Bruenn, W. R. Hix, E. J. Lentz, O. E. Bronson Messer, J. A. Harris, E. Endeve, J. M. Blondin, and E. J. Lingerfelt. Gravitational wave signatures of ab initio two-dimensional core collapse supernova explosion models for 12 -25 M? stars. *Phys. Rev. D*, 92(8):084040, October 2015.

[175] Viktoriya Morozova, David Radice, Adam Burrows, and David Vartanyan. The gravitational wave signal from core-collapse supernovae. *Astrophys. J.*, 861(1):10, 2018.

[176] David Radice, Viktoriya Morozova, Adam Burrows, David Vartanyan, and Hiroki Nagakura. Characterizing the Gravitational Wave Signal from Core-collapse Supernovae. *Ap.J. Letters*, 876(1):L9, May 2019.

[177] A. Burrows, D. Vartanyan, J. C. Dolence, M. A. Skinner, and D. Radice. Crucial Physical Dependencies of the Core-Collapse Supernova Mechanism. *Space Science Reveus*, 214:33, February 2018.

[178] M. A. Skinner, J. C. Dolence, A. Burrows, D. Radice, and D. Vartanyan. FORNAX: A Flexible Code for Multiphysics Astrophysical Simulations. *Ap.J. Suppl.*, 241:7, March 2019.

[179] Adam Burrows and David Vartanyan. Core-Collapse Supernova Explosion Theory. *Nature*, 589(7840):29–39, 2021.

[180] D. Christodoulou. Nonlinear nature of gravitation and gravitational wave experiments. *Phys. Rev. Lett.*, 67:1486–1489, 1991.

[181] Kip S. Thorne. Gravitational-wave bursts with memory: The Christodoulou effect. *Phys. Rev. D*, 45(2):520–524, 1992.

[182] David Vartanyan and Adam Burrows. Gravitational Waves from Neutrino Emission Asymmetries in Core-collapse Supernovae. *Astrophys. J.*, 901(2):108, 2020.

[183] Marie-Anne Bizouard, Patricio Maturana-Russel, Alejandro Torres-Forné, Martin Obergaulinger, Pablo Cerdá-Durán, Nelson Christensen, José A. Font, and Renate Meyer. Inference of protoneutron star properties from gravitational-wave data in core-collapse supernovae. *Phys. Rev. D*, 103(6):063006, 2021.

[184] Jade Powell and Bernhard Müller. Inferring astrophysical parameters of core-collapse supernovae from their gravitational-wave emission. *Phys. Rev. D*, 105(6):063018, 2022.

[185] T. Bruel, M-A. Bizouard, M. Obergaulinger, P. Maturana-Russel, A. Torres-Forné, P. Cerdá-Durán, N. Christensen, J. A. Font, and R. Meyer. Inference of proto-neutron star properties in core-collapse supernovae from a gravitational-wave detector network. 1 2023.

[186] M. Aaron Skinner, Adam Burrows, and Joshua C. Dolence. Should One Use the Ray-by-Ray Approximation in Core-collapse Supernova Simulations? *apj*, 831(1):81, November 2016.

[187] A. Burrows, D. Vartanyan, J. C. Dolence, M. A. Skinner, and D. Radice. Crucial Physical Dependencies of the Core-Collapse Supernova Mechanism. *ssr*, 214(1):33, February 2018.

[188] David Vartanyan, Adam Burrows, David Radice, M. Aaron Skinner, and Joshua Dolence. A successful 3D core-collapse supernova explosion model. *mnras*, 482(1):351–369, January 2019.

[189] Tuguldur Sukhbold, T. Ertl, S. E. Woosley, Justin M. Brown, and H. T. Janka. Core-Collapse Supernovae from 9 to 120 Solar Masses Based on Neutrino-powered Explosions. *Astrophys. J.*, 821(1):38, 2016.

[190] Tuguldur Sukhbold, Stan Woosley, and Alexander Heger. A High-resolution Study of Presupernova Core Structure. *Astrophys. J.*, 860(2):93, 2018.

[191] J. Aasi et al. Advanced LIGO. *Class. Quant. Grav.*, 32:074001, 2015.

[192] F. Banyuls, J. A. Font, J. M. Ibáñez, J. M. Martí, and J. A. Miralles. Numerical {3 + 1} General Relativistic Hydrodynamics: A Local Characteristic Approach. *Ap.J.*, 476:221–231, February 1997.

[193] Andreas Reisenegger and Peter Goldreich. A New Class of g-Modes in Neutron Stars. *apj*, 395:240, August 1992.

[194] Charles W. Misner, K. S. Thorne, and J. A. Wheeler. *Gravitation.* W. H. Freeman, San Francisco, 1973.

[195] Ken-ichi Oohara, Takashi Nakamura, and Masaru Shibata. A way to 3D numerical relativity. *Prog. Theor. Phys. Suppl.*, 128:183–249, 1997.

[196] E. Muller, H. Th. Janka, and A. Wongwathanarat. Parametrized 3D models of neutrino-driven supernova explosions: Neutrino emission asymmetries and gravitational-wave signals. *Astron. Astrophys.*, 537:A63, 2012.

[197] David Vartanyan, Adam Burrows, and David Radice. Temporal and Angular Variations of 3D Core-Collapse Supernova Emissions and their Physical Correlations. *Mon. Not. Roy. Astron. Soc.*, 489(2):2227–2246, 2019.

[198] G Heinzel, A Rudiger, and R Schilling. Spectrum and spectral density estimation by the Discrete Fourier transform (DFT), including a comprehensive list of window functions and some new flat-top windows. page 84, February 2002.

[199] M. W. Trethewey. Window and Overlap Processing Effects on Power Estimates from Spectra. *Mechanical Systems and Signal Processing*, 14(2):267–278, March 2000.

[200] P. Astone, P. Cerdá-Durán, I. Di Palma, M. Drago, F. Muciaccia, C. Palomba, and F. Ricci. New method to observe gravitational waves emitted by core collapse supernovae. *Phys. Rev. D*, 98(12):122002, 2018.

[201] R. Abbasi et al. IceCube Sensitivity for Low-Energy Neutrinos from Nearby Supernovae. *Astron. Astrophys.*, 535:A109, 2011. [Erratum: Astron.Astrophys. 563, C1 (2014)].

[202] Keith C. Gendreau et al. The Neutron star Interior Composition Explorer (NICER): design and development. In Jan-Willem A. den Herder, Tadayuki Takahashi, and Marshall Bautz, editors, *Space Telescopes and Instrumentation 2016: Ultraviolet to Gamma Ray*, volume 9905 of *Society of Photo-Optical Instrumentation Engineers (SPIE) Conference Series*, page 99051H, July 2016.

[203] Thomas Edward Riley. X-PSI: X-ray Pulse Simulation and Inference, February 2021.

[204] M. C. Miller et al. PSR J0030+0451 Mass and Radius from $NICER$ Data and Implications for the Properties of Neutron Star Matter. *Astrophys. J. Lett.*, 887(1):L24, 2019.

[205] Duncan A. Brown, Karan Vahi, Michela Taufer, Von Welch, and Ewa Deelman. Reproducing GW150914: The First Observation of Gravitational Waves From a Binary Black Hole Merger. *Comput. Sci. Eng.*, 23(2):73–82, 2021.

[206] Ria Patel, Brandan Roachell, Silvina Caino-Lores, Ross Ketron, Jacob Leonard, Nigel Tan, Duncan Brown, Ewa Deelman, and Michela Taufer. Reproducibility of the First Image of a Black Hole in the Galaxy M87 from the Event Horizon Telescope (EHT) Collaboration. 5 2022.

[207] R. Ketron, J. Leonard, B. Roachell, R. Patel, R. White, S. Caíno-Lores, N. Tan, P. Miles, K. Vahi, E. Deelman, D. Brown, and M. Taufer. A case study in scientific reproducibility from the event horizon telescope (eht). Research Posters - IEEE 17th International Conference on eScience (eScience21), 2021.

[208] F. Feroz, M. P. Hobson, and M. Bridges. MultiNest: An efficient and robust Bayesian inference tool for cosmology and particle physics. *Monthly Notices of the Royal Astronomical Society*, 398(4):1601–1614, October 2009.

[209] Lisandro Dalcín, Rodrigo Paz, and Mario Storti. Mpi for python. *Journal of Parallel and Distributed Computing*, 65(9):1108–1115, 2005.

[210] Edgar Gabriel, Graham E. Fagg, George Bosilca, Thara Angskun, Jack J. Dongarra, Jeffrey M. Squyres, Vishal Sahay, Prabhanjan Kambadur, Brian Barrett, Andrew Lumsdaine, Ralph H. Castain, David J. Daniel, Richard L. Graham, and Timothy S. Woodall. Open mpi: Goals, concept, and design of a next generation mpi implementation. In Dieter Kranzlmüller, Péter Kacsuk, and Jack Dongarra, editors, *Recent Advances in Parallel Virtual Machine and Message Passing Interface*, pages 97–104, Berlin, Heidelberg, 2004. Springer Berlin Heidelberg.

Chaitanya Afle

⚲ Syracuse, NY | ✉ chafle@syr.edu | ☎ (315) 515-7336 | ⓘ 0000-0003-2900-1333 | ⓞ chaitanyaafle

Education

Aug 2017 - Jun 2023	**Syracuse University, NY, USA** Ph.D. in Physics Advisor: Duncan Brown Thesis Topics: Analysis of gravitational-wave emission from Core-collapse Supernovae, Equation of state constraints of Neutron stars from NICER data (X-Ray) and LIGO-Virgo data (gravitational waves)
Aug 2011 - May 2016	**Indian Institute of Science Education and Research, Pune, India** Bachelor of Science, Master of Science Advisors: Sanjit Mitra (IUCAA, Pune), Anuradha Gupta (IUCAA, Pune) Thesis Topic: Detection and Characterization of Spin-Orbit Resonances in the advanced Gravitational-Wave Detectors Era

Publications

6. Afle, C., Cammerino, J., Kundu, S. K., Vartanyan, D., Brown, D. A., Burrows, A., & Coughlin, E. R. (2023) "Measuring the properties of f-mode oscillations of a proto-neutron star by third generation gravitational-wave detectors". Physical Review D, 107, 123005 https://doi.org/10.1103/PhysRevD.107.123005

5. Afle, C., Miles, P. R., Caino-Lores, S., Capano, C. D., Tews, I., Vahi, K., Brown, D. A., Deelman, E., & Taufer, M. (2023). "Reproducing the results for NICER observation of PSR J0030+0451". arXiv:2304.01035 [astro-ph, cs]

4. Evans, M., Adhikari, R. X., Afle, C., Ballmer, S. W., Biscoveanu, S., Borhanian, S., Brown, D. A., . . . (2021). A Horizon Study for Cosmic Explorer: Science, Observatories, and Community. arXiv:2109.09882 [astro-ph, physics:gr-qc]

3. Afle, C., & Brown, D. A. (2021). Inferring physical properties of stellar collapse by third-generation gravitational-wave detectors. Physical Review D, 103(2), 023005. http://dx.doi.org/10.1103/PhysRevD.103.023005

2. Srivastava, V., Ballmer, S., Brown, D. A., Afle, C., Burrows, A., Radice, D., & Vartanyan, D. (2019). Detection prospects of core-collapse supernovae with supernova-optimized third-generation gravitational-wave detectors. Physical Review D, 100(4), 043026. http://dx.doi.org/10.1103/PhysRevD.100.043026

1. Afle, C., Gupta, A., Gadre, B., Kumar, P., Demos, N., Lovelace, G., Choi, H. G., . . . (2018). Detection and characterization of spin-orbit resonances in the advanced gravitational wave detectors era. Physical Review D, 98(8), 083014. http://dx.doi.org/10.1103/PhysRevD.98.083014

Scientific Talks

Aug 2022	**Reproducing the results for NICER observation of PSR J0030+0451** Network of Neutrinos, Nuclear Astrophysics, and Symmetries (N3AS) Summer School, Santa Cruz, CA
Jul 2022	**Reproducing the results for NICER observation of PSR J0030+0451** Institute of Nuclear Theory (INT) Workshop "Neutron Rich Matter on Heaven and Earth", Seattle, WA (virtual)
Apr 2022	**Measuring the properties of f-mode oscillations of a proto-neutron star by third generation gravitational-wave detectors** American Physical Society (APS) Meeting, New York, NY
Apr 2021	**Inferring physical properties of stellar collapse by third- generation gravitational-wave detectors** American Physical Society (APS) Meeting (online)
Feb 2020	**Inferring physical properties of stellar collapse by third- generation gravitational-wave detectors** Cosmic Explorer Horizon Study Meeting, Boston, MA
Apr 2019	**Detection prospects of gravitational-waves from Core collapse supernovae with third-generation detectors** American Physical Society (APS) Meeting, Denver, CO
Dec 2016	**Detection and characterization of spin-orbit resonances in advanced gravitational wave detectors era** Indo-South American Conference on Numerical Relativity, Pune, India

Posters

Dec 2021	**Inferring physical properties of stellar collapse by third- generation gravitational-wave detectors** Gravitational Waves Physics and Astrophysics Workshop, Hanover, Germany
Dec 2018	**Detection and characterization of spin-orbit resonances in advanced gravitational wave detectors era** Gravitational Waves Physics and Astrophysics Workshop, College Park, MD
Dec 2015	**Detection and characterization of spin-orbit resonances in advanced gravitational wave detectors era** International Conference on Gravitation and Cosmology, Mohali, India

Additional Conferences and Summer Schools

Jun 2021	Astrostatistics Summer School (virtual)
Apr 2020	INT Workshop: The r-process and the nuclear EOS after aLIGO's third observing run (virtual)
Jan 2020	Conference at Schloss-Ringberg, Tegernesee, Germany
May-Jul 2019	KITP Program: The New Era of Gravitational- Wave Physics and Astrophysics, Santa Barbara, CA
Mar 2017	Astrowin International Conference, Hyderabad, India
Feb 2016	Astronomy at Taj, Agra, India
Dec 2013	ICTS Winter School on Experimental Gravitational-wave Physics, Indore, India

Teaching and Mentoring Experience

Feb 2022 - Apr 2023	Mentored Syracuse University undergraduate Jenna Cammerino for research project
Summer 2018	Teaching Assistant, AST 104, Physics Department, Syracuse University
Spring 2018	Teaching Assistant, AST 104, Physics Department, Syracuse University
Fall 2017	Teaching Assistant, PHY 212 "Electricity and Magnetism", Physics Department, Syracuse University
Fall 2015	Teaching Assistant, MTH 100 "Introduction to Proofs", IISER Pune

Computational Skills

- Extensive experience with Python, LaTeX, Bash, Git, C++, C, Mathematica, Fortran, MATLAB, OpenMP, Docker, Singularity, Emacs, Lisp, HTCondor

Extracurricular Activities

- Mentored Summer REU students for Astro-Neutrino program at Syracuse University, Summer 2022

- Reviewed papers for Astronomy and Astrophysics journal.